DISCLAIMER

Final Technical Report (FTR)

Cover Page

a. *Federal Agency*	Department of Energy	
b. *Award Number*	DE-EE0008752	
c. *Project Title*	Roll-to-roll Manufacturing of Continuous Perovskite Modules	
d. *Recipient Organization*	University of Louisville	
e. *Project Period*	*Start:* 6/1/2019	*End:* 6/30/2023
f. *Principal Investigator (PI)*	Thad Druffel Theme Leader Solar Manufacturing R&D thad.druffel@louisville.edu (502) 852-2265	
g. *Business Contact (BC)*	Barbara Sells Associate Director Grants Management barbara.sells@louisville.edu (502) 852-3788	

K.R. "Trey" Bauer III, MPA, CRA / jrs

Digitally signed by K.R. "Trey" Bauer III, MPA, CRA / jrs
Date: 2024.11.01 14:13:07 -04'00'

Signature of Certifying Official

9/4/2024

Date

By signing this report, I certify to the best of my knowledge and belief that the report is true, complete, and accurate. I am aware that any false, fictitious, or fraudulent information, misrepresentations, half-truths, or the omission of any material fact, may subject me to criminal, civil or administrative penalties for fraud, false statements, false claims or otherwise. (U.S. Code Title 18, Section 1001, Section 287 and Title 31, Sections 3729-3730). I further understand and agree that the information contained in this report are material to Federal agency's funding decisions and I have any ongoing responsibility to promptly update the report within the time frames stated in the terms and conditions of the above referenced Award, to ensure that my responses remain accurate and complete.

1. **Acknowledgement:** "This material is based upon work supported by the U.S. Department of Energy's Office of Energy Efficiency and Renewable Energy (EERE) under the Solar Energy Technologies Office Fiscal Year 2018 Award Number(s) DE-EE0008752."

2. **Disclaimer**: “This report was prepared as an account of work sponsored by an agency of the United States Government. Neither the United States Government nor any agency thereof, nor any of their employees, makes any warranty, express or implied, or assumes any legal liability or responsibility for the accuracy, completeness, or usefulness of any information, apparatus, product, or process disclosed, or represents that its use would not infringe privately owned rights. Reference herein to any specific commercial product, process, or service by trade name, trademark, manufacturer, or otherwise does not necessarily constitute or imply its endorsement, recommendation, or favoring by the United States Government or any agency thereof. The views and opinions of authors expressed herein do not necessarily state or reflect those of the United States Government or any agency thereof.”

4. Executive Summary:

Perovskite solar technology has generated excitement since it was first introduced nearly ten years ago by Miyasaka's group with the efficiency increasing rapidly to 25.2%.[1, 2] The efficiency now stands near that of the market leading crystalline silicon solar cell, and the durability has been demonstrated for over 1,000 hours in ambient conditions.[3] The high defect tolerance of the perovskite material makes it suitable for solution-phase deposition, making it a prime option for high volume, roll-to-roll manufacturing. Roll-to-roll manufacturing of thin films is an established platform utilized in numerous industries and is capable of web speeds of 100 m/min. Utilizing small modifications to existing roll-to-roll printing press equipment across the globe, 100+ TW-scale production of perovskite photovoltaics is achievable.[4] Thus the successful implementation of this technology via solution processable roll-to-roll manufacturing can scale to meet anticipated demand.

Radiative processes have been used extensively to dry/anneal thin films and can process these materials at rates unachievable by conventional annealing techniques (convection ovens).[5, 6] A novel and emerging radiative process is intense pulsed light (IPL) annealing. Perovskite solar cells (PSC) annealed via IPL have achieved power conversion efficiency (PCE) of 16% while demonstrating the ability to improve perovskite (PVSK) surface morphology post-deposition via sintering.[7, 8] This technique utilizes high energy, UV/visible wavelength light to directly heat light-absorbing media on a microsecond time scale.

This project researched the development of inks that were roll-to-roll compatible and that could reduce processing time to achieve high speed operation. This necessitated the development of two nanoparticle inks, tin oxide (SnO_2) and nickel oxide (NiO) as electron transport layer (ETL) and hole transport layer (HTL) respectively. Several PVSK inks were also developed including a methyl ammonium lead iodide (MAPI), a mixed cation chemistry (MC) and a triple cation (TC) chemistry. All of these layers were demonstrated in roll-to-roll compatible processes utilizing IPL processing.

The project resulted in devices with efficiencies greater than 18% and operational durability over 500 hours. A technoeconomic analysis of the proposed IPL process incorporated into a roll-to-roll platform demonstrated that the inks and process does have an economic advantage. The work was disseminated through 9 published manuscripts, one patent application and 10 conference presentations. The work will continue at the University of Louisville and is being commercialized by a startup, SoFab Inks.

The project benefits the public through the training of one post-doctorate scholar and four graduate students. The work also has been shown to be economically viable and is being explored and or adopted by commercial entities. The work can lead to a true capability to scale solar energy production, with factories that can be implemented in the United States.

5. Table of Contents:

6. Background:

The PSC has generated a fair amount of interest due to the low cost of materials and manufacturing with a reported highest efficiency of 26.1%, which is on par with traditional technologies of silicon (26.8%) and CdTe (22.3%).[2] The structure of the PSC includes a PVSK thin film that is sandwiched between two charge extraction layers, the ETL and hole transport layer HTL. The technology also lends itself well to tandem devices including PVSK/silicon (33.7%), PVSK/CIGS (24.2%) as well as PVSK multifunction devices (26.4%).[9] All of these devices utilize hole transport or electron transport layers that are carbon based. Most of the work also utilizes coating processes such as spin coating that are not applicable to large area high throughput manufacturing. Nanoparticles can play a very important role in the commercialization of the PSC, since these can be made from earth abundant materials, easy to scale, have suitable band alignment and can impart improved durability. Thus for the roll-to-roll scaling of PSC it is necessary to consider the inks (PVSK and inorganic CTLs) that can be incorporated economically into high throughput production.

6.1 Inks

Inks for the PSC device manufacturing include the ETL, HTL and PVSK thin films. These inks are composed of solvents, surface modifiers and active materials. During deposition surface modifiers improve wetting and post deposition processes are used to evaporate the solvents leaving behind the active materials. A technoeconomic analysis demonstrated how using nanoparticles for the charge transport layers in a PVSK film can achieve a cost of $0.04-$0.10 per watt.[10] Key to this low cost is large area rapid coating on a roll-to-roll system and reduced energy consumption by utilizing IPL annealing. Several recent reviews have examined current efforts in large area PVSK coatings with focus on device architecture and performance.[11-14]

The PVSK ink traditionally has been developed for spin coating techniques and utilizes solvents that form adducts that are removed using anti-solvents. In a large area high speed roll-to-roll platform, these are difficult to establish due to economics and avoiding large crystal transformations in short periods of time. Thus, the inks for these must take into consideration fast evaporations that yield stable films not needing excessive processing time (space). These formulations must also be stable in large volumes such that operators can load inks for 24/7 production.

The specific nanoparticle materials for the HTL and ETL are typically metal oxides that can be very straightforward to synthesize and disperse in solvents suitable for volume manufacturing. The functionalization schemes of these metal oxides have been studied at length to improve dispersion in selected solvents and to establish homogeneous inorganic/organic thin films. This solvent engineering scheme has resulted in the capability to deposit a SnO_2 ink directly onto a PVSK thin film yielding an efficiency of 16.5% using a flexible polymer substrate.[15] Our unpublished work has achieved efficiency greater than 20%.

6.1.1 Perovskite

A typical roll-to-roll process has three steps: (1) mixing of precursors, (2) coating of ink, and (3) drying/annealing of the coating. For PVSKs, the result is a layered thin film

structure that has desired photovoltaic properties when patterned correctly. The coating window is a multidimensional space of operating parameters that constitutes a permissible region of operability to yield uniform coatings. The success for roll-to-roll manufactured PSCs lies in the art of understanding how the coating window changes within a wide range of operating parameters including ink formulation, additives, deposition methods, and annealing techniques.[16, 17]

Consistent PVSK thin-film deposition can be achieved when the PVSK thin-film coating fundamentals are understood in detail. Generally, the LaMer model of nucleation and growth is used to describe PVSK film formation, which is solubility driven.[18] Common PVSK precursors form adducts in solution according to the Lewis theory for acid-base reactions causing solubility to correlate strongly with Gutmann's donor number.[19] Utilizing a combination of Gutmann's donor number and vapor pressure, evaporation kinetics and growth mechanisms can be controlled. Deng et al. proposed segmenting solvents into volatile, non-coordinating solvents (VNCS) and non-volatile, coordinating solvents (NVCS) to allow users to mix solvents in formulations that amplify their respective merits (quick evaporation, high crystallinity/large grain size). In general, consistent PVSK film formation happens when the three stages of solvent evaporation, transitional phase formation, and annealing occur as independently as possible. The modular nature of PVSK deposition allows for application of multiple different techniques to enhance the film post-deposition; however, changes to solvent chemistry and/or compositional engineering must have synergy from deposition to annealing all while remaining cost competitive.

The first iteration of a functioning PSC utilized a MAPI formulation and has remained the most widely studied formulation. Regardless of the particular formulation, the stability of PVSK materials is susceptible to alterations caused by environmental conditions such as temperature, moisture, and pressure.[20] The optoelectronic properties of PVSK films are dependent upon morphology, crystallinity, and stoichiometry, to name a few, that can be altered by pre-and post-treatments, doping, ambient conditions, deposition methods, solvents, molar compositions, drying conditions, and annealing parameters.[21-24] Despite the remarkable progress, the most significant barriers to PSC PV commercialization are stability, scalability, and manufacturing.[25]

A-site substitutions include (MA^+), formamidinium (FA^+), cesium (Cs^+), ethylammonium (EA^+), and butylammonium (BA^+) ions. Replacing MA^+ with FA^+ lowers the band gap of the absorber layer, but generally have better electronic properties, higher symmetry and PCE.[26] Mixing A-site cations have been shown to improve the PVSK crystallinity and phase stability, improve reproducibility, achieve stabilized power output efficiencies, unachievable by the individual compositions alone.[27, 28] For example, both pure MA- and FA-based PVSKs are sensitive to ambient conditions, however, the higher dipole moment of MA^+ stabilizes photoactive α-$FAPbI_3$ PVSKs when combined.[29] Unfortunately, the low volatility of MA cation leads to low thermal and photostability.[30]

Transitioning from double cation systems to triple and quadruple systems, allows for another parameter to manipulate the PVSK properties. Introducing Cs to double cation systems reduces the tolerance factor towards the stable cubic α-phase and showed higher thermal stability and reproducibility.[27] Islam et al. reported that, according to their computational study, the addition of Cs to $FAPbI_3$ induces strain, due to the size

mismatch, that suppresses re-orientation of FA^+.[31] These results were confirmed by Stranks et al. who showed that $FAPbI_3$ maintained the photoactive α-phase by octahedral tilting of 2°.[32] Compositional engineering strategies to suppress the transition to the hexagonal phase upon cooling to room temperature require an understanding of the re-orientational dynamics of FA^+[33], how they influence octahedral tilting in the halide PVSK, and how the re-orientational modes can be controlled through alloying in the A-site.[28]

A number of strategies have been developed to mitigate A-site cation migration including surface passivation[34], mixed phases[35], and doping with alkali cations.[36, 37] Schelhas et al. determined that an important parameter to determine phase stability is the Gibbs free energy of mixing (ΔG_{mix}).[38] Cs-FA PVSKs with less negative ΔG_{mix} demonstrated poorer operational stability due to de-mixing into photoinactive Cs-rich clusters, thus reducing cation migration.[39] Methods to reduce the A-site migration are important for mixed cation PVSKs should improve operational stability and reduce hysteresis. Saidaminov suggests that A-site composition have a significant impact on carrier diffusivity across grain boundaries, where MA-based PVSKs have an order of magnitude larger diffusivity than Cs-FA PVSKs without MA.[40, 41]

It is well established that mixing A-site cations improves stability as well as reproducibility of PSCs; however, the relationship of chemical composition/crystal structure/performance/phase stability is yet to be established. Many post-deposition characterization techniques have yielded a lot of information about re-orientation dynamics of alkylammonium cations and structural transitions of MA- and FA-based PVSKs, but the lack of detailed information about the role of different cations in the crystallization mechanism need to be urgently addressed.[28]

Additives play a critical role in the field of PVSK precursor chemistry. Their functions extend to various aspects of PVSK film formation and performance, including modulation of film morphology, stabilization of the essential components, namely FA and Cs, both in the precursor solution and in the final PVSK film, alignment of energy levels within the PSC, reduction of non-radiative recombination pathways, mitigation of hysteresis, and overall improvement of operational stability.[42] These additives serve to optimize the crystalline structure of the PVSK film, ensure uniform coverage, enhance efficiency and stability, maximize the conversion of absorbed light into electrical energy, and prolong the lifespan of PSCs. The specific objectives of adding additives may vary, depending on the application, and often involve a combination of these factors.

Despite the abundance of additive materials, a limited number have been evaluated for compatibility with IPL annealing. Diiodomethane (CH_2I_2) has been shown to reduce pinholes, increase grain size, and improve overall device efficiency for both $MAPbI_3$ and triple cation PSCs using IPL annealing.[8, 43] Xu et al. elucidated that the addition of CH_2I_2 promotes grain growth in the vertical direction, increases the I/Pb ratio in the final film, and removes the I- ionic diffusion/defect signature associated with iodine interstitials.[44] The outcomes of these studies have led to the development of PSCs exhibiting PCEs greater than 17%, as well as significantly reduced annealing times to a millisecond scale. Table 6.1 details different PVSK materials and scalable techniques to deposit these that have been employed in the literature.

Table 6.1 Survey of PSC devices manufactured using roll-to-roll compatible processes.

Deposition Method	Structure	Substrate	PCE (%)	Area (cm^2)	Date	Ref.
Inkjet Printing	MAFACsRb PVSK	Glass	16.09	802	2020	[45]
Spray Coating	CsFA PVSK	Glass	13.82	112	2021	[46]
Slot-Die Coating	FA0.83Cs0.17PbI3	Glass	19.54	65	2021	[47]
Doctor Blading	ITO/PTAA/MAPbI3/C60/BCP/Cu	Glass	14.6	57.2	2018	[48]
Blade Coating	MA0.6FA0.4PbI3	Glass	19.7	50.1	2021	[49]
Blade Coating	FTO/c-TiO2/m-TiO2/FA1-x-yMAxCsy(I1-xBrx)3/spiro-OMeTAD/Au	Glass	11.59	50	2020	[50]
Spray Coating	FTO/TiO2/MAPbI3xClx/PTAA/Au	Glass	15.5	40	2016	[51]
Slot-Die Coating	FTO/NiOx/(FAPbI3)0.95(MAPbI3)0.05/G-PCBM/BCP/Ag	Glass	14.17	36	2019	[52]
Doctor Blading	ITO/PTAA/MAPbI3/C60/BCP/Cu	Glass	15.3	33	2018	[48]
Doctor Blading	FTO/TiO2/MAPbI3xClx/spiro-OMeTAD/Au	Glass	13.3	11.09	2017	[53]

6.1.2 Tin Oxide

The primary role of an ETL in PSCs is to enable efficient extraction of photogenerated electrons from the PVSK absorber layer and transport them to the electrode, while concurrently inhibiting hole transport, thus reducing charge recombination probability. Moreover, the ETL acts as a protective barrier between the PVSK and the electrode, mitigating the degradation of the PVSK layer due to contact with the metal electrode. Various binary and ternary metal oxides, including TiO_2, ZnO, SnO_2, WO_3, In_2O_3, Nb_2O_5, Fe_2O_3, Cr_2O_3, CeO, $BaSnO_3$, $SrSnO_3$, $BaTiO_3$, $SrTiO_3$, Zn_2SO_4, Nb_2O_5, and $BaSnO_3$, have been explored as ETLs in n−i−p configurations.[54-56] Of these TiO_2, ZnO and SnO_2 have been demonstrated as effective inorganic ETLs. SnO_2 has demonstrated it to be effective in both n-i-p and p-i-n configurations with little to no annealing necessary when deposited from solution phase.

For an ETL material to be effective it needs to have a conduction band that is slightly lower than that of the PVSK, while also having a deep valence band to prevent electron-hole recombination. This wide band gap is also important for insuring high transparency and maximum light adsorption by the PVSK layer. Additionally, the selected material needs to have high electron mobility to reduce internal series resistance and increase charge extraction. A uniform and pinhole-free ETL is essential to prevent charge recombination and device degradation. As PVSK research moves to improving stability

and scalability the extra considerations of environmentally stable and process compatibility are now also being considered.

Developed initially in dye-sensitized solar cells, titanium dioxide (TiO_2) was the first ETL material used in a PVSK sensitized solar cell during the pioneering work of Miyasaka's team in 2009.[1] Transitioning from the complex mesoporous scaffold to a simpler planer structure was demonstrated as feasible by Snaith et al. in 2013.[57] Snaith et al. followed this initial result with a vapor phase deposited PVSK on compact TiO_2 resulting in a PCE of over 15% accompanied by an open circuit voltage of 1.07 V.[58] Following this innovation, researchers began to investigate other low-temperature processable ETLs such as ZnO, PCBM, and SnO_2 as potential alternatives to TiO_2 for use in simple planar structures. Currently, tin(IV) oxide (SnO_2) has emerged as a prominent ETL alternative to TiO_2 and zinc oxide (ZnO) in PSCs, with the highest reported PCE of 25.7% in single-junction planar structures.[59] SnO_2 is a wide bandgap n-type semiconductor (3.5-4.0eV) that aligns with the conduction band of the PVSKs and is transparent to most visible and UV light. It also has been reported to have high electron mobility (200 to 250 $cm^2/V•S$) while being able to be processed at low temperatures.[60]

The processing temperature requirements for SnO_2 are also lower than those for TiO_2, broadening the range of viable substrates for PSCs fabrication, to include flexible and temperature-sensitive polyethylene terephthalate (PET) based substrates. SnO_2 as an ETL is amenable to a wide variety of deposition methods, such as spin-coating, spray coating, blade coating, and slot die coating. This adaptability introduces greater flexibility into the fabrication process, but most work with SnO_2 uses the n-i-p configuration as the deposition of SnO_2 on top of a PVSK is challenging. Finally, SnO_2 is non-toxic and environmentally friendly, characteristics that enhance its suitability as an ETL material for large-scale production and application of PSCs.

The low-temperature fabrication methodologies of SnO_2 have provided its suitability for the development of flexible PSCs on low temperature substrates.[61, 62] Standard flexible plastic substrates like PET (Tg: 70–110 °C) and polyethylene naphthalate (PEN) (Tg: 120–155 °C) are capable of withstanding limited heating, but are incompatible with higher temperature precursor or mesoporous annealing conditions. Low temperature work by Song et al. and Qi Jiang et al. have demonstrated up to 21.6% PCE using commercially available SnO_2 nanoparticles. [63-65] As flexible modules and roll to roll processing become more common, colloidal SnO_2 nanoparticles have been deemed a promising route to formulate the ETL for flexible PSCs. The utilization of nanoparticles circumvents the high-temperature sintering process, which would otherwise be integral in the transition from precursors to SnO_2 films. Additionally, pre-synthesized nanoparticles can be suspended in an array of solvents that are compatible with PVSK enabling direct coating on the PVSK layer to serve as an upper charge transport layer (CTL). Consequently, the utilization of pre-synthesized SnO_2 nanoparticles simplifies the process and holds the potential to shorten the total fabrication time.

The synthesis of SnO_2 nanoparticles is generally achieved through precipitation, solvothermal, hot injection, and the inverse micelle-water injection methods.[61, 62, 66, 67] These processes result in the formation of pre-synthesized SnO_2 nanoparticles, which are subsequently deposited onto a substrate to form a film. A distinct advantage of synthesized nanoparticles is the ability to engineer surface ligands and solubility to fit a

desired application (Table 6.2). An example of this is the work of Xie et al. where they developed highly crystalline SnO_2 nanoparticles with superior dispersibility in non-polar solvents utilizing a solvothermal method. Using spin-coating they were able to deposit a high quality SnO_2 film on ITO-PEN that had a PCE of 13.90%[62] Park et al. engineered ultrafine SnO_2 quantum dots (QD) capped with a liable ligand where the ligands spontaneously exchanged with halides in a PVSK solution as part of the coating process, leading to an appropriate SnO_2 QD–halide junction resulting in a PCE of 17.7% with a short circuit current density (J_{sc}) of 19.7 mA cm^{-2}, open circuit voltage (V_{oc}) of 1.13 V, and a fill factor (FF) of 79.0%. [61]

Along with ligands and solubility, the electrical properties of nanoparticles can be tuned by the introduction of dopants to the crystal lattice. Doping of semiconducting metal oxides (MO_x) effectively modulates electrical properties such as carrier concentration and electron mobility, in addition to altering optical and structural properties. Common doping methodologies can be categorized as equivalent cation doping in which the material is doped with an ion of the same oxidation state, and nonequivalent cation doping in which the material is doped with an ion of higher or lower oxidation state. Equivalent cation doping improves defect densities, improves carrier mobility, and induce alterations in the energy band structure, which can lead to diminished trap-state density and promoted energy band alignment with PVSK. Noh et al. demonstrated Zr doping in SnO_2 that resulted in a conduction band up shift which increased the built in potential and improved the band alignment with the PVSK with a champion device achieving a PCE of 19.54%.[68]

Nonequivalent doping directly effects the electron density of the conduction band. Specifically, the incorporation of lower valence cations such as Li^+,[69] Mg^{2+}, Zn^{2+},[70] Y^{3+}, and Al^{3+} into the crystal lattice of tetravalent Sn^{4+} or Ti^{4+} results in p-type doping, while the incorporation of higher valence cations like Nb^{5+}, [71] and W^{6+} yields n-type doping. The incorporation of higher valence cations, n-type doping, enhances the electron density causing a more positive shift in the conduction band. Together the shifted conduction band and increased electron density increase film conductivity.[72-74] Ren and associates report a 2.44% increase in PCE using Nb-doped SnO_2. [71] P-type doping decreases the electron density of the conduction band while upshifting the Fermi level and decreasing the oxygen vacancies. This promotes electron transport while impeding charge recombination at the ETL/PVSK interface. [70] Yang et al. reported the Y doping led to a more positive conduction band minimum in Y-SnO_2 improving conductivity and charge extraction. [75]

As mentioned before, one of the benefits of nanoparticles is their adaptability to a variety of solution deposition methods. Solution deposition methods are widely employed due to their cost-effectiveness, ease of implementation, and versatility. Various deposition methods, including spin-coating, chemical bath deposition (CBD), spray pyrolysis, screen printing, blade-coating, and slot-die coating, can achieve solution-processed deposition.[76-78] Currently spin-coating is the most common method utilized in lab scale research but interest is increasing in larger area depositions. A recent study by Siegrist et al. on the effect of blade coating parameters including blade speed, blade gap, ink concentration and volume, and stage heating. They conclude that

of blade coating of large area devices is best performed using a continuous solution supply with blade coating and further development of slot die coating.[79]

Table 6.2: Survey of recent works using SnO_2 as the ETL. SC: Spin-coating,

Regular (P-I-N) architecture								
Device architecture	**ETL**	**Deposition**	**Processing**	**J_{sc}**	**V_{oc}**	**FF**	**PCE**	**Ref**
Sb:SnO_2/ $MAPbI_3$/ spiro-OMeTAD/ Au	NC	SC	100°C, 30 min	22.6	1.06	72.0	17.2	[74]
PEN/ ITO/ $MAPbI_3$/ spiro-OMeTAD/ Au	NC	SC	80°C, 15min	19.7	1.13 V	79.0%	17.7%	[61]
ITO/ SnO_2/ $(FAPbI_3)_x(MAPbBr_3)_{1-x}$/ Spiro-OMeTAD/ Au	NC	SC	150°C, 30 min	24.87	1.09V	74.77%	20.27%	[64]
ITO/ SnO_2/ $(FAPbI_3)_x(MAPbBr_3)_{1-x}$/ Spiro-OMeTAD/ Au	NC	SC	150°C, 30 min	25.2	1.18	78.4%	23.32%	[80]
ITO/ SnO_2/ $MAPbI_3$/ Spiro-OMeTAD/ MoOx/Ag	NC	Slot-die	Air-knife, IPL	23.70	0.91	52.0	11.24	[81]
ITO/ SnO_2/ $MAPbI_3$/ Spiro-OMeTAD/ Au	NC	Blade	100°C	22.86	1.124	76.17%	19.6	[17]
ITO/SnO_2/ $Cs_{0.05}FA_{0.85}MA_{0.15}PbI_{2.9}Br_{0.15}$/ Spiro-OMeTAD/Au	NC	Spray	150°C, 30 min	23.35	1.14	66.6	17.78	[82]
Inverted(N-I-P) architecture								
glass/ ITO/ NiO_x/ $MAPbI_3$/ ZnO/ Al	NC	SC	N/A	21.0	1.01	76	16.1	[83]
Glass- ITO/ PTAA/ PFN/ $MAPbI_3$/ SnO_2-A/Ag.	NC	Blade	100°C, 10 min	22.6	1.02	61.0	14.1	[84]
PET/ ITO/ PTAA/ PFN/ $MAPbI_3$/ Y:SnO_2-A/ BCP/ Ag	NC	Blade	100°C for 2 min	22.38	1.08	68.4%	16.5%	[15]
PET/ ITO/ PTAA/ PFN/ FAMAPbIBr/ Y:SnO_2-A/ BCP/ Ag	NC	Blade	IPL	23.7	1.09	65.7	16.9	[85]

6.1.3 Nickel Oxide

HTL materials face many of the same considerations as ETLs for material characteristics but with the electronics targeting hole transport instead of electron transport. Favored for their stability over organic alternatives and good band alignment with the valence band of the PVSKs; NiO_x, Cu_xO, CuI, CuSCN, and CuS, have been explored as HTLs through a variety of methods. Inorganic copper salts such as CuSCN, CuI, and CuS have shown promise as inorganic options for devices of n-i-p configuration.[86] Copper oxide nanoparticles are also an active field of work with delafossite like composition ($CuM^{3+}O_2$) recently emerging as a promising solution to the instability of Cu_2O.[87] To date, copper oxide nanoparticles trail nickel oxide (NiO_x) in terms of conductivity and device performance, which has been the most successful

inorganic HTL to date. Due to its natural self-doping p-type character NiO_x has shown high hole carrier densities, conductivity, and good band alignment with PVSKs. These properties make it a natural choice for use as an HTL.

Precursor deposition is a popular method for NiO_x film formation as it by passes the often-tedious cleaning process and directly forms the NiO_x film on the desired substrate. This has the advantage of being able to form highly uniform films with few defects.[88-92] However, this method has a high thermal cost (300-600 °C) and long annealing time (1-3 hours) that make it incompatible with flexible substrates. Work with photonic curing by Piper et al. has presented some promising results by reducing the annealing time to several seconds instead of hours.[92] A recent example of work done using precursor inks, is the work of Li et al. with utilizing urea to passivate surface defects on the NiO_x surface. Their resulting devices achieved a champion PCE of 23.61%.

While precursor-based inks have demonstrated remarkable efficiency, so to have nanoparticle-based inks without the high thermal cost. Our work has focused on moving to scalable deposition methods on flexible PET substrates so accounting for this high thermal cost has directed our current work to lower temperature options. An advantage of working with nanoparticles is the versatility they offer as composite coatings with other HTL materials or by functionalization of the particle surface. An active area of current research is in the passivation of defects at the NiO_x/PVSK interface. Whether by doping or introducing a passivator into the NiO_x ink prior to coating, nanoparticles can be customized to address the specific needs of the application.

The most common method for synthesizing NiO_x nanoparticles is the low temperature precipitation method.[93-100] In general a nickel salt is dissolved in water then precipitated by the addition of base to form $Ni(OH)_2$. Controlling the particle surface through selection of the counter anions or introduction of ligands to the reaction mixture is critical for forming small, stable particles. In 2021, Guo et al. demonstrated an average 2% PCE increase when using nitrate vs chloride.[97] Their further analysis shows a direct relationship between ink stability and the identity of the initial counter anion. Addition of ligands prior to precipitation has also been shown to effectively control particle growth.[101] Cui et al. has taken this one step further by using alkylammonium hydroxides as the base to introduce alkylammonium ligands during precipitation.[95] Their champion devices reached a PCE of 22%, with a duel NiO_x/PTAA HTL layer.

An additional property that is important to control in the particles during synthesis is the Ni^{2+}/Ni^{3+} ratio, which produces the innate p-type character of NiO_x.[102-105] Doping with transition metals such as Co,[106] V,[107] and Cu,[96, 104] have been found to induce changes the Ni^{2+}/Ni^{3+} ratio while also improving conductivity.[105] A seminal investigation by Chen et al. in 2018 revealed important insights into the mechanism of Cu doping.[104] Utilizing DFT to calculate the density of states, they found a shift in gap state positions of NiO_x from 1.3 -2.0 eV to 0.7eV in Cu:NiO_x. This shift resulted in shallower acceptor levels which would likely lead to improvements in conductivity and the work function. Investigations by XPS showed no significant change in the Ni^{2+}/Ni^{3+} peak ratio, which was observed in prior studies, but did confirm the presence of both Cu^{2+} and Cu^{+} indicating that the change in conductivity is likely related to the copper oxidation state.[108]

Table 6.3: Survey of recent works using NiO_x as the HTL. SC: Spin-coating

Regular (P-I-N) architecture								
Device architecture	**HTL**	**Deposition**	**Processing**	**J_{sc}**	**V_{oc}**	**FF**	**PCE**	**Ref**
Glass/ ITO/ NiO_x-Urea/ $CsFAMAPbI_3$/ BzMIMBr/ C60/ BCP/ Ag	Precursor	Spray Pyrolysis	400C, 20 min	24.04	1.15	85.4	23.61	[91]
glass/ ITO/ NiO_x/ TC/ $PC_{61}BM$/ ZnO NPs/ Ag	Precipitation, Precursor	SC	350C, 30 min or 300C, 45 min	24.34	1.06	79.18	20.45	[109]
Glass/ NiO_x/ CsFAMAPbIBr/ PCBM:C60/ BCP/ Au	Precipitation	SC	100C, 10 min	23.49	1.15	84.68	22.81	[110]
Glass/ ITO/ NiO_x/ PTAA/ CsFAMAPbIBr/ PCBM/ Ag	Precipitation	SC	150C, 20 min	24.52	1.13	82	22.71	[95]
Glass/ ITO/ NiO_x/ CsFAMAPbIBr/ C60/ BCP/ Cu	Precursor	SC	180C, 10 min+ 400C, 45 min or UV lamp 10min	24.25	1.126	82.19	22.45	[111]
Glass/ ITO/ NiO_x/ CBSA/ CsFAMAPbIBr/ PCBM/ BCP/ Ag	Precipitation	SC	130C, 20 min	23.72	1.11	81.43	21.8	[112]
Glass/ ITO/ NiO_x/ TMPA/ MAPbI/ PCBM/ BCP/ Ag	Precipitated	SC	No Anneal	23.7	1.07	80.4	20.4	[113]
PEN/ hc-PEDOT:PSS/ NiO_x/ $Cs_{0.05}FA_{0.85}MA_{0.10}Pb(I_{0.97}Br_{0.03})_3$/ PCBM/ Ag	Precipitation	Blade Coated	130 C, 30 min	23.74	1.12	74.7	19.87	[114]
Glass/ ITO/ Li:NiO_x/ NiO_x/ FAMAPbIBr/ PCBM/ BCP/ Ag	Precursor	SC	120 C, 10 min + 2nd coat 450 C, 1h	23.22	0.99	82.83	19.04	[89]
Glass/ ITO/ V:NiO_x/ $MAPbI_3$/ PCBM/ BCP/ Ag	Solvothermal	SC	25C, 15 min + UV-V 20 min	19.81	1.04	75	15.45	[107]
Glass or PET/ ITO/ NiO_x/ $MAPbI_{3-x}Cl_x$ / PCBM-C60/ Zracac/ Ag	Precipitation	SC	No Anneal	23.16/ 22.02	1.11/ 1.06	81/ 78	20.83/ 18.16	[96]
Glass/ ITO/ NiO_x/ $Cs_{0.05}MA_{0.16}FA_{0.79}Pb_{1.03}(Br_{0.16}I_{0.86})_3$/ LiF/ C60/ BCP/ Ag	Precursor, Sputtered, Precipitation	SC	Precursor: 400C, 50 min; Nanoparticles: No Anneal	19.56	1.15	84.7	19.06	[115]
Inverted(N-I-P) architecture								
Glass/ ITO/ TiO_2/ MAPbI/ NiO_x/ Au	Precipitation	SC	100C, 5 min	23.59	0.885	60.1	12.57	[98]

6.2 IPL Process

Roll-to-roll manufacturing is a robust technique with great potential to process high-throughput PSC, addressing many problems of scale.[116] However, the production capacity of a roll-to-roll line is limited by the slowest step. Encouraging results have been demonstrated for high-throughput processing of NiO[92], SnO_2[84], Cu[117], and PVSK[43, 81] layers by intense pulsed light (IPL) annealing, with opportunities for further refinement.

Consistent PVSK thin-film deposition can be achieved when the PVSK thin-film coating fundamentals are understood in detail. Generally, the LaMer model of nucleation and growth is used to describe PVSK film formation, which is solubility driven.[18] Common pPVSK precursors form adducts in solution according to the Lewis theory for acid-base reactions causing solubility to correlate strongly with Gutmann's donor number.[19] Utilizing a combination of Gutmann's donor number and vapor pressure, evaporation kinetics and growth mechanisms can be controlled. Deng et al. proposed segmenting solvents into volatile, non-coordinating solvents (VNCS) and non-volatile, coordinating solvents (NVCS) to allow users to mix solvents in formulations that amplify their respective merits (quick evaporation, high crystallinity/large grain size). In general, consistent PVSK film formation happens when the three stages of solvent evaporation, transitional phase formation, and annealing occur as independently as possible. The modular nature of PVSK deposition allows for application of multiple different techniques to enhance the film post-deposition; however, changes to solvent chemistry and/or compositional engineering must have synergy from deposition to annealing all while remaining cost competitive.

The potential for low-cost manufacturing with adaptability to massive scalability and the use of turnkey deposition tools are the main attractions for roll-to-roll manufacturing. Typically, this involves continuously printing functional layers onto a flexible substrate with transparent conducting oxide (TCO) coated plastics being the most promising substrate. Utilizing conventional methods, the combination of thermal and mechanical stressors in PSC manufacturing can severely compromise functionality within the substrate during operation. Several roll-to-roll compatible annealing techniques, including hot air blowing[118], flash infrared[119], rapid thermal[120], and microwave annealing[121], have been investigated for fabrication of PSCs with promising results. However, electromagnetic absorption by flexible plastic substrates, from these radiative sources, can result in the same substrate instabilities observed in conventional annealing methods. Intense pulsed light (IPL) annealing has drawn widespread attention for its ability to rapidly anneal light absorbing materials (~1ms) without affecting transparent substrates.[8, 43] Successful integration of IPL annealing in high-throughput roll-to-roll manufacturing lines can reduce oven energy requirements by 80% and reduce the annealing footprint by two orders of magnitude over conventional methods.[10] While optimized IPL annealing promotes thin-film densification and grain growth, PSCs manufactured with this method lag behind the state-of-the-art PCEs by ~7-8%. Understanding the interactions between IPL annealing and properties of the PVSK film will help devices approach the state-of-the-art at much higher manufacturing throughputs.

Thin-film synthesis typically involves a thermal annealing step to convert from precursors to final material phases, to obtain the desired crystalline phase, or to improve materials structural/electrical properties. Conductive thermal annealing, the primary annealing method in PSC fabrication, is not suitable for roll-to-roll due to lengthy annealing times and/or large production line requirements.[13] Convective ovens are the natural substitute, however, they too face the same challenges. As an illustration, if a roll-to-roll line with a web speed of 30 m/min had a dwell time of 10 minutes, then it would need a 300 m oven.

The consequences of such extended web length in a roll-to-roll line are not only limited to increased footprint and cost but can also negatively impact yield through elevated web tension demands and misalignment issues. A drawback of using a convective oven for plastic substrates is the need to maintain the operating temperature below the temperature at which the plastic would undergo deformation under tensile stress. The combination of these stressors can severely negatively impact conductivity of the TCO layer on top of the plastic where an increase in surface resistivity of 40 ohm per square can decrease efficiency by 70%.[122, 123] It is evident that advances are necessary in the realm of scalable annealing techniques for PSCs..

Radiative thermal processes have been utilized extensively in roll-to-roll manufacturing for drying, annealing, and sintering applications. Belt infrared (IR) furnaces have been used for several decades in the manufacture of silicon solar cells, where thick films are dried, polymer binders are decomposed and metal materials are sintered.[124] IR heating elements, capable of rapidly reaching temperatures exceeding 800 degrees Celsius and featuring high processing speeds of several meters per minute, have been adapted for implementation in roll-to-roll production processes. These elements have been successfully utilized to demonstrate the feasibility of high-throughput sintering of metal on polymer substrates.[125] Similarly, the use of microwaves has also been adapted to sintering metals on polymer substrates.[126] The use of radiative techniques, such as IR heating and microwave heating, has been shown to reduce dwell times in comparison to traditional convection ovens.

The IPL process involves the absorption of light energy from a broad-spectrum, rapid pulse emitted by a xenon bulb onto a thin film. The use of a thin film with high absorptivity within the IPL spectrum allows for the absorption of radiative energy and its rapid conversion into thermal energy. This process results in the uniform irradiation of a relatively large surface area, making it suitable for the heating of large-area PSCs. IPL lamps can be tuned to utilize energies spanning the UV, visible, and into the IR regions. The technology has been utilized in processing polymers, metals, metal oxides and semiconductors since the 1970's but recently has found industrial applications for materials in PVs.[127, 128] Two advantages of IPL are short processing times and compatibility with low heat-tolerant, transparent substrates.

The first reported application of IPL processing on PVSK materials was conducted on a sequentially deposited PbI_2 and methylammonium iodide film, resulting in a significant phase transition from cubic particles to a dense PVSK film.[7] It was observed that IPL provided better penetration of the mesoporous TiO_2. Although the higher energy densities led to improved crystallization, excessive energy or prolonged pulses lead to thermal degradation to the PVSK films.[129, 130] The duration of the pulse has also been shown to influence the crystallization of PVSK materials, with longer pulses resulting in larger grain sizes, surpassing those obtained through hot plate annealing.[129]

The IPL process has been established for films of interest to the PSC with several research groups demonstrating the process in manufactured devices with efficiencies of over 16%.[8] for a single PSC device.[43] (Table 6.4)

Table 6.4: Examples of IPL processing of thin films used in PSCs from literature.

Layer	Energy Density (J/cm^2)	Pulse Duration (μs)	Number of Pulses	Substrate	PCE (%)	Ref
TiO_2	12.3	2000	10	Glass	16.7	[131]
				PEN	12.3	
TiO_2	17.3	2000	5	PET	8.1	[132]
SnO_2	11.7	2000	5	Glass	12.0	[43]
SnO_2	4.6	2000	10	Glass	15.3	[133]
$MAPbI_3$	25	2000	5	Glass	16.5	[8]
$MAPbI_3$		1150	1	Glass	11.3	[130]
$MAPbI_3$	0.89-1.78	1125-1982	6	Glass	11.75	[134]
$MAPbI_3$	33	2000	1	Glass	12.3	[7]
$MAPbI_3$	8	2700	1	Glass	NA	[135]
$MAPbI_3$	6.9	20000	1	Glass	11.26	[129]
$MAPbI_{3-x}Cl_x$	3.99	250	1	Glass	11	[130]
Triple Cation		2000	1	Glass	12.0	[43]
$MAPbI_3$	6.8			Glass	15.04	[44]
$MAPbI_3$		20000	1	Glass	11.42	[136]
Mixed Cation PVSK and SnO2				PET	18.8	[85]

7. Project Objectives:

The organo-metal halide PVSK that is the core layer of the PSC can be deposited using simple solution-phase processes at low temperatures. The high defect tolerance of the PVSK material makes it suitable for solution-phase deposition, making it a prime target for high volume, roll-to-roll manufacturing. Roll-to-roll of thin films is an established platform utilized in numerous industries and is capable of web speeds of 100 m/min. Utilizing small modifications to existing roll-to-roll printing press equipment across the globe, 100+ TW-scale production of PSC photovoltaics is achievable.[4] Thus the successful implementation of this technology via solution processable roll-to-roll can scale to meet anticipated demand. *The overall goal was to establish commercial relevance of radiative annealing techniques for manufacturing thin films for PSC in a roll-to-roll platform.* This must also necessitate newer materials that are also low cost (metal oxides) that can also be deposited directly on a PVSK. The outcomes were devices built at relevant throughput using the IPL technique. This leads to lower cost manufacturing through a smaller footprint and lowered electricity consumption.

The IPL process is ideally suited for roll-to-roll integration because it can reduce annealing dwell times to a fraction of a second. This directly impacts the cost of goods sold (COGS) through both the capital expenses (CAPEX) and operation expenses (OPEX) and allows for a much smaller footprint that should also improve the yields. The required line length can be several orders of magnitude shorter and in essence eliminates the largest piece of equipment in a roll-to-roll production facility. A shorter tool reduces web tension and errors associated with web alignment. The lower temperatures in the IPL will result in lower strains in the web. These will be expected to increase yields and uptime. The IPL also operates at a lower energy consumption, eliminating the thermal losses from traditional ovens. Finally, the costs of the IPL are nearly an order of magnitude less than a traditional oven.

PSC produced using roll-to-roll techniques at modest web speed costs between $0.02-$0.08 per Watt. This is less than the costs to produce c-Si cells ($0.19-$0.33 per Watt), which account for 54% of the module cost in 2018. The cost of producing a c-Si solar cell is expected to dip to just less than $0.10 in the next few decades.[137] During this time the efficiency, costs and durability of the PSC modules will continue to improve. Thus, the PSC will maintain a cost advantage at the cell level when compared to the dominant technology. However, this only accounts for the cell level and the balance of module (glass, encapsulant, junction box and framing) would be expected to reduce the cost advantage of the PSC technology at the module level. The balance of module costs for c-Si include the tabbing, encapsulation, framing, junction box and testing is estimated to add approximately $0.10 per Watt to the module. This yields a finished PSC module cost of $0.12 to $0.18 per Watt. At these costs, the PSC technology is indeed competitive with the existing crystalline silicon product and it is expected that costs from a roll-to-roll enabled manufacturing platform will continue to see costs reduce.

Budget Period 1

Task 1: Deposition and processing of CTL on top of PVSK thin film
Task Description: The primary objective of this task is to establish a method to deposit and process a CTL layer on top of the PVSK thin film. The deposition of layers onto the PVSK film is challenging because the material is susceptible to degradation from solvents and heat. These limitations have resulted in materials and processes that are cost-prohibitive and thus we will research means to economically deposit a CTL on top of the PVSK.

Subtask 1.1: Solvent/deposition engineering
Subtask description: The objective of this subtask is to determine the solvent-deposition interactions that will enable the deposition of a CTL on a PVSK. This will rely on the use of co-solvents that can be mixed with the CTL precursor chemistries making it more compatible with the direct deposition. This may be especially advantageous when used with a spray coating technique in which the primary solvent used to disperse the CTL evaporates prior to deposition.

Subtask 1.2: Functionalization of nanoparticles
Subtask description: The objective of this subtask is to determine what functionalization schemes allow for the deposition of the CTL on the PVSK. This will rely on the synthesis of metal oxide nanocomposites with protecting ligands such that they have improved solubility to solvents that will not damage the PVSK layer.

Subtask 1.3: CTL nanocomposites
Subtask description: The objective of this subtask is to determine what functionalization schemes allow for the deposition of the CTL on the PVSK. This will rely on building inorganic-organic nanocomposite films in which the nanoparticles yield the bulk of the electrical properties and the polymer bridges provides a more homogenous film. This is aided by the functionalization of nanoparticles.

Task 2: Baseline process
Task Description: The objective of this task is to establish the baseline process combining the deposition and annealing on the web. This will be done for the SnO_2 ETL chemistry and the PVSK chemistry. This will involve configuring the roll-to-roll coater and running optimization of the individual layers.

Subtask 2.1: Deposition of ETL and PVSK layers
Subtask Description: The objective of this subtask is to optimize the deposition of the initial CTL, which is deposited directly onto the substrate. The initial CTL will either be SnO_2 (n-i-p) or NiO (p-i-n). The PVSK material will utilize the triple cation system. These films will be deposited using a slot die technique. Work will include optimization of the chemistry formulation (dilution), web speed and material flow. The work will include XRD, XPS, UPS and UV-Vis spectroscopy techniques.

Subtask 2.2: Radiative annealing of ETL and PVSK layers
Subtask Description: The objective of this subtask is to optimize the radiative processing of the PVSK and initial CTL from subtask 2.1. The primary use of the IR annealing system will be to remove solvents from the films, which will initiate crystallization in the PVSK making in more amenable to the IPL. Parameters such as IR intensity, IPL intensity, pulse number and pulse width will be optimized.

Subtask 2.3: Baseline I-V characterization
Subtask Description: The objective of this subtask is to build cells from the deposited primary CTL and PSC stack. This will require the deposition of a secondary CTL on top of the PVSK to make a functioning solar cell. This will be done using a spin coating technique and available polymer chemistries for the secondary CTL (Spiro-MeOTAD, PTAA, and etc).

Subtask 2.4: Baseline durability
Subtask Description: The objective of this subtask is to demonstrate the baseline durability of the PVSK material under constant light load. Cells from subtask 2.3 will be placed into an inert atmosphere and exposed to 1000 hours of constant illumination. The performance of the cell at the conclusion of the 1000 hours will be compared to the initial.

Task 3: Technoeconomic model
Task Description: The objective of this task is to develop a technoeconomic model that will be continuously updated for the duration of the project using results from the technical tasks and inputs from stakeholders.

Subtask 3.1: Build technoeconomic model
Subtask Description: The model will consider the inputs of the materials (substrates, precursor chemistries, solvents and etc.), equipment (substrate handling, deposition, annealing and etc.) and energy (thermal, electrical and etc.) as well as the outputs of the PSC module product and waste (liquid and gaseous emissions, heat, scrap). The complete process will be decomposed into the discrete operations of the four layer depositions (including any interlayer components) and will consider any handling (storage, remounting and etc.) required between layers. The model roll up of the overall process will incorporate contributions related to yield and speed. The model will be initially developed on a spreadsheet and made available to all participants.

Subtask 3.2: Technoeconomic model refinement
Subtask details: The awardee will develop a model that is available on a spreadsheet or using other applicable feedback for its development. Once the model is completed, the results of the model will be distributed to two stakeholders from each class (module manufacturer, material supplier, equipment supplier) for a minimum of six stakeholders. The awardee will develop a survey to go to each of these stakeholders along with the results of the model. The survey questions will be written to get quantitative feedback on the applicability of the results of each pertinent section of the model. The awardee will also have a conference call between each stakeholder and the technical team to discuss directly any feedback, concerns or suggestions that they might have relative to the model.

Task 4.0: Optimize the deposition of the CTL on the PVSK
Task Description: The objective of this task is to validate an economically scalable method to deposit and process a CTL on top of the PVSK. We will use the information from the task 1 to inform a rational manufacturing process that may include more than one concept from task 1.

Subtask 4.1: Interfacial layers

Subtask description: The objective of this subtask will be to investigate the use of interface layers to improve the deposition of a secondary CTL on a PVSK. This will also investigate how the interface layer will also improve charge transfer at the interface.

Subtask 4.2: Design of experiments
Subtask description: The objective of this task is to combine the techniques developed to deposit the secondary CTL on the PVSK and optimize for cell performance. At the beginning of this task we will organize the results of the process/formulation/ functionalization schemes above as to the impact on the PVSK films and organize into a design of experiments (DOE). The process factors will include the functional parameters from the radiative process (energy density (ED), pulse duration (PD), pulse number (PN), pulse frequency (PF). This will allow us to quickly screen interactions between factors towards the functioning of the PVSK, CTL and interface. The dependent variables will determined using scanning electron microscopy (SEM), X-ray diffraction (XRD), photoluminescence (PL) and electronic impedance spectroscopy (EIS). The goal of the subtask is to demonstrate the secondary CTL process at the end of this subtask.

Subtask 4.3: Scribing ETL and HTL
Subtask description: The objective of this subtask is to evaluate the use of well-known scribing techniques to selectively scribe these layers. The films will be evaluated prior and after scribing for electrical resistivity using an I-V test.

Task 5: Stakeholder Engagement
Task description: The objective of this task is to engage stakeholders important to moving the results of this project towards commercialization. The stakeholders will include academia, national laboratories, equipment suppliers, materials suppliers and manufacturers. Virtual meetings will be organized with participation from relevant stakeholders, including but not limited to faculty, students, and NREL staff involved in this work as well as other stakeholders from equipment suppliers, materials suppliers and manufacturers. The meetings will center around defining any additional steps that need to be taken prior to commercialization of the technology. The goal will be fostering innovation and intellectual exchange amongst the technical team, small businesses and mature industrial partners who find value in the developing technology.

Budget Period 2

Task 6: Full cell integration
Subtask description: The objective of this task is to integrate the deposition and radiative annealing of the full PSC stack.

Subtask 6.1: Full stack production
Subtask description: The objective of this subtask is to complete the deposition of the individual layers for the cell and processing using radiative annealing. Cells from this subtask will be evaluated using I-V.

Subtask 6.2: End of project cell durability
Subtask description: The objective of this subtask is to demonstrate the end of project durability of the PVSK material under constant light load. Cells from subtask 7.2 will be exposed to 1000 hours of constant illumination. The performance of the cell at the conclusion of the 1000 hours will be compared to the initial.

Task 7: Stakeholder commitments
Task description: The awardee will engage with potential stakeholders relative to their interest in the technology and its potential commercialization. These early interactions will include phone calls, meetings and visits to their facilities. The awardee will also exchange samples as appropriate and where adequate disclosure protections can be put in place. As the award progresses, the awardee will seek commitments from these potential stakeholders in the form of in-kind donations of materials and testing/trials with our materials and modules. The awardee will aim at securing at least two stakeholder commitments for continued interest and interactions past the award period of performance. The awardee will also solicit samples from industry partners who are using different chemistries/architectures and demonstrate the radiative annealing on their samples.

Milestone table

#	Month of completion	Performance Metric	Success Value	Assessment Tool / Method of Measuring Success Value	Verification Process	Metric Justification, Additional Notes
1.3.1	3	Industry engagement	3 company contacts one each from equipment, materials and manufacturing	Begin the process of engaging industry members to be interested in the work.	Draft database including contact information and interest in project. Share with DOE	Will need industry buy-in by the end of project for commercial success
1.2.1	6	CTL and PVSK deposition	CTL 50 nm PVSK 350 nm	Characterization of the layer thickness of a deposited CTL on ITO and PVSK using slot dies.	SEM cross-sectional image.	Necessary to build a working cell.
1.2.2	18	Phase 1 (see appendix) cell ready for durability	1 cm^2 cell >10%	I-V characterization of 10 baseline samples.	Performance measured at UofL.	Necessary to begin 1,000 hour test.
1.1.1	15	CTL deposition on PVSK	PL/EIS	Demonstrate a stable PL and/or EIS of cell incorporating a CTL deposited onto a PVSK	PL and/or EIS data.	Needed to verify that a metal oxide CTL can be deposited onto a PVSK.
MP-T1.1	21	Cell Efficiency-Phase 1	1 m/min (ETL, PVSK) 1 cm^2 cell >12% +/- 4%	Average, standard deviation. I-V measurement of at least 15 cells samples randomly selected from a 1 m length web across and along the length of the web. Additionally, 3 cells will be selected from a second web run after a start/stop.	Measured by NREL's Device Performance Group. Data and report sent to DOE for verification	The test result was chosen to demonstrate that control of the deposition within a web and across webs using current device architectures.
MP-T1.2	21	Cell Stability – Phase 1	500 hours < 5% η loss (relative)	Efficiency ratio. Test 5 encapsulated cells (sealed in inert gas glass-glass capsule) under constant	Measured at NREL and/or UofL. Data and report sent to DOE for verification	Generally accepted as a first pass durability test for PSC cells.

#	Month of completion	Performance Metric	Success Value	Assessment Tool / Method of Measuring Success Value	Verification Process	Metric Justification, Additional Notes
				illumination with unregulated humidity. (Humidity to be monitored and recorded.)		
MP-CV1.1	18	Techno-economic model	Validated model	Model. Functional model of PSC manufacturing allowing for adjustments of inputs (materials, CAPEX, OPEX). Feedback from materials and equipment suppliers to be included.	Model sent to DOE for evaluation. Model will include validation/feedback from 2 stakeholders in each of the following categories: module manufacturer, material supplier, equipment supplier	Demonstrating that the technology can be scaled at a viable cost with inputs from stakeholders is vital to showing the path to commercialization
MP-SH1.1	12	Dissemination	Paper presentation	Presentation of the conceptual work at a major relevant conference	Accepted manuscript uploaded into OSTI (SEE FARC for more info about reporting requirements)	Presenting results early to these conferences offers opportunities to identify and meet with other stakeholders important to commercializing.
5.1.1	21	Virtual Meeting	Virtual meetings held	Count. At least 5 virtual meetings held with stakeholders.	Meeting minutes to be sent to DOE.	Necessary to establish the place and time to hold the conference in Louisville.
4.1.1	27	Interfacial layer determination	PL	Determination of necessity and advantages of interfacial layers between PVSK and secondary CTL.	PL measurement	Interfacial layers may be necessary to improve deposition and charge transfer to achieve higher efficiencies.
4.2.1	27	ETL and CTL layers	I-V curves of ETL and HTL	I-V curves of the ETL and HTL.	Measured at UofL or NREL.	These will be necessary to begin the evaluation of the scribing of these layers.
GNG1-T2.1	30	Cell Efficiency – Phase 2	2 m/min (ETL/ PVSK /HTL)	Average, standard deviation. I-V measurement of at least 15 cells samples randomly selected from a 1 m length	Measured by NREL's Device Performance Group. Data and report sent to DOE for verification	The test result was chosen to demonstrate that control of the deposition of the CTL

#	Month of completion	Performance Metric	Success Value	Assessment Tool / Method of Measuring Success Value	Verification Process	Metric Justification, Additional Notes
			1 cm^2 cell >16% +/- 3%	web across and along the length of the web. Additionally, 3 cells will be selected from a second web run after a start/stop		directly onto the perovskite meets market needs.
GNG1 - T2.2	30	Cell Stability – Phase 2	1,000 hours < 10% η loss (relative)	Efficiency ratio. Test 5 encapsulated cells (sealed in inert gas glass-glass capsule) under constant illumination with unregulated humidity. (Humidity to be monitored and recorded.)	Measured at NREL and/or UofL. Data and report sent to DOE for verification	Generally accepted as a first pass durability test for PSC cells.
GNG1 - CV2.1	30	Techno-economic validation	Feedback: from at least 4 stakeholders with a minimum of 3 representing industry	Written feedback with verification that techno-economic model fits technical targets and market expectations, Covering at a minimum materials and equipment costs, throughput, yield, life and efficiency. Stakeholders will include material and equipment suppliers and module manufacturers. Final roll-up will be cost per Watt for the module manufacturer.	Report sent to the DOE detailing the validation of the technoeconomic analysis based on stakeholder feedback.	Buy in from industry stakeholders of the technoeconomic analysis is critical to commercialization.
GNG1 - CV2.2	30	Processability	Successful scribing of CTL	I-V curve of the layer demonstrating that the electrical conductivity of the CTL is broken.	Measured at UofL. Data and report sent to DOE for verification.	The successful commercialization into a module may require that one or more of the CTLs can be scribed.
GNG1 -	30	Stakeholder engagement	Virtual meetings organized	Count. At least 5 virtual meetings held with stakeholders.	Meeting minutes to be sent to DOE.	Discussion amongst stakeholders across the

#	Month of completion	Performance Metric	Success Value	Assessment Tool / Method of Measuring Success Value	Verification Process	Metric Justification, Additional Notes
SH2.1			with relevant stakeholders			technology will be important to the commercialization.
7.1.1	33	Industry samples	Obtain 3 samples from industry	Obtain samples from at least one company developing PSCs for commercialization. These samples will be used to determine the applicability of the radiative annealing process.	Letter detailing the plan for transfer of materials.	Demonstration of the radiative process on industry relevant devices will help the success of this award.
6.1.1	36	Processing	>16% efficiency	I-V characterization	I-V measured at UofL.	Necessary to establish the EOP architecture and process.
6.2.1	39	Phase 3 cell ready for durability	Functioning baseline cell	I-V characterization of 10 EOP samples.	Performance measured at UofL.	Necessary to begin 1,000 hour test.
EOP-T3.1	42	Cell Efficiency – Phase 3	2 m/min (ETL/ PVSK /HTL/Metal) 1 cm^2 cell >18% +/- 2%	Average, standard deviation. I-V measurement of at least 15 cells samples randomly selected from a 1 m length web across and along the length of the web. Additionally, 3 cells will be selected from a second web run after a start/stop	Measured by NREL's Device Performance Group. Data and report sent to DOE for verification	Success value was chosen as this target represents a high average efficiency with a small deviation that will be important for commercialization.
EOP-T3.2	42	Cell Stability – Phase 3	1000 hrs < 10% η loss (relative)	Efficiency ratio. Test 5 unencapsulated cells under constant illumination with unregulated humidity. (Humidity to be monitored and recorded.)	Measured at NREL and/or UofL. Data and report sent to DOE for verification	Generally accepted as a first pass durability test for PSC cells.
EOP-CV3.1	42	Letters of intent	2	Count. A minimum of 2 letters of intent from relevant stakeholders committing to	Letters delivered to DOE	Success of the award will be measured by private entities willing to sell

#	Month of completion	Performance Metric	Success Value	Assessment Tool / Method of Measuring Success Value	Verification Process	Metric Justification, Additional Notes
				supply materials and/or equipment at the costs outlined in the technoeconomic model.		materials/equipment at competitive costs.
EOP-SH3.1	42	Memorandum of Understanding	1	Count. At least one memorandum of understanding to pursue funding to commercialize the technology.	Agreement sent to DOE	Success of the award will be measured by successful technology transfer to private entities.
EOP-SH3.2	42	Dissemination	Manuscript	Count. At least 2 manuscripts submitted for publication and one provisional patent application.	Accepted manuscript uploaded into OSTI (SEE FARC for more info about reporting requirements)	Dissemination of results through publications offers opportunities to alert the further community of the success of the project. Pate
EOP-SH3.3	42	Process Transferability	Industry Engagement with at least 2 partners	Count. Demonstrate the IPL process using materials and/or architecture supplied by third party industry partner. The minimum cell efficiency tested provided by the industry partner >20% and the IPL/IR process will not decrease the efficiency by more than 10%.	Letter attesting to the improvement in operation sent to the DOE.	Success of the award is to establish that the process can be ported to other materials and architectures.

8. Project Results and Discussion:

Task 1: Deposition and processing of CTL on top of PVSK thin film

The intent of this project is to deposit a metal oxide directly onto the PVSK film. Work to date has focused on both solvent systems as well as functionalizing the metal oxide nanoparticles. The work also included making devices based on these dispersions. The deposition of the SnO_2 has resulted in functional devices with efficiencies greater than 14%, whereas the NiO films have not produced a functional device. Therefore, the decision has been made to work with a p-i-n device architecture: PET/ITO/NiO/ PVSK /SnO_2/Ag. The current progress for this task is shown in figure 1.1, where the deposition of the SnO_2 on a PVSK is demonstrated. **The project team was the first to ever report the solution deposition of an SnO_2 layer directly onto a PVSK material.**[84]

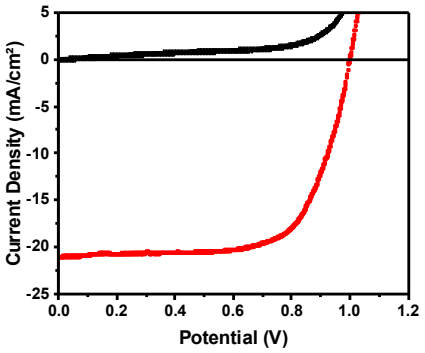

Material	Process	Anneal
SnO_2	Blade	plate
MAPI	Blade	plate
PTAA	Blade	plate
ITO PET (50 ohm/sq)		

0.25 cm²	V_{oc} (V)	J_{sc} (mA/cm²)	FF (%)	η (%)
Champion	1.00	21.1	68.0	14.5
Average	0.940	20.5	64.0	12.3
Std dev	0.050	0.92	3.00	1.10

Innovations

1. Synthesis of acetate stabilized SnO2
2. Deposition of solution SnO2 on perovskite
3. Yttrium Doping of SnO2 during synthesis

Next steps

1. Optimization of Yttrium concentration
2. Modification of PV/SnO_2 interface

***Figure 1.1**: Performance of SnO2 ink deposited directly onto a* PVSK *film.*

Subtask 1.1: Solvent/deposition engineering

Metal oxides exhibit good stability in polar solvents (water and alcohols) where Lewis bases can be used to alter the electric double layer to modify dispersibility. The PVSK antisolvents are typically an aprotic nonpolar solvent (chlorobenzene, toluene, and etc.). Thus, there is an incongruity for the choice of solvent to disperse a metal oxide for deposition directly onto a PVSK film; however, it may be advantageous to utilize a co-solvent system using the above solvents with vastly disparate properties. Our work has shown that the co-solvent system of ethanol (EtOH) and chlorobenzene (CB) can be used without damage to the PVSK. And furthermore, dispersions using 100% anhydrous ethanol can be accomplished in the blade coating process. Coatings of both SnO_2 and NiO have been attempted on the PVSK material to make devices. The SnO_2 materials have been shown to make devices up to 18%. The results from the NiO depositions do not show any observable damage to the PVSK film; however, devices could not be successfully built. **A suitable solvent system for the deposition of metal oxides directly onto a PVSK has been identified**.

Subtask 1.2: Functionalization of nanoparticles

Functionalization schemes for both SnO_2 and NiO have been studied to date. The functionalization schemes are solution phase and are accomplished from nanoparticles synthesized by the project team. This allows the in-situ doping of the metal oxides prior to the functionalization. SnO_2 has been functionalized with an acetate ligand and the NiO has been functionalized with a xanthate ligand. **The addition of the ligands has allowed these metal oxides to be dispersed into organic solvents that can be applied directly onto the PVSK layer without visible damage.**

SnO_2 Functionalization. A PVSK compatible SnO_2 ink was prepared by functionalization of SnO_2 nanoparticles to enhance dispersibility in non-aqueous solvents (Figure 1.2.1 a-c). Hydrous-SnO_2 was prepared from stannic chloride and sodium hydroxide according to established literature procedures.[138, 139] The hydrous SnO_2 nanoparticles particles were then reacted with acetic acid to yield SnO_2 functionalized with acetate (SnO_2-A) through ligand exchange.[139] XRD patterns indicates the ligand exchange reaction is purely a surface modification of hydrous-SnO_2 with no observable alteration of the crystal structure. The coordination of the acetate ligands to the metal oxide surface was confirmed by Fourier transform infrared (FT-IR) spectroscopy. Possible binding modes of the carboxylate ligand include monodentate, bidentate, or bridging.[140]

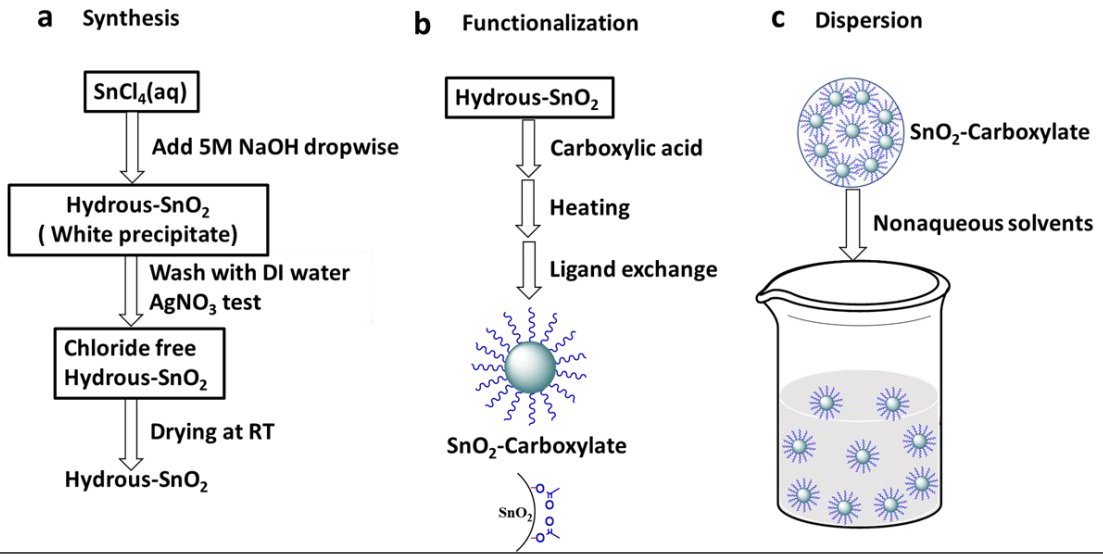

Figure 1.2.1: a-c) Schematic illustration of the synthesis of hydrous-SnO_2, functionalization of hydrous-SnO_2 with acetic acid to yield SnO_2-A, and preparation of a stable colloidal dispersion in anhydrous ethanol.

In contrast to hydrous-SnO_2, the SnO_2-A nanoparticles are readily dispersed in protic organic solvents such as ethanol and isopropanol. The enhanced dispersibility of the SnO_2-A particles in protic organic solvents is attributed to the formation of a hydrogen bonding network between the surface bonded acetate, excess acetic acid, and ethanol.[139] Although longer chain carboxylates would more effectively prevent agglomeration of the SnO_2 nanoparticles and enable the formation of a stable colloidal dispersion of SnO_2 in PVSK compatible non-polar organic solvents, the residual longer

chain ligand in the ETL would hamper the charge transfer process and reduce the overall efficiency of the PSCs. As such, we selected to functionalize SnO_2 with a short-chain carboxylic acid even though this limits our selection of solvents for the ink formulation to anhydrous ethanol.

NiO functionalization. Development of CB compatible NiOx nanoparticles with reduced alkyl chain lengths is here in undertaken. For this propose a series of alkyl xanthates (ROCS2-) of varying carbon chain length coupled with triethylamine (Et3N) have been prepared (Figure 1.2.6). Xanthates were selected due to their higher electron density in comparison to typical carboxylic acids. Each of the NiOx nanoparticles were suspended in CB and deposited by blade coating to form functioning p-i-n PSC devices that were evaluated in a solar simulator. The inks are also potentially applicable for the fabrication of n-i-p PSC devices. As an initial proof of concept, NiOx nanoparticles were deposited directly on the PVSK layer with no PVSK film degradation observed.

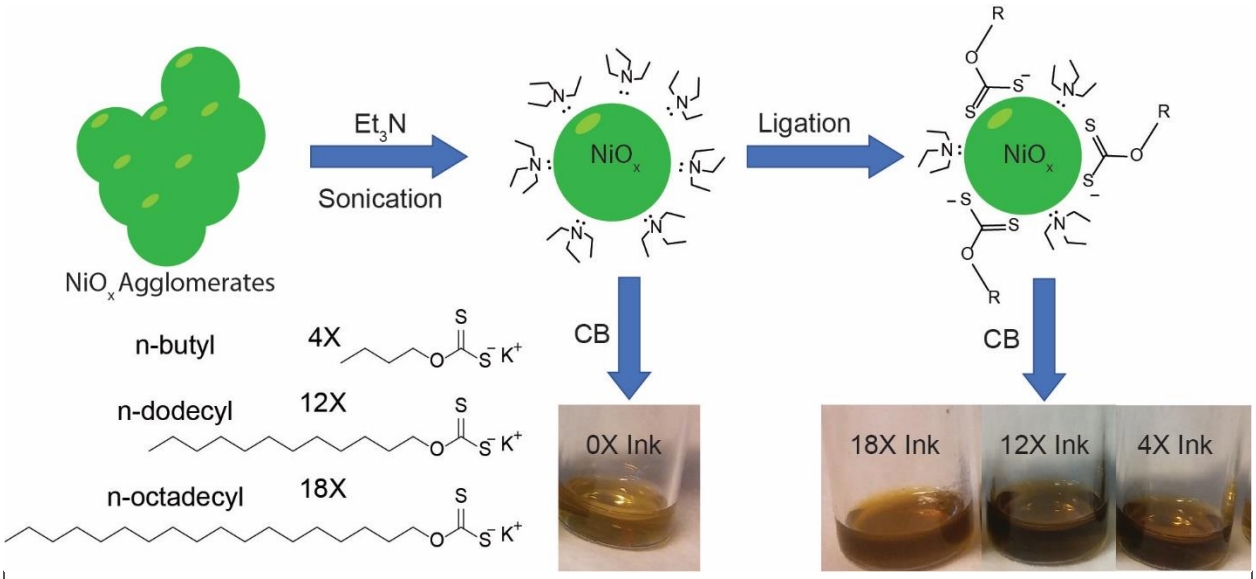

Figure 1.2.2: NiO synthesis and functionalization, hypothesized surface character and dispersions.

The NiO_x particles were synthesized by known solvothermal methods.[141] The potassium xanthates salts were prepared from potassium hydroxide, carbon disulfide, and the appropriate alcohol using reported methods. Xanthates with 4- and 12-carbon chains were isolated as yellow solids as described by Carta.[142] The 18-carbon chain xanthates was prepared as reported by Sawant as white solids.[143] The sodium carbonate salts were prepared as flaky, white solids from sodium phenoxide, carbon dioxide, and the appropriate alcohol according to the method reported by Ichiro.[144] A series of NiO_x nanoparticles have been prepared that can be readily suspended in CB as inks for the preparation of HTL with PSC photovoltaics. The NiO_x particles were initially ligated with the Lewis base triethylamine (Et_3N) to which alkyl xanthate ($ROCS_2^-$) ligands were added (Figure 1.2.2). The alky substituent on the xanthate was varied to evaluate the effect of carbon chain length on the ink properties and device performance. The various NiO_x particles are identified based on the length of the alkyl chain as follows: 0X (no xanthate), 4X (n-butyl xanthate), 12X (n-dodecyl xanthate), 18X (n-octadecyl xanthate).

To quantify the effect of Et_3N on the dispersion stability of the NiO_x particles, the ζ-potential was measured for the 0X solution. Prior to the addition of Et_3N, the ζ-potential of the initially prepared NiO_x particles was 6.19 ± 3.0 mV consistent with their observed agglomeration. Addition of 15% Et_3N to yield the 0X particles increased the ζ-potential to 27.29 ±3.9 mV. The results clearly indicate that Et_3N, *even in the absence of additional alkyl xanthate ligands*, is sufficient to stabilize the suspension of NiO_x in CB. Addition of alkyl xanthate to the 0X ink results in a ligand exchange process with coordination of xanthate to the NiO_x particles. While the 0X inks of the NiO_x particles are light tan to colorless in CB, the addition of alkyl xanthates yields dark brown suspension upon filtration (Figure 1.2.6).

Subtask 1.3: CTL nanocomposites

The functional schemes allow the nanopartciles to be dispersed into suitable solvents to allow these to be deposited directly onto a perovskite by blade coating. The functionalization of the SnO_2 using an acetate ligand has produced highly functional f-PSC with efficiencies greater than 18% on flexible PET substrates. The deposition of the NiO dispersion did not damage the perovskite, but did not lead to functional devices.

SnO2 Devices PSCs were fabricated with a p-i-n architecture employing SnO_2-A as the ETL. A series of planar PSCs were fabricated on indium tin oxide (ITO) coated glass with a polytriarylamine (PTAA) hole transport layer (HTL) and a poly[(9,9-bis(3'-(N,N-dimethylamino)propyl)-2,7-fluorene)-alt-2,7-(9,9-dioctylfluorene)] (PFN) interfacial layer. The overall device architecture is ITO/PTAA/PFN/$CH_3NH_3PbI_3$/SnO_2-A/Ag. The PTAA, PFN, and $MAPbI_3$ layers were also deposited using blade coating at ambient conditions.[120] The SnO_2-A layer was annealed for 10 min at 100˚C to remove solvents, and finally, silver was thermally evaporated as a top contact layer. The annealing process was optimal at 100 ºC and 10 min. Additionally, it was noticed that the PVSK undergoes degradation at a higher temperature, which limits the annealing of SnO_2-A deposited on the PVSK.

Figure 1.2.2 shows cross-sectional scanning electron microscopy (SEM) image of the proposed p-i-n device structure. Each of the individual layers can be clearly identified. Notably, there is no visible physical deformation of the PVSK layer due to the deposition of the SnO_2-A ink directly on the PVSK. Additionally, the SnO_2-A layer is compact, uniform, and without pinholes. The optimized thickness of the SnO_2 ETL was measured to be 36.7 ± 3.4 nm.

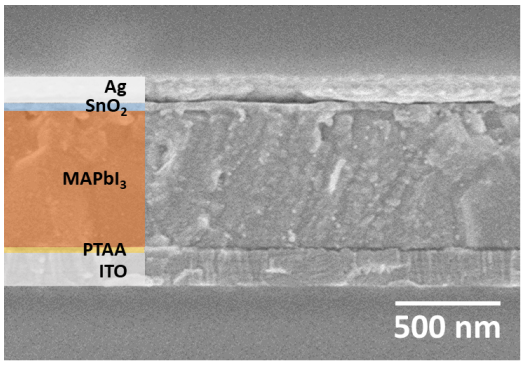

Figure 1.3.1. Cross-sectional SEM image of the full device.

NiO Devices Construction of a n-i-p device was undertaken with a glass/ITO/SnO_2/$MAPbI_3$/NiO_x/Ag architecture. The ETL, HTL, and PVSK layer were deposited by blade coating using the parameters described in experimental section. Upon deposition of NiO_x atop the PVSK the appearance of the stack shifted from a black mirror finish to a metallic blue with retention of its reflective nature. However, no functional devices were found upon solar testing. Evaluation of the $MAPbI_3$-NiO_x interface by PXRD shows the appearance of a peak at 9.5° (Figure 1.2.4) upon

deposition of the 0X ink on the PVSK. The same peak is observed when the ink solvent mixture (CB, EtOH, Et_3N) is deposited on the PVSK. This suggests the formation of a Et_3N adduct peak with the PVSK similar to that observed with DMSO.[145] Notably, no peak is observed at 12.7 indicating that $MAPbI_3$ is not degraded to PbI_2. Further work is ongoing to study this interface interaction and develop functional n-i-p devices.

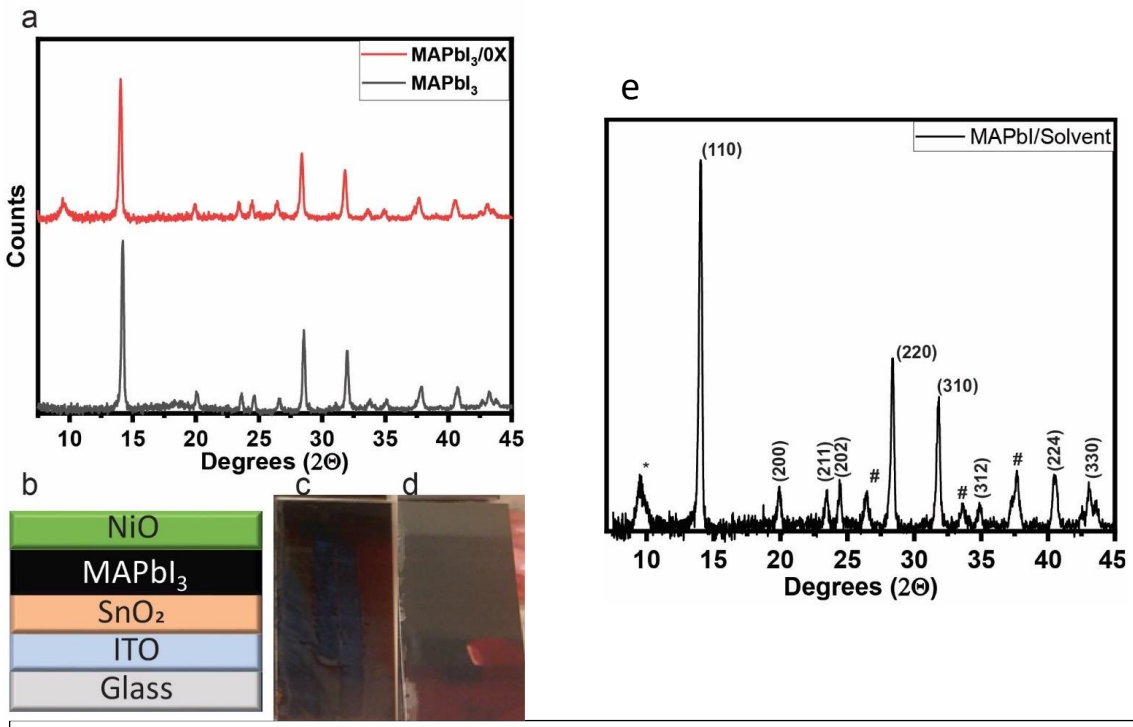

Figure 1.2.4: a) PXRD of perovskite film as prepared (red) and after deposition of 0X ink (grey) showing the formation of a new peak at 9.5° (*). B) Schematic illustration of n-i-p device stack. C) Image of the 0X coated perovskite. D) Image of perovskite film prior to NiO_x coating. e) PXRD of MAPbI3 on FTO (#) coated glass showing Et3N (*) adduct at 9.5˚.

Task 2: Baseline process

A schematic illustration of roll-to-roll slot-die coating deposition setup for this project is shown in figure 2.1. A corona discharge treater (CDT) (Enercon Industries CoronoFlex™) was added in the second quarter of 2021 to improve the wettability of the films. The ink is pumped using a SonoTek Syringe Pump TI that allows for a continuous flow of fluid at low flow rates. The fluid is deposited using a Premier Dies slot die with a shim thickness of 25 microns and a land length of 25.4 mm and the distance of the die to the web is precisely controlled using micrometers to 30-200 microns. The films are dried using an Exair model 110006 air knife using room temperature dry air at 30 psi. The substrate enters a 600 mm dry chamber that is fed with dry air to assist with the complete evaporation of the solvents. The dry section is used since humidity can exceed 60% for much of the year in Louisville, KY. The films are then annealed using a Xenon Sinteron S2210 IPL equipment. The web speed and tension are controlled using an integrated PLC. The overall footprint of the deposition and post-deposition setup is approximately 1 meter.

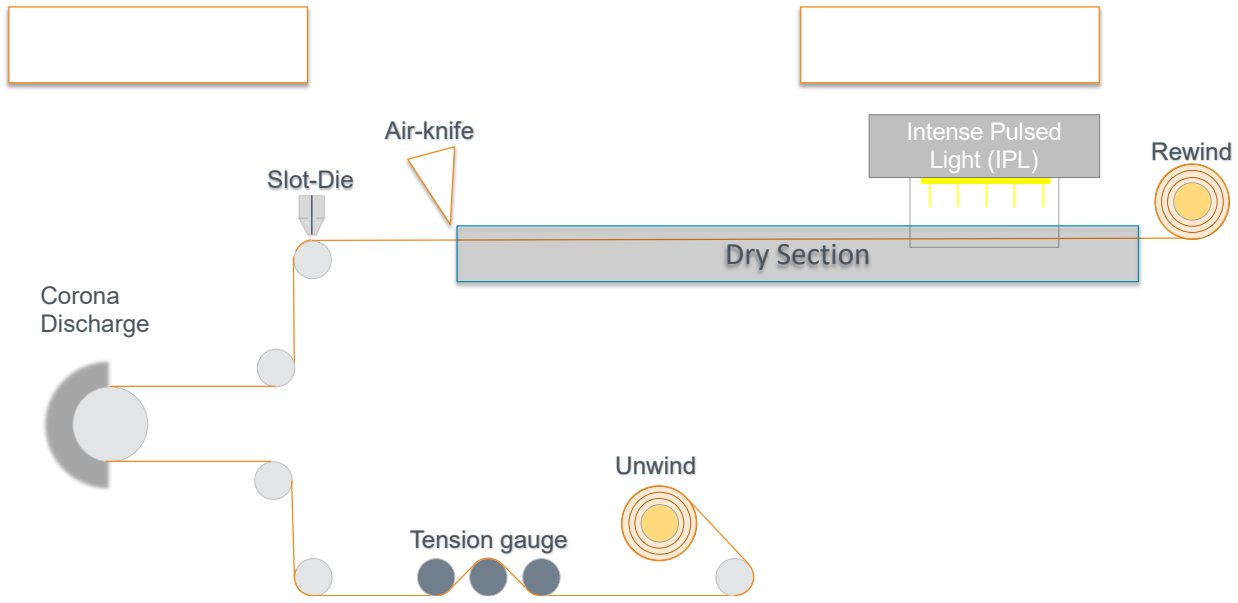

Figure 2.1: Schematic of the roll-to-roll setup for the deposition of individual films.

Three sperate thin films have been successfully deposited using the complete roll-to-roll setup including SnO_2, NiO and PVSK films. All of these films are deposited using the setup described in figure 2.1 and include thermal processing using the IPL. **Multi-layered devices from the roll-to-roll have been built up to 1 cm^2 with efficiencies greater than 11%. (**The ITO coated PET has a conductivity of 50 ohms/sq.) In addition to the roll-to-roll coater, a blade coater capable of high speeds is used to evaluate individual layers. The blade coater is placed in a humidity-controlled environment and operated at humidity below 30%, which aids in the deposition of the PVSK. Using this setup, 1 cm^2 devices of more than 13% have been established

Subtask 2.1: Deposition of CTL and PVSK layers

The deposition of the thin films requires optimization of the ink chemistry, surface energies, web speed and tension and slot die parameters. The films for deposition are extremely thin (CTLs at 20-50 nm and the PVSK at 400-700 nm), thus the inks tend to be very solvent rich and very little pressure is required to push through the slot die. Inks were developed to have a high stability to allow for more time between formulation and deposition. Surface energies can be controlled using a CDT. **To date inks for SnO_2 ETL, NiO HTL and PVSKs (MAPI and triple cation) have been developed and deposited using the roll-to-roll coater.**

ETL. The SnO_2 ETL layer was optimized to deposit by roll-to-roll printing method. The SnO_2 precursor solution was prepared by diluting the commercial SnO_2 solution with DI water and anhydrous ethanol (1: 6: 3 vol. ratio) having a trace amount (15 µl) of Triton X 100 surfactant to improve wettability. Here, the amount of surfactant was also optimized to obtain a continuous uniform SnO_2 films. The slot die is set at a height of 40 microns from the web. Prior to the deposition, the substrates were subjected to UV treatment to

alter the surface free energy and cleaning which improves the adhesion of precursor solution. Then, roll to roll deposition was carried out at different solution flow rates and web speeds, followed by drying with cold air knife and subsequently annealed using IPL with different pulse rates, durations and energies. As deposited SnO_2 films by roll-to-roll coating, and its corresponding IPL annealed parameters are shown in table 2.1. The thickness of as roll to roll deposited SnO_2 films was measured using a Veeco Dektak 8M stylus profilometer from different locations across the web and it was found to be an average thickness of 48 ± 7 nm.

Table 2.1.1 Deposition, IPL parameters and thickness evaluation of roll-to-roll coating of SnO_2

Roll to Roll deposition		IPL annealing				Stylus Profilometer
Web speed (mm/min)	**Flow rate (ml/min)**	**Energy (J/cm²)**	**Voltage (V)**	**Duration(µsec)**	**Delay (msec)**	**Thickness (nm)**
2000	1.9	1.22	1940	1000	200	48 ± 7

NiO. To study the quality of the NiO_x film devices of architecture PET/ITO/Cu:NiO_x/ $MAPbI_3$/C_{60}/BCP/Ag and 0.25 cm^2 area. To date our highest performing NiO_x devices by slot die coating has a PCE of 11.2% with a J_{sc} of 20.4 mA/cm^2, V_{oc} of 0.950 V and FF of 57.7%. By blade coating our highest device has a PCE of 9.00%, $J_{sc,}$ of 18.2, V_{oc} of 0.92 and FF of 53.8%. The JV curves (Figure 2.1.1) clearly show the behavior of the curve near the $V_{oc,}$ which shows a double diode behavior, and the decrease in J_{sc} are the primary differences between the films. The double diode behavior of the blade coated film has been associated with the thickness of the NiO_x film. When the HTL layer is to thick or thin it can cause charge build up at the film interface inducing a secondary diode behave decreasing the device V_{oc} and FF.

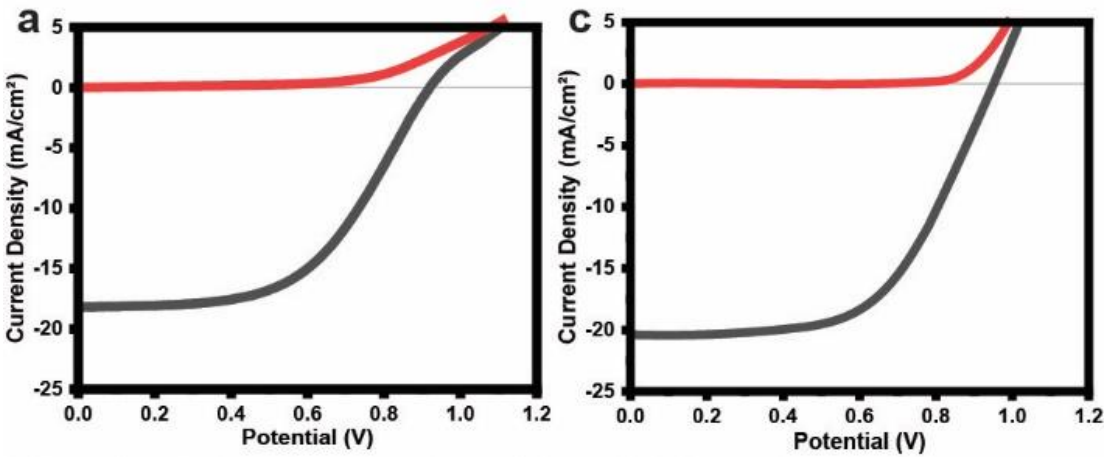

Figure 2.1.1 a) Top JV curve of blade coated Cu:NiO_x and b) associated SEM image of film. c) Top JV curve of slot die coated Cu:NiO and d) associated SEM image of film

PVSK. In earlier attempts, roll to roll deposition of active PVSK layer was optimized using different solvents such as DMF, DMSO, acetonitrile and 2-Methoxyethanol and also explored with different surfactants (SDS, Tween C60, and L -α phosphotidylcholine) for getting homogenous and pinhole free PVSK films. After numerous attempts, the deposition of PVSK films was optimized having a solvent chemistry of 3:2 vol. ratio of acetonitrile (ACN) and 2-methoxyethanol (2-MeOH) containing 20 mol.% of L -α phosphotidylcholine (LP) surfactant and DMSO. Prior to the depositions, ITO coated PET substates were subjected to UV treatment to remove organic residue and to alter the surface free energy for improving the wettability and adhesion of PVSK films. As deposited films were dried using cold air knife pass, and subsequently annealed by IPL for attaining crystallinity in PVSK thin films. The obtained PVSK films were characterized using XRD, SEM, UV-visible measurements and thickness was also measured using surface profilometer.

Table 2.1.3. Deposition, IPL parameters and thickness evaluation of roll-to-roll coating of PVSK film

Roll to Roll deposition		IPL annealing				Stylus Profilometer
Web speed (mm/min)	**Flow rate (ml/min)**	**Energy (J/cm^2)**	**Voltage (V)**	**Duration(μsec)**	**Delay (msec)**	**Thickness (nm)**
1800	1.9	0.37	1500	600	1000	800 ± 50

The deposition was carried out with a flow rate of 1.9 ml/min and at web speed of 1.8 meter/min and subsequently dried with cold air knife pass and followed by IPL treatment. The thickness of as roll to roll deposited PVSK films were measured using stylus profilometer from different locations across the web as shown in table 2.1.2 and it was found to be an average thickness of 800 ± 50 nm. Optical images of as deposited PVSK films are shown in figure 2.1.2 b&c.

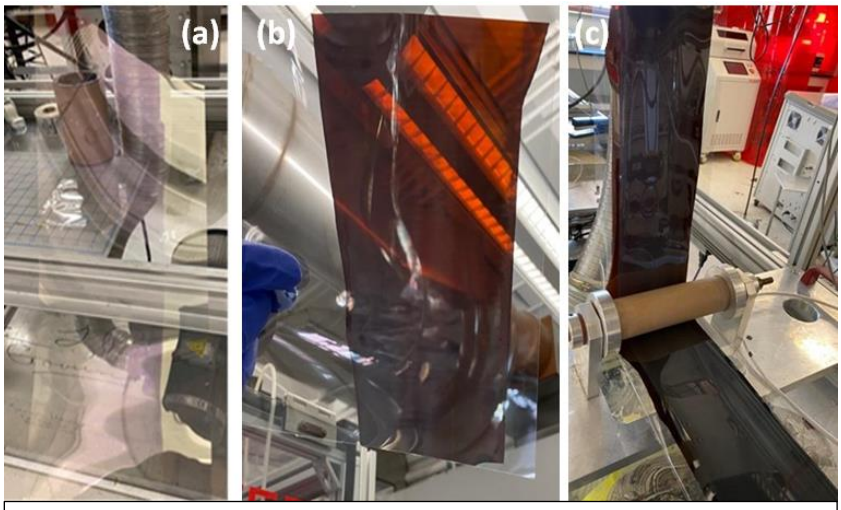

Figure 2.1.2*:* Optical images of as deposited (a) SnO2 and (b) and (c) perovskite films

Subtask 2.2: Radiative annealing of CTL and PVSK layers

The IPL process involves the absorption of light energy into a thin film from an intense rapid pulse with a broad spectrum covering large areas. A thin film with high absorptivity within the spectrum of light will absorb the radiative energy, which is then rapidly transformed into thermal energy. The advantage of this technique for polymeric substrates is that it can generate very high temperatures within a thin film without damage to the plastic.

SnO2 To understand the IPL annealing of SnO_2 films over ITO/PET flexible substrates for obtaining high crystallinity and should be capable of charge carrier transportation. At the initial stage, different energy pulses, flash counts and delay times were applied to ensure evaporation of all the water content and enhance the crystallization of SnO_2 nanoparticles. It is known that charge carrier transportation depends on the degree of crystallization which relies on applied IPL energy vales. During optimization, different energy values 0.6, 0.8, 1.0 and 1.2, and 1.4 J.cm2 were applied to obtain uniform and defect free SnO_2 films. At the lower energies, it was observed that more gaps and defects over the film and at high energies noticed a cracks on the SnO2 films. Thus, after numerous attempts, the optimum IPL energy was found to be 1.2 J/cm2, at this, obtained a uniform, defects and cracks free SnO2 films. The resulting films exhibited higher Voc values close to 1.0V (see subtask 2.3) in their corresponding devices.

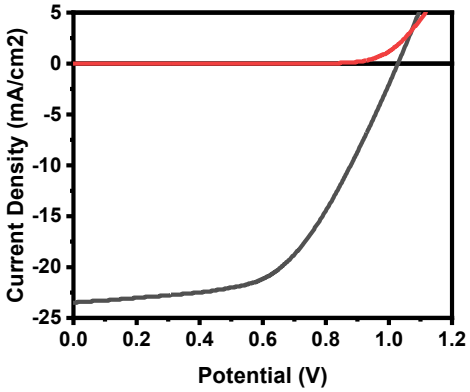

Material	Process	Anneal
Spiro	Spin	N/A
MAPI	Blade	IPL
SnO2	Roll-to-roll	IPL/CDT
ITO PET (50 ohm/sq)		

1 cm²	V_{oc} (V)	J_{sc} (mA/cm²)	FF (%)	η (%)
champion	1.03	23.5	55.0	13.2
average	1.01	22.3	50.1	11.3
Std dev	0.01	3.29	3.71	1.58

Innovations

1. SnO_2 film annealed in line with IPL

Next steps

- CDT optimization

Figure 2.2.1: Performance of SnO2 by roll-ot-roll slot die deposition and IPL processing.

NiO: It was expected that the same energies used for the SnO_2 annealing would be ideally suited for the NiO films as well. One should note that the method of post deposition annealing affects the composition, work function, and hole extraction capability which accelerates Voc values up to 1.1 V. IPL annealing is used for the post-treatment of NiOx films which is compatible with roll-to-roll manufacturing. IPL offers

short and intense energy pulses of light to process materials at a high speed. At the initial stage of processing of NiOx films different energy pulses, flash counts and delay times were executed to obtain fully dry and uniform films with improved crystallinity. In the process of optimization different energy pulses (0.4, 0.8, and 1.2 J/cm2) having different delay times (200, 600, and 1000 msec) were applied to obtain uniform and defect free NiOx films. Among these, it was found that the same energies used for the SnO2 annealing are nearly suitable for the NiOx films as well for obtaining uniform and crystalline films. Thus, the resulting films exhibited Voc values up to 0.95 V in their corresponding devices as shown in figure 2.2.2.

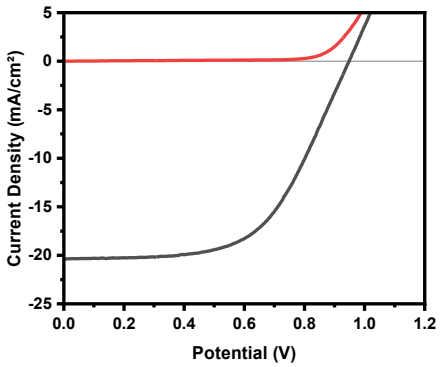

Material	Process	Anneal
C60	Evaporated	N/A
MAPI	Blade	IPL
Cu:NiO_x	Roll to Roll	IPL
ITO PET (50 ohm/sq)		

0.25 cm^2	V_{oc} (V)	J_{sc} (mA/cm^2)	FF (%)	η (%)
Champion	0.950	20.4	57.7	11.2
Average	0.906	19.8	54.8	9.86
Std dev	0.047	0.63	2.41	1.02

Innovations

- Doped with Cu to improve V_{oc} and FF
- Precipitation of NiO to remove organics

Next steps

- Film roughness reduction
- CDT treatment of NiO
- Interface engineering

Figure 2.2.2: Performance of NiO by roll-to-roll using slot die deposition and IPL processing.

PVSK: Roll-to-roll manufacturing coupled with IPL processing addresses many of the scalability concerns surrounding the perovskite technology. To make this technique a reality, the ink formulation needs to be tailored to the process. This can be accomplished through incorporation of additives and judicious selection of solvents. There are a few main functions that these modifications must address to be selected in the precursor chemistry. First, the additive must increase the intermediate absorption profile throughout the visible light spectrum. Second, the additive must undergo a reaction or participate in solute-solvent interactions that result in improved surface morphology or stabilization of the PVSK material. Lastly, solvents that increase the intermediate absorption through visible wavelengths will be considered. Most commonly, solvent- PVSK adducts yield consistent, high-quality PVSK films by retarding crystallization and reducing horizontal grain boundaries that result from disordered crystallization mechanisms.

Solar cell devices were assembled from the optimized roll-to-roll slot die coated and IPL processed SnO_2, and PVSK films chosen from the five locations across and down the web as shown in figure 5a. The champion device exhibited a PCE of 11.2% with a V_{oc} of 0.91 V, Jsc of 23.7 mA/cm^2, and FF of 52 % over an active area of 1 cm^2 as shown in figure 6a. The low performance of the large area devices in PET substrate is due to the decrease in V_{oc} and FF attributed to high sheet resistance of the PET-ITO substrate. A statistical distribution of the performance from the ten 1 cm^2 devices (active area 1 cm^2) collected from each of the five locations is shown in figure 6b. An average stabilized PCE of 10.6% was obtained with an average open circuit voltage (V_{oc}) of 0.97 V, current density (J_{sc}) of 22.9 mA/cm^2, fill factor (FF) of 47%. The FF and the Voc are lower than expected and can be attributed to the thickness of the PVSK and ITO layers. A thicker PVSK layer will reduce the FF and Voc due to a higher charge recombination. The thickness of the ITO layer on the PET yields a resistance of 50 Ω/sq and decreases the FF as is evident from the slope of the J-V curve showing high series resistance.

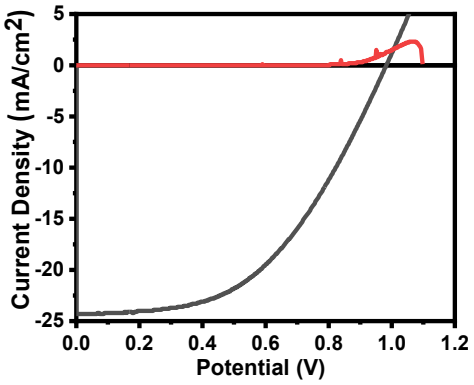

Material	Process	Anneal
Spiro	Spin	N/A
MAPI	Roll-to-roll	IPL
SnO2	Roll-to-roll	IPL/CDT
ITO PET (50 ohm/sq)		

1 cm^2	V_{oc} (V)	J_{sc} (mA/cm^2)	FF (%)	η (%)
champion	0.98	24.3	49.0	11.8
average	0.96	20.2	50.0	10.3
Std dev	0.03	1.46	2.91	1.26

Innovations

1. Very rapid annealing by IPL
2. Small footprint (~30 second annealing)

Next steps

- Improve perovskite deposition

Figure 2.2.3: *Demonstration of roll-to-roll coated baseline devices using slot die deposition and IPL*

The characterization techniques like SEM, XRD and UV-visible spectroscopy of as deposited PVSK films are shown in figure 2.1.3 and figure 2.1.4. From SEM, it shows that slot-die coated PVSK films exhibited uniform and compact layers having very minimal pin holes with an average crystal size of ~400 nm. These are the best morphologies for slot-die coated PVSK films as the function of IPL annealing by eliminating conventional hot air ovens and thermal hot plates. It is noteworthy to mention that crystallization of roll to roll slot-die coated PVSK film is strongly influenced by the precursor solvents, drying and annealing conditions. The presence of minimal pinholes on the film effected the photovoltaic performance by decreasing the fill factor due to low shunt resistance.

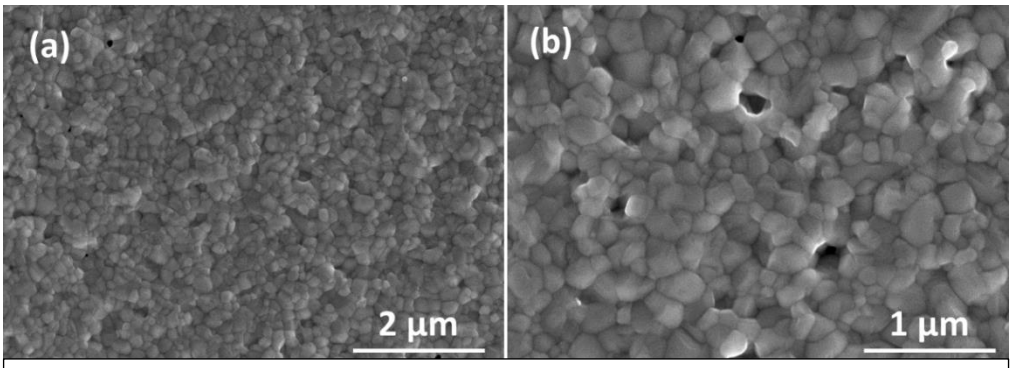

Figure 2.1.3: (a) and (b) SEM images of roll-to-roll deposited PVSK films as a function of IPL annealing.

To further investigate the quality of roll-to-roll slot-die coated PVSK films, Uv-Visible absorption, and X-ray diffraction (XRD) analysis were carried out and their corresponding spectra are shown in figure 2.1.4. In this, the absorbance was measured from different locations of the slot-die coated PVSK film (~2 meters length) across the 6" web as obtained out of roll-to-roll deposition as shown in figure 2.1.4a and b. It is clearly seen that the trend of absorption is uniform from all over the film at different random locations along the web and is indicating that the slot-die coated PVSK film is uniform. It was also found that the thickness of PVSK film is nearly uniform across the whole web and an average thickness was found to be approximately 850 nm. Besides, as shown in figure 2.1.4d, the XRD also exhibited a same peak at 14.2^0 corresponding to (110) crystal plane of the tetragonal phase of PVSK structure from all the different locations as specified across the web, and no other additional peaks were detected. It confirms the full conversion of precursor to PVSK phase throughout the deposition.

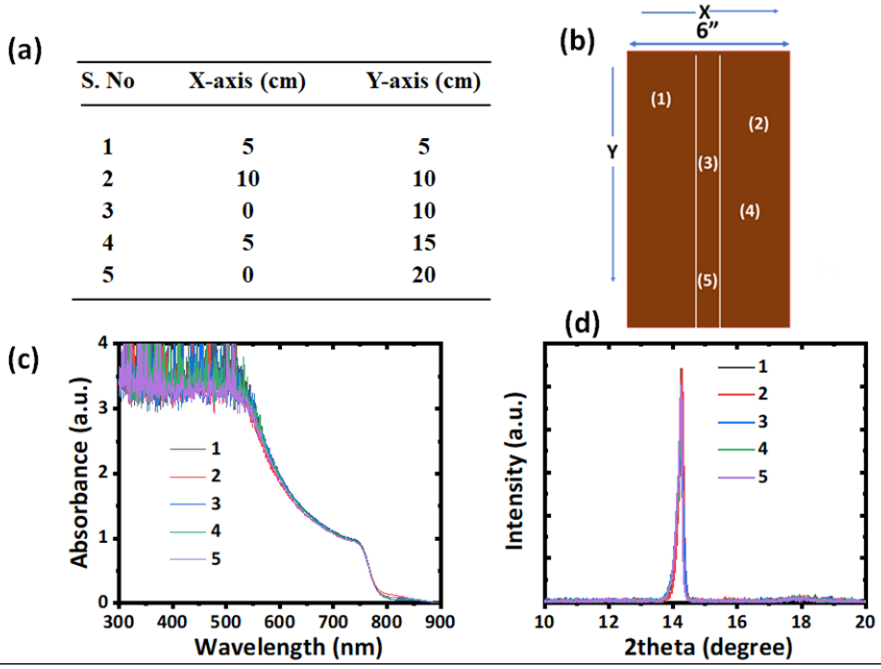

Figure 2.1.4. Uv-Visible absorbance of R2R slot-die coated perovskite films, a) from different locations of the web, b) optical image specifying different locations, c) and d) corresponding absorption and XRD spectra

Subtask 2.3: Baseline I-V characterization

The team is constructing primarily 1 and 0.25 cm^2 devices. After deposition of the three layers (ETL, HTL and PVSK) a section of the web is cut to prepare devices. The chosen areal device is isolated by removing the three layers using a swab soaked in GBL (using a mask). The samples are then loaded into a thermal evaporator to deposit the metal contact (which may include a contact layer such as MoOx or BCP). A typical MoOx buffer layer with a thickness of 8 nm and a final top contact silver (Ag) with a thickness of 80 nm are deposited by thermal evaporation having a shadow mask of an active area of 1 cm^2. The photovoltaic performance of devices was measured using Oriel class AAA solar simulator equipped with Xenon lamp having one sun condition (100 mW/cm2, AM 1.5G), prior to the actual device measurements, NREL certified silicon solar cell was used for the calibration. Schematic representation of the device stack is shown in Figure 2.3.1. **To date 1 cm^2 devices with efficiencies over 13% have been produced.**

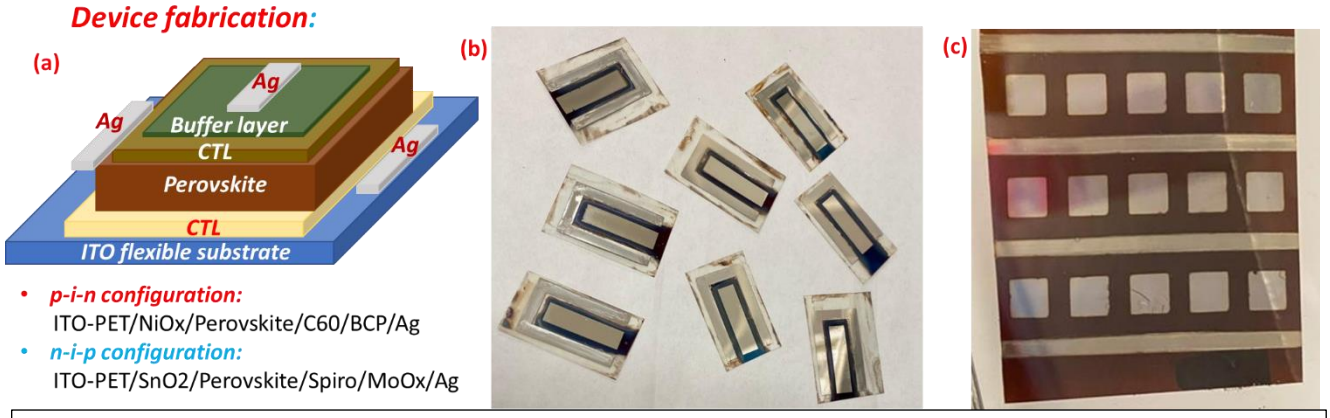

Figure 2.3.1: (a) Schematic representation of device architecture and (b) and (c) optical images of as fabricated devices at the time of I-V measurements having an active area of 1 cm^2 and 0.25 cm^2 respectively.

Subtask 2.4: Baseline durability

Current state-of-the-art for MAPbI3 PVSK device stabilities have demonstrated >95% normalized PCE over 1000 hours under constant illumination.[146] This study utilized a metal oxide hole-transport material and multiple measures to encapsulate the device.

To understand the stability of the fabricated device, sample devices were stored in a nitrogen flow box after initial J-V measurements were recorded. The devices were stored without any encapsulation and the J-V characteristics were re-evaluated after 40 days. Figure 2.4.1 shows the device performance statistics of the stability test. After 40 days, 95.8% of the average initial efficiency was retained. The loss of efficiency is mainly due to a decrease in J_{sc}, which decreased by 15.59% on average. Interestingly, the average V_{oc} and FF values increased by 4.85% and 8.42%, respectively, after storage. There is no clear mechanism that explains the increase in V_{oc} and FF over

time. Possible factors include age-induced recrystallization of the PVSK, strain reduction of the PVSK thin film, and/or disappearance of the trap state.[147, 148]

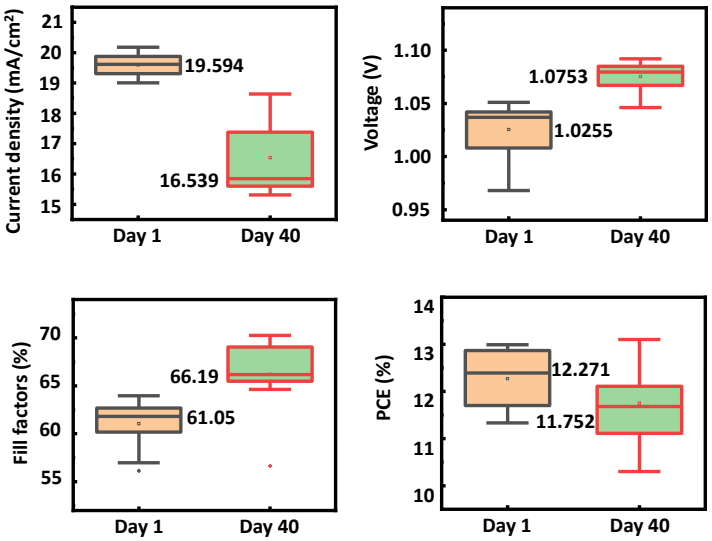

Figure 2.4.1. Stability study J-V characteristics of unencapsulated p-i-n devices before (1) and after (2) storage for 40 days in a nitrogen flow box.

ISOS-L1I protocol proposes that the devices be maintained under a constant light intensity (0.6 – 1 sun) in an inert atmosphere. This is a wide parameter space of durability testing within which valuable insights can be obtained at different conditions. This type of stability testing does not necessitate strict standardized testing conditions because the focus of this test is to elucidate and probe the material-specific stability regimes as well as fundamental degradation mechanisms. The tests can therefore be

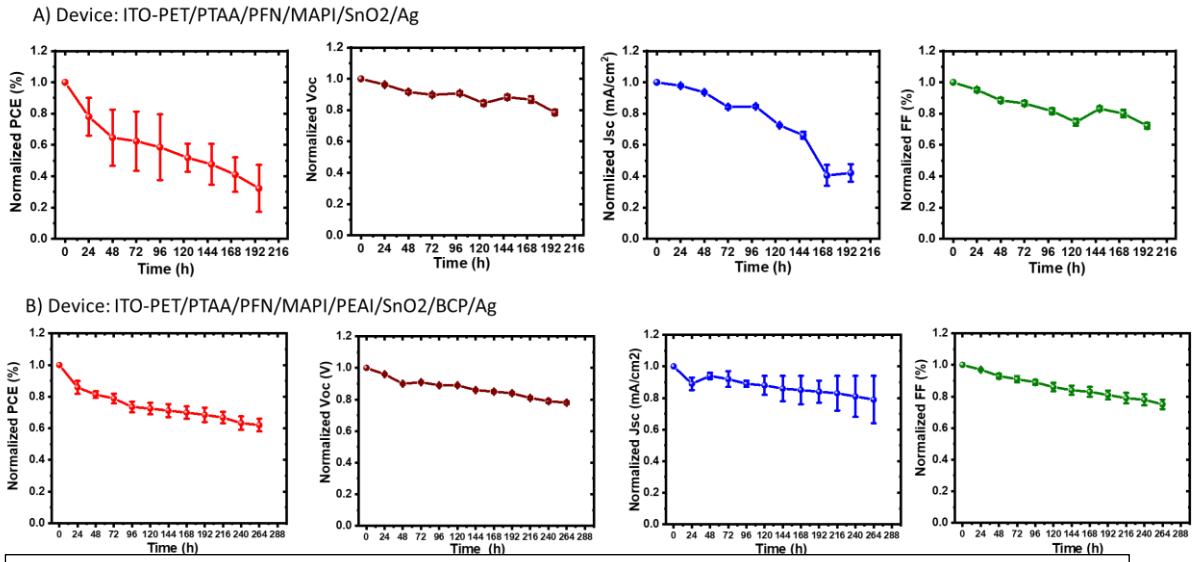

Figure 2.4.7. Durability measurements of two different device stack for more than 100 h. a) ITO-PET/PTAA/PFN/MAPI/SnO_2/Ag for 196 h, b) ITO-PET/PTAA/PFN/MAPI/PEAI/SnO_2/BCP/Ag for 120 h, c) and d) optical images of device

tailored to answering material-specific questions rather than the operating mechanism of the solar cell. Based on this approach, the team is investigating the process of photoinduced halide segregation in halide PVSKs and interaction process of top metal electrodes with PVSK structures upon continuous light soaking.

Two different device stacks were subjected to durability measurements for more than 250 h. The device stack having configuration of ITO-PET/PTAA/MAPI/SnO_2/Ag has exhibited a faster degradation, in which the initial PCE was 13.6 % and it was degraded to 4.38 % after 196 h, the corresponding measurement curve is shown in figure 2.4.7a. There were significant losses of V_{oc}, and J_{sc}, a minimal loss of FF, where all these collectively effect the overall PCE. The degradation was due to the interaction of Ag metal and PVSK layer as shown in figure 2.4.7c, thus the metal diffuses into the PVSK layer and react with the PVSKs at grain boundaries which results in the formation of an insulating layer (Ag halides) and finally decomposes the PVSK structure. The second device configuration consists of ITO-PET/PTAA/MAPI/PEAI/SnO_2/BCP/Ag is subjected to durability study for more than 250 h. In which the initial PCE was about 15 % and after 264 h, the PCE was dropped to ~9%. As shown in figure 2.4.7b, it was found that this device configuration has exhibited relatively higher stability in comparison to the first device configuration. It is due to an extra layer of PEAI (Phenyl ethyl ammonium iodide), which inhibits the ion migration and reduces the interaction between top Ag metal contact and PVSK film.

Task 3: Technoeconomic model

A technoeconomic model has been developed and discussed with a number of stakeholders. The model has been published.

Subtask 3.1: Build Technoeconomic model

PSC technology is an economically viable photovoltaic based primarily on low cost of materials and scalable manufacturing. Solution phase deposition of all active layers lends itself towards roll-to-roll which is a well-established platform with production rates of several hundred square meters per minute. In this reporting period, the opportunity to scale at this production throughput was considered with manufacturing exceeding 1 GW per year in a single plant. The use of intense pulsed light is utilized to minimize costs associated with the footprint, equipment and operation. The analysis is limited to the operation of the roll-to-roll with the product being a PSC solar film that can be incorporated into modules and focuses primarily on the deposition, drying and annealing of the films. Costs associated with materials, equipment and operations are considered with utilities costs determined from the fundamental engineering calculations. The results show that at very large-scale operations, the costs to produce the solar films range between $0.02-$0.08 per watt.

The techno-economic analysis considers the cost of goods sold (COGS) for a roll-to-roll manufacture of PVSK films considering the flow chart in Figure 3.1.1. The model considers the use of intense pulsed light as a post-deposition step for multiple layers of the device and includes the use of fundamental engineering and economic analysis of materials and energy inputs. The roll-up of the COGS for the proposed process was then compared to an existing process that is prevalent in the roll-to-roll manufacturing community. Data is presented for production throughputs of several GWs of yearly

production in a single factory at web speeds of up to 40 m/min. A novel aspect of the work involves the use of IPL as an annealing step and the savings in energy and facility size (footprint) will be discussed. Consideration of the processing is described in three discrete operations: deposition, drying, and annealing. The deposition is a solution phase deposition by slot die, the drying accomplished using air knives, and the annealing using IPL.

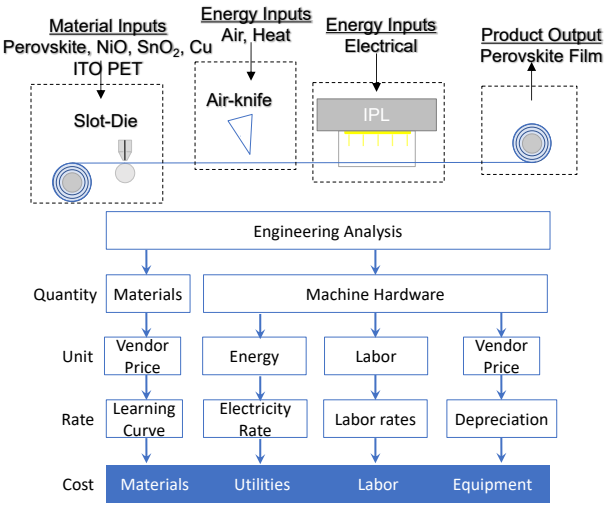

Figure 3.1.1: Flow chart explaining the overall methodology of the techno-economic analysis. This includes the deposition, drying and post-processing using IPL of the four layers (SnO_2, PVSK, NiO and Cu). A fundamental engineering analysis of each process informs the design of the equipment, utilities and labor. All of these including the material inputs are considered for the overall roll-up of the cost of goods sold.

The analysis was developed to compare the costs of implementing the IPL as a viable thermal annealing processing step within a roll-to-roll manufacturing platform. The promise of roll-to-roll processing is related to the throughput with web speeds of over 100 m/min achieved within the film industry. These achievable web speeds of a single tool could produce near 1 GW per month or the equivalent of a year's worth of operation at a major crystalline silicon (c-Si) manufacturing plant. Therefore, in order to establish the true opportunities for roll-to-roll manufacturing of PSCs, it is most advantageous to design manufacturing plants at roll-to-roll capable production speeds. To establish the costs at these scales for the IPL process it was necessary to first determine the costs associated with the materials since previous analysis stop at 1 GW production.

The roll-to-roll production of the PSC modules in this analysis does not include the final stages of manufacturing that would include the encapsulation of the module, framing and or addition of the junction box. This is somewhat analogous to the manufacture of c-Si photovoltaics, which typically assumes that the cell is a material input to the module. In the case of the c-Si production, the size of the cell and modules are bounded by small aspect ratios due to considerations in manufacturing and installation. In a roll-to-roll manufacturing technique the width of a roll would be about 1.5 meters, whereas the length can be considered infinite. Thus, the costs from this analysis are for a PSC coated film which can be compared to the costs to produce a c-Si solar cell. The comparison is not quite one-to-one as the tabbing of the PSCs is accomplished during the roll-to-roll and costs ~$0.01 per watt for the production of a c-Si module. [137]

Each 1 GW production requires approximately 6 million m^2 of solar cell area and would require a modest web speed of 9.7 m/min, which is well within the limits of roll-to-roll technologies. The overall cost of production follows the standard asymptotic relationship in which the COGS is dominated by the materials at higher production capacity (Figure 3.1.2). The curves bound the COGS of the PSCs assuming conservative and modest

learning rates for the materials and will be discussed in more detail in the following paragraphs. The small bumps in the curve are caused by the addition of the extra equipment and labor at each 1 GW production. From this analysis, the graph of COGS starts to flatten out at around 3 and 4 GW. This demonstrates that the scales at which roll-to-roll becomes competitive with prevailing technologies far exceeds the capacities ($0.30/W, at ~100MW) considered to date.[149] This has some major implications towards the capital and operation expenses that will be discussed in Equipment Costs and Utilities sections below.

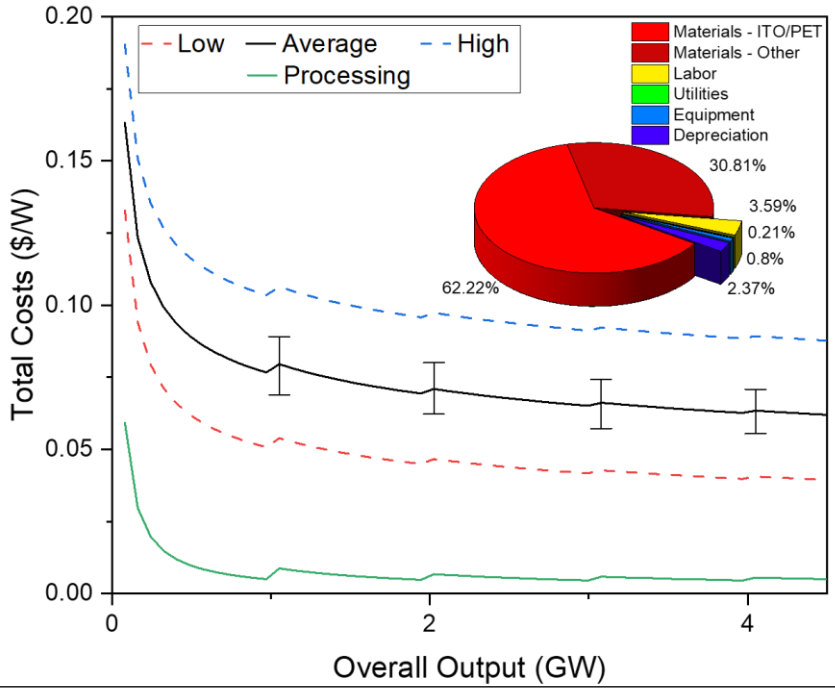

Figure 3.1.2: Manufacturing costs of PSCs based on annual output. The curves bound the upper and lower cost estimates using a modest and conservative learning rates applied to the ITO coated PET. The bars on the average curve includes 95% confidence intervals from the Monte-Carlo analysis. The lowest curve shows the costs associated with processing (equipment, labor, utilities, & depreciation). (inset) Contribution to overall costs at 2 GW production using the average learning rate applied to the ITO coated PET.

Materials Costs The overall costs of the production of the PSCs is dominated by the materials exceeding 85 percent of the COGS. The major cost component is the ITO coated PET representing over 75% of the material costs. Developing cost estimates for ITO coated PET is difficult and hence three learning rates (15%, 10% and 7% for the low, mid and high respectively) to estimate the cost of ITO coated PET were used. This results in costs of $3.38, $7.77 and $12.52 per m^2 at 2 GW production. In comparison to an earlier report by Mathews et. al., the estimation would have been $10.18 per m^2. [150] At this rate over 12 million m^2 of ITO coated PET is required. The production of Indium (In) was 760 tonnes in 2019 of which the vast majority is used to produce ITO.[151] It is not only difficult to determine the quantity of ITO production, but the quantity used to

produce ITO coated flexible polymer substrates is even more difficult to ascertain. Assuming the amount is on the order of five percent (a generous assumption), then the current production capabilities of ITO coated PET can support about 2 GW. The cost of the ITO coated PET is driven both by the cost of the In and the cost of manufacturing. Using the cost of an ITO sputter target and applying a modest learning rate of 9% would yield a cost of ITO at \$1.34 m^2 for a 4 GW production capacity. The non-materials costs for producing ITO coated glass were estimated to be \$1.64 m^2.[152] This would yield a total cost of \$2.98 per m^2, which is in line with the lower estimate. Using an analysis proposed by Woodhouse, the estimated costs using the current spot price of In results is a cost of \$3.60 per m^2.[153]. The main point is to demonstrate that at the volumes described in this study, the cost floor for ITO coated PET is not outside the realm of possibility. But it is obvious that the most expensive component in the production of the PVSK film is the ITO coated PET. Furthermore, to reach the scales of several hundred GW production capacity will be limited by the availability of Indium unless a cheaper alternative appears.

Equipment Costs The overall equipment costs are approximately 1/3rd of the non-material costs as shown in Figure 3.1.2. The overall costs of the equipment, web length for each piece of equipment required for the roll-to-roll deposition at per 1 GW production is tabulated in Table 3.1.1. It is estimated that the equipment cost per 1 GW production line is \$14M and that the total tool length is about 24 meters. The individual equipment specifications have been designed to meet a 4 GW production using a single line. Since these equipment costs are dwarfed by the materials costs a single line will be used at 25% capacity for this analysis. This serves to improve the robustness of the operations by guaranteeing production rates as equipment fluctuations occur. Using this capacity ratio also allows for some leeway into the design of the manufacturing line, where it may be possible to design a layout in which a line is dedicated to a single layer, requiring 4 lines.

For this analysis the evaporation is accomplished using a convective air knife and annealing is done using IPL. The drying and annealing of solution phase films has historically been accomplished in ovens that dominate the roll-to-roll manufacturing line. The replacement of these ovens with the air knife and IPL processes has the advantage of a much shorter web section, less equipment costs, and an overall shorter footprint. The evaporation by air knives for a single layer has been accomplished in less than 10 seconds and the IPL annealing process can be accomplished in less than 1 second.[85, 154] At a web speed of 10 m/min this would require an overall tool length of about 2 m. Most of the cost is associated with the IPL stations, making up 75% of the equipment costs.

Assuming that the web is 1.5 m wide and allowing for 2 m on either side of the web, the total manufacturing footprint is approximately 108 m^2 and rounding up, four lines would require ~500 m^2 and applying the \$10,000 per m^2 for installation results in a cost of \$5M. The estimate of \$10,000 per m^2 for installation is on the high side but has little impact on the overall COGS. To estimate the storage footprint, it is assumed that one month of inbound and outbound materials will be maintained and required space is estimated at 10,000 m^2. The building, as expected, is dominated by space for storage of materials. Using a cost \$1,000 per m^2, for yields an estimated building cost of \$15 M. A

4 GW production plant would have a total cost of $71M, or about $18M per 1GW production. A 4 GW plant size is an arbitrary choice but was chosen as this is where the COGS curve becomes relatively flat. In comparison the cost of a c-Si solar cell facility is estimated at $120M for 1 GW yielding a significant cost savings using a roll-to-roll manufacturing process. [155]

Table 3.1.1: Equipment requirements for the Roll-to-Roll line per 1 GW production.

Stations	Number required	Cost per item ($M)	Equipment cost ($M)	Web length per station (m)	Total line length (m)
Roll-to-roll (wind/unwind, controls, dancers, alignment, etc.)	1	0.62	0.62	5.0	5.0
Corona discharge	1	0.25	0.25	0.5	0.5
Slot die	4	0.35	1.40	1.0	4.0
Single/multi-array of air knives	4	0.10	0.40	1.0	4.0
IPL	4	3.00	10.5	1.0	4.0
Laser scribe	3	0.10	0.30	0.5	1.5
Lamination	1	0.25	0.25	5.0	5.0
Total	------	------	13.72	------	24.0

Utilities

Table 3.1.2: Comparison of energy usage per layer using IPL vs. Traditional oven

Layer	IPL (kW-hr/m^2)	Oven (kW-hr/m^2)
SnO_2	0.056	0.056
$MAPbI_3$	0.010	0.119
NiO	0.022	0.043
Cu	0.025	0.388
TOTAL	0.113	0.607

The overall utilities costs in this analysis are approximately 10% of the non-materials costs. The IPL annealing represents more than half but is still less than $0.01 per m^2. The energy requirement for the IPL to process the PVSK layer is estimated to be 0.01 kW-hr/m^2. In comparison, at 1 GW, the energy consumption is 0.119 kW-hr/m^2 using a conventional thermal oven. Table 3.1.2 compares the energy consumption of the IPL and traditional ovens for each of the thin film layers. There is clearly an advantage in the energy costs when using the IPL over a traditional oven. The biggest cost savings is from the exhaust requirements for the solvents being used. The exhaust of the solvents is required for both processes, but for the traditional oven, this airflow must be heated and ends up being a relatively significant utilities cost. The layer that does not show much of a separation in utilities is SnO_2 in which the use of water will require a lower air flow rate; however, even in this case it would be expected that some air flow is necessary to keep the exhaust flow from being saturated.

The IPL process also provides significant cost savings (> 80%) associated with the annealing step. This savings along with the shorter web length in the annealing step will also affect the overall OPEX of manufacturing. Long web sections affect the yield through breakage and misalignment, both of which will also increase the labor to deal with the associated downtime.

Subtask 3.2: **Technoeconomic model refinement**

A manuscript of the findings were submitted to a journal, which went through a thorough vetting process. The team also engaged with other stakeholders to check the model. The process was checked against experiment and found to be in spec.

Task 4.0: Optimize the deposition of the CTL on the PVSK

Based on the results of the prior tasks, the team chose to proceed with the deposition of the SnO_2 directly on the perovskite layer. Doping the SnO2 with Yttrium resulted in a PCE of over 18%. This work also included the study of using interfacial layers and laser etching.

Subtask 4.1: Interfacial layers

One issue that nanoparticle CTL inks struggles with is the presence of pinholes. Due to the packing of spheres, there will invariably be intersectional gaps between tightly packed particles. As particle size decreases the packing density increases and intersectional gaps decrease. Addition of fillers or interfacial layers can further reduce these gaps preventing ion migration.[156] One of the primary modes of degradation that has had significant attention is ion migration in the perovskite film. The loss of iodide in the crystal lattice leads to phase segregation in mixed halide devices structural deformation with the development of lead rich regions, formation of PbI_2 and has been tied to device hysteresis. Iodide migration specifically has been tied to application of electric fields and thermal stress. Permeation of iodide through charge transport layers (CTLs) to react with electrode materials can result in the formation of AgI a p-type dopant.[157] Early works by Kato et al. proposed that the perovskite degradation was induced by pinholes in their spiro-OMeTAD coating that provided pathways moisture penetration and for ion migration from the perovskite to the silver back contact. [158] Similar results have been observed by other researchers with attempts to reduce this degradation pathway ranging from ion doping, small molecule additives, and polymer additives. For an interfacial layer to be effective it needs to able coordinate and passivate surface defects, be electronically conductive, and prevent ion migration. A potential compound with tunable coordinating abilities, imidazoles and their salt derivatives, imidazoliums, have recently been explored as additives and interfacial materials compatible with metal oxides and perovskites.

The degradation of PSCs via iodide migration through the CTL from the perovskite absorber to the Ag electrode is evidenced by the formation of AgI on the back contact. To demonstrate this, we performed a series of stress tests on series of half-cell devices consisting of $MAPbI_3$ as the perovskite absorber on a flexible ITO-PET substrate with SnO_2 as the ETL and Ag as the back contact (Figure 4.1.1a). The half-cell devices were exposed to a range of conditions to identify the role of external forces including air heat, and UV exposure (Figure 4.1.1b-d). Samples placed on a hotplate at 80 °C overnight in an inert environment and dark conditions showed no visible signs of degradation. In

contrast, samples left under dark, ambient conditions showed a rapid browning around the silver contacts overnight. These results are indicative of moisture induced degradation propagating from the outer edge of the contacts towards the center. Samples that were exposed to full spectrum light or UV light while heating at 80 °C under inert environment and short circuit conditions showed significant degradation of the Ag contact. Investigation by XRD was unable to detect the formation of AgI but was able to confirm the that no PbI_2 had formed. (Figure 4.1.1e).

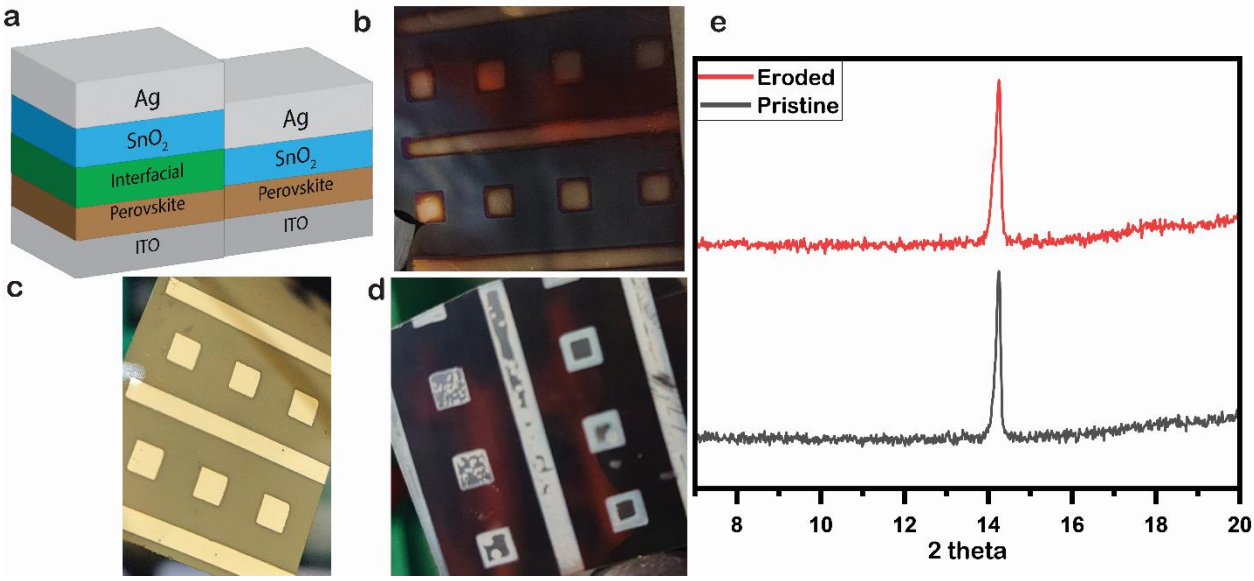

Figure 4.1.1. a) Diagram of half stack with and without interfacial layer, Digital image of perovskite half stack left in b) ambient dark conditions overnight, c) heating at 80 °C, d) heating at 80 °C with UV illumination, e) XRD of film before and after degradation was observed.

A series of imidazoles were then investigated as interfacial layers to evaluate their ability to prevent iodide migration and formation of AgI. The compounds include 1-methylimidazole (Me-IM), 2-methyl-5-nitro imidazole (Me,NO_2-IM), 5-aminoimidazole-4-carboxamide (NH_2,Am-IM), 1-phenylimidazole (Ph-IM), 4-(Imidazol-1-yl)phenol (PhOH-IM), 1-methylbenzimidazole (Me-BIM), and 2-(chloromethyl)-benzimidazole (Cl-BIM), 4,5-diphenylimidazole (diPh-IM), and 1,5-dicyclohexylimidazole (diCy-IM). The compounds were selected to encompass a variety of functional groups that can influence packing interactions and binding modes as described below. The compounds were incorporated as a separate interfacial layer between the perovskite and SnO_2 layers in the half-cells (Figure 4.1.1a), which were exposed to accelerated stress tests of 1 sun illumination under short circuit conditions at an elevated operation temperature of 35°C for 24 hours in a nitrogen glove box.

During the initial stress-test, half-cells with a Me-IM, NH_2,Am-IM, and Me,NO_2-IM interfacial layer suffered from critical failures with significant conversion of the Ag to AgI. Of these, NH_2,Am-IM showed the most degradation of Ag to AgI with complete conversion occurring even prior to any illumination. This is attributed the bidentate coordinating ability of NH_2,Am-IM, which can coordinate to Pb^{2+} and destabilizes the PbI_6 octahedron leading to accelerated iodide migration. The benzimidazole derivatives

Me-BIM and Cl-BIM have fused rings making the molecules rigidly planar. The imidazoles Ph-IM and PhOH-IM have an aromatic functional group on the pyrrole-like nitrogen of the imidazole ring, allowing for free rotation about the C-N bond. The compounds Me-BIM, Ph-IM, and PhOH-IM all successfully passed the stress test with no AgI formation over 24 hours illumination. Interestingly, Cl-BIM did not pass the stress test with formation of AgI taking place even under dark conditions. This can be attributed to weak π-coordination with the Pb^{2+} and π-stacking interactions that orient Me-BIM, Ph-IM, and PhOH-IM into sheets that cover the surface, similar to the π-stacking observed in the x-ray structures of 1-methylbenzimidaziums.[159-161] For Cl-BIM, the Cl sits outside of the BIM plane disrupting p-stacking as observed in the structure of 2-chloromethylbenzimidazolium.[162] Additionally, the phenolic -OH of PhOH-IM may also serve a Lewis base of hydrogen-bonding site for interactions with the perovskite or SnO_2. The electron withdrawing effects of the aromatic ring make this group significantly less basic than the functional groups in NH_2,Am-IM. This is consistent with strong chelating interactions leading to destabilization at the perovskite surface, whereas softer hydrogen bonding or Lewis basic coordination do not.[163] The results above strongly suggest that a molecular planarity and an extended p-interactions are essential for an effective interface layer.

Subtask 4.2: Design of experiments

The synthesis of yttrium doped SnO_2 nanoparticles (Y:SnO_2) was undertaken to improve the electronic properties of SnO_2 nanoparticles, while maintaining low-temperature annealing conditions required for f-PSC fabrication on PET substrates. Functionalization with acetic acid yields Y:SnO_2-A, which enables a stable colloidal dispersion in anhydrous ethanol, which was directly deposited on a PVSK film by blade coating. Several groups have previously demonstrated improved electronic properties and enhanced performance of SnO_2 ETLs upon doping with aliovalent cations such as Y^{3+}, Nb^{5+}, Li^{+}, Mg^{2+}, and Sb^{3+}.[69, 74, 75, 164-166] In the same manner, we shown herein that Y doping improves charge extraction and transport for f-PSC devices prepared on flexible PET substrate with champion PCEs of 14.4% to 18.2% for SnO_2 and Y:SnO_2 devices, respectfully.

A series of yttrium doped tin(IV) oxide (Y:SnO_2) nanoparticles (NPs) were synthesized using a slight modification of the solgel process we recently reported for the synthesis of pristine tin(IV) oxide (SnO_2) particles.[84] For the synthesis Y:SnO_2 nanoparticles, yttrium chloride was added to anhydrous $SnCl_4$ during the synthesis process in the appropriate ratios to get 1, 2, and 3 mol % Y, which are represented as 1% Y:SnO_2, 2% Y:SnO_2, and 3% Y:SnO_2. To enhance dispersibility in PVSK compatible organic solvents, the Y:SnO_2 NPs were functionalized with acetate to yield Y:SnO_2-A using the methods reported for acetate functionalized SnO_2 (SnO_2-A), which is dispersible in anhydrous ethanol.[84, 139] Acetate functionalization converts the amorphous, white powder of Y:SnO_2 to a clear and colorless solution of functionalized tin oxide (Y:SnO_2-A) in glacial acetic acid. Characterization for 2% Y:SnO_2 and 2% Y:SnO_2-A is described below. Data for 1% and 3% doped materials are consistent.

The diluted Y:SnO_2-A ink was deposited directly on the top of the $MAPbI_3$ PVSK layer via blade coating as shown in Figure 4.1b. A dry air knife was used to rapidly remove excess solvent after deposition. Samples were annealed for 2 to 3 minutes at 100˚C on

a hotplate inside a box filled with dry air. The effect of Y:SnO_2-A deposition on the integrity of the PVSK layer was evaluated by scanning electron microscopy (SEM), X-ray diffraction (XRD), and UV-visible spectroscopy. Figures 4.1a-b show top surface SEM images of the PVSK films before and after Y:SnO_2-A deposition. The PVSK film before Y:SnO_2-A deposition (Figure 4.2.1a) shows well-developed perovskite domains without observable pinholes. After Y:SnO_2-A deposition, the structure of the PVSK is partially obscured consistent with a uniform layer of Y:SnO_2-A (Figure 4.1b).

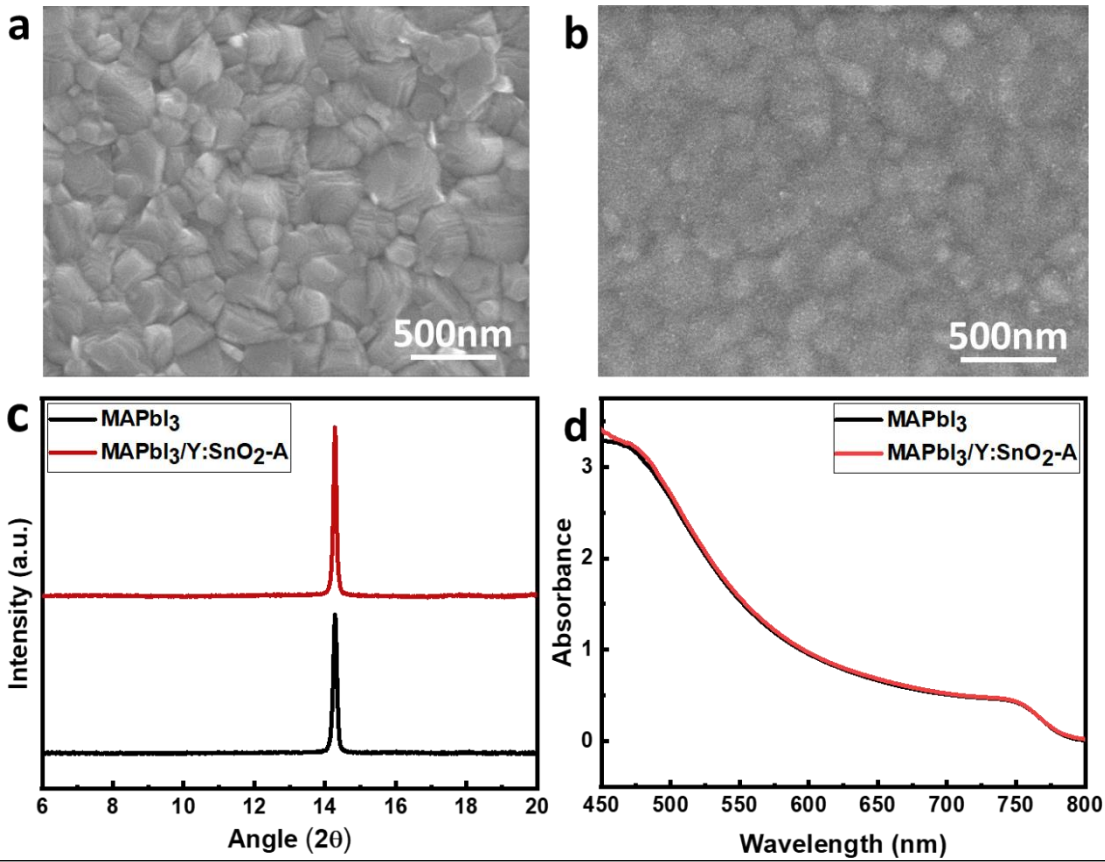

Figure 4.2.1. Characterization of Y:SnO_2 films on PVSK. (a) top-surface SEM micrographs of the PVSK film, (b) Y:SnO_2-A layer on the PVSK film (c) XRD diffraction patterns PVSK before and after Y:SnO_2-A deposition, and (d) UV-Vis spectra of PVSK films before and after Y:SnO_2-A deposition.

The XRD patterns of the PVSK before and after deposition of Y:SnO_2-A (Figure 4.2.1c) further demonstrate the integrity of the PVSK layer is intact following deposition. Prior to deposition, a single prominent peak is observed at 14.1° as expected for $CH_3NH_3PbI_3$. The diffraction pattern is unchanged following the deposition of the Y:SnO_2-A ink on the PVSK surface. If deposition had induced degradation to PbI_2, a peak at 12.7° would be expected. The UV-visible spectra of the PVSK before and after Y:SnO_2-A deposition (Figure 4.2.1d) are also comparable indicating no significant change in optical absorption of the PVSK film and no change in the band edge of the absorption spectra. Overall, the SEM and XRD data confirm that Y:SnO_2-A ethanol inks can be deposited on PVSK without changing PVSK crystallinity and grain size.

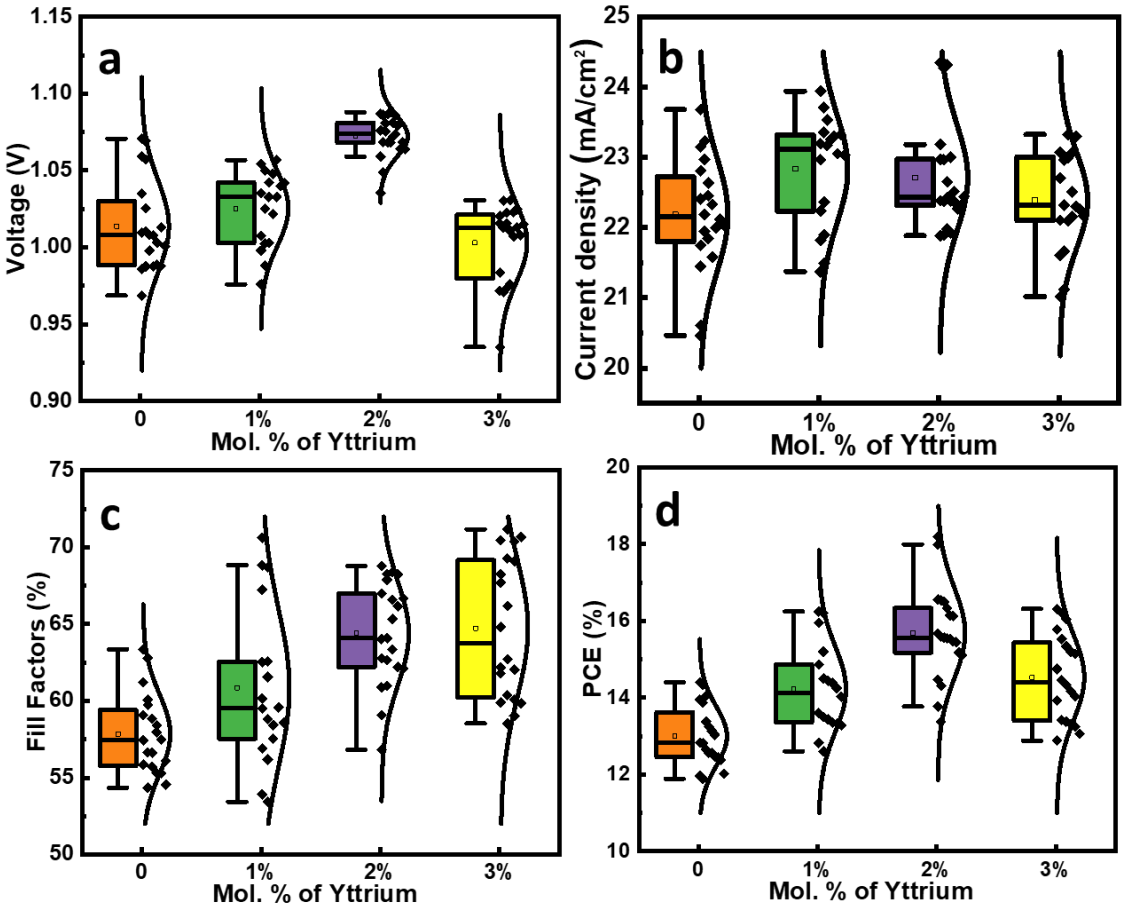

Figure 4.2.2. Device performance statistics as a function of yttrium doping concentration in the Y:SnO2 ETL. The photovoltaic parameters are (a) V_{OC}, (b) J_{SC}, (c) FF, and (d) PCE.

Device performance statistics of the f-PSCs as a function of Y doping concentrations in the Y:SnO_2 ETL yttrium are presented in Figure 4.2.2. The PCEs increased with increasing yttrium concentrations until an optimum performance was achieved with 2 mol. % of yttrium in Y:SnO_2. The increase in PCE is attributed to increases in open-circuit voltage (V_{oc}) and fill factor (FF), and short-circuit current density (J_{sc}) as shown in Table 1. The increase in V_{oc} and J_{sc} indicates an enhancement in conductivity after yttrium doping. We calculated the conductivity of pristine SnO_2 and 2%Y:SnO_2 thin film on the Glass-ITO substrate from the I-V curve using the relation $\sigma = \frac{d}{AR}$ where σ is the conductivity, d is the thickness of SnO_2 and Y:SnO_2 layers (75 nm), A is the area under measurement (0.1cm^2) and R is the resistance calculated from Ohms law i.e., $V = IR$.[70, 71] The conductivity (σ) of the SnO_2 and Y:SnO_2 thin films were calculated to be 13.27 x 10^{-6} Scm^{-1} and 25.95 x 10^{-6} Scm^{-1} respectively. Thus the increase in the electrical conductivity of Y:SnO_2 after Yttrium doping improves the charge extraction. Additionally, yttrium doping decreases series resistance (R_s) and increases shunt

resistance (R_{sh}), which improves the J_{sc}, $V_{oc,}$ and FF parameters.[71, 75] These effects are optimized value in 2% Y:SnO_2 PSCs.

An image of blade-coated f-PSCs is presented in Figure 4.2.3b. It is noteworthy, that the PCE of the champion f-PSC with 2% Y:SnO_2-A is ~4% higher than the PCE of the champion f-PSC with pristine SnO2-A. The device with 2% Y:SnO_2-A exhibited a champion PCE of 18.19 % with a J_{sc} of 24.34 mA/cm^2, a V_{oc} of 1.08 V, and an FF of 68.8% (Figure 4.3c). Figure 4.3d highlights minimal hysteresis between forward and reverse scans of the f-PSCs with 2% Y:SnO_2 as an ETL.

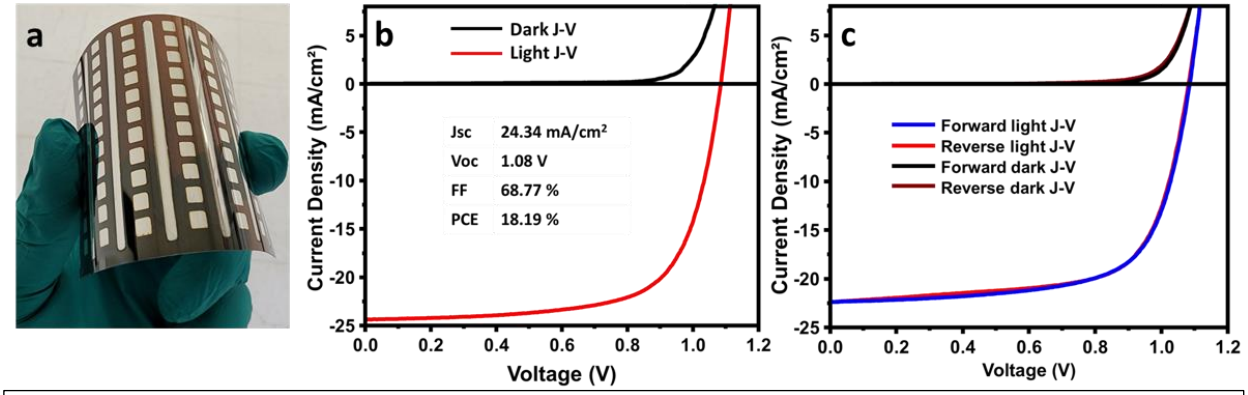

Figure 4.2.3. Device and device characteristics. (a) Digital image of f-PSCs, (b) J−V curve of the champion 0.1 cm^2 Y:SnO_2 device, (c) J−V hysteresis of a Y:SnO_2-A device.

Subtask 4.3: Scribing ETL and HTL

The preparation of the PSC requires the removal of the deposited layers CTL, perovskite and CTL. For much of the work, GBL was used to remove these layers, but is not ideal since the edge of the cell is not well defined with an edge resolution of about 1 mm. Laser scribing is more desirable because it can provide a lower edge resolution and takes less time to complete, expediting the overall manufacturing process. A blue laser is capable of etching through the perovskite layers and by default etch the CTLs due to the heat produced. However, the amount of energy must be controlled in order to not etch through the ITO. An off the shelf hobby blue laser (485 nm, 550 mW) from SainSmart was fitted to a hobby CNC machine from Genmitsu, yielding a setup cost of less than $500. This setup was capable of etching through the PTAA/PVSK/SnO_2 stack but was too powerful and etched through the ITO layer.

A student Capstone team from the Mechanical Engineering Department was assembled to overcome this issue. The decision by the team was to simply increase the traverse speed of the laser while etching to limit the damage to the ITO layer. This required the replacement of the drive mechanism of one of the axis to allow for the higher speed movement (figure 4.3.1A). Once the mechanical and electrical components were

assembled, LaserGRBL software was used to configure the machine's settings to ensure the laser moved at the proper distance and desired speed. A "dynamic laser power mode" was used in the software to automatically adjust the power of the laser based on the current speed of the laser head concerning the build-plate. This setting, along with the high speeds in the X-axis, solved the issue of high laser residence times. With the laser configured properly, etching trials were then performed on actual Perovskite cells (figure 4.3.1 B). Transmission line measurement tests (TLM) were used to find the resistance of the individually etched bus bars. The goal was to achieve resistance as close as possible to the control value for the bare TCO layer. An ideal scenario would yield a bus bar etch with the same resistance as the TCO layer. The average ITO resistance by TLM was 69.53 ohms. At an etching speed of at 18 m/min speed and 30% power resulted in an average busbar resistance by TLM of 94.46 ohms. The percentage difference from the control was 35%, resulting in a roughly 9% decrease in efficiency of the solar cell (for every 10% decrease in resistance, 2.5% is lost in efficiency).

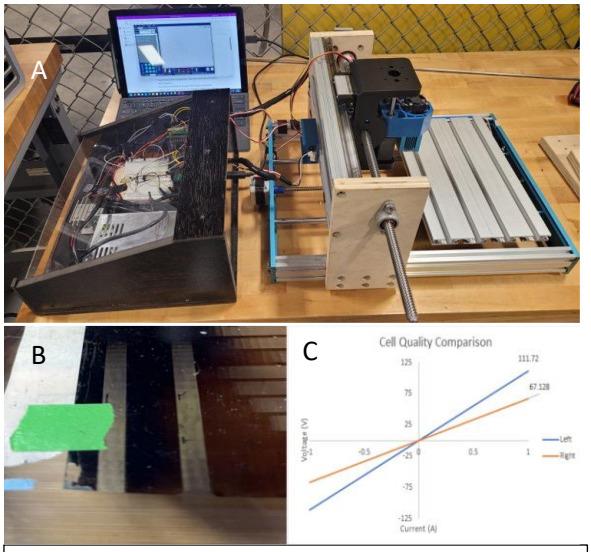

Figure 4.3.1. A) Image of laser scribe setup, B) laser scribed busbars exposing the ITO layer and C) conductivity of ITO and laser scribed busbar.

Task 5: Stakeholder Engagement

Due to COVID, Stakeholder engagement was virtual. The primary discussions center on the assumptions made for the technoeconomic analysis and material/equipment concerns that need to be addressed to insure that the cost targets can be met.

Mid Project Milestones

GNG1-T2.1 Cell efficiency

2 m/min (ETL/ PVSK /HTL) 1 cm^2 cell >16% +/- 3%	Average, standard deviation. I-V measurement of at least 15 cells samples randomly selected from a 1 m length web across and along the length of the web. Additionally, 3 cells will be selected from a second web run after a start/stop	Measured by NREL's Device Performance Group. Data and report sent to DOE for verification	The test result was chosen to demonstrate that control of the deposition of the CTL directly onto the PVSK meets market needs.

Status: The project team built several device architectures using SnO_2 and NiO materials. The web speed of the coating processes were near 2 m/min. The I-V measurements of baseline devices made using the roll-to-roll setup have demonstrated an efficiency of > 10% on a 1 cm^2 device. Considering just the SnO_2 layer roll-to-roll printed, the efficiency of a 1 cm^2 device has exceeded 12%. All three materials

deposited have been successfully thermally processed using IPL, drastically reducing the overall footprint.

Issues: The team is using a relatively high resistive ITO coated PET (50 W/•) mainly to reduce costs. Changing the aspect ratio of the cell would increase the FF due to the decreased series resistance. The team also encountered an issue with the durability of the ITO coating, which seems to delaminate from the PET relatively easily. High humidity in Louisville, KY does impact the deposition of consistent PVSK coatings. This high humidity has been impacting the measurement of the cells, where degradation of the PVSK in contact with the silver can be rapid.

Strategy: The project team investigated several materials and device designs. The team down selected to a single device architecture PET/ITO/NiO/ PVSK /SnO_2 based on the promising results during BP1. The team has demonstrated the doping of the SnO_2 material with yttrium. The University has signed a materials transfer agreement to trial the SnO_2 material in industrial devices. Effort on the NiO was refocused to develop a Cu doped material that can be deposited as the initial layer.

GNG-T2.2 Stability

1,000 hours < 10% η loss (relative)	Efficiency ratio. Test 5 encapsulated cells (sealed in inert gas glass-glass capsule) under constant illumination with unregulated humidity. (Humidity to be monitored and recorded.)	Measured at NREL and/or UofL. Data and report sent to DOE for verification	Generally accepted as a first pass durability test for PSC.

Status: The team has tested the stability of devices not under load during the extended stays at NREL. These results have demonstrated an initial device stability. The team has designed and built equipment that will allow them to test devices using the ISOS-L1 protocols.

Issues: The team had limited access to an inert environment for testing cells under constant illumination. A setup was built that allowed the team to test cells in a controlled environment under illumination.

Strategy: The team has built equipment that allows for the evaluation of devices under constant light soaking.

GNG Cv2.1 Technoeconomic

Feedback: from at least 4 stakeholders with a minimum of 3 representing industry	Written feedback with verification that techno-economic model fits technical targets and market expectations, Covering at a minimum materials and equipment costs, throughput, yield, life and efficiency. Stakeholders will include material and equipment suppliers and module manufacturers. Final roll-up will be cost per Watt for the module manufacturer.	Report sent to the DOE detailing the validation of the technoeconomic analysis based on stakeholder feedback.	Buy in from industry stakeholders of the technoeconomic analysis is critical to commercialization.

Status: A complete techno-economic model that considers the materials, processes and equipment has been developed. This model has been published in Applied Energy.[10]

Issues: None

Strategy: The team will continue to engage with external stakeholders to understand the economics of employing this technology.

GNG-CV2.2 Processability

Successful scribing of CTL	I-V curve of the layer demonstrating that the electrical conductivity of the CTL is broken.	Measured at UofL. Data and report sent to DOE for verification.	The successful commercialization into a module may require that one or more of the CTLs can be scribed.

Status: The team has demonstrated that a 420 nm laser can etch through the metal oxide layers.

Issues: The team has not yet demonstrated the equipment in a full device.

Strategy: The team was unable to make a full device, but confirmed the electrical conductivity of the ITO layer and the layers above were visibly missing.

GNG-SH2.1 Stakeholder Engagement

Virtual meetings organized with relevant stakeholders	Count. At least 5 virtual meetings held with stakeholders.	Meeting minutes to be sent to DOE.	Discussion amongst stakeholders across the technology will be important to the commercialization.

Status: Five manuscripts have been published. The team has presented four papers, several virtually. Three patents related to the IPL process have been issued and one provisional patent has been submitted related to the deposition of metal oxides onto PVSKs. The team has held 3 online meetings with stakeholders and have sent the details to the DOE. Beyond this the team has continued to engage with several stakeholders including equipment manufacturers (Xenon, Novacentrix) and PSC manufacturers (EMC). The University has signed a materials transfer agreement to sample SnO_2 for evaluation in their process.

Issues: The COVID-19 pandemic severely limited the ability for the team to attend meetings.

Strategy: The team will continue to submit manuscripts.

Task 6: Full cell integration

Previously, we reported a fully solution processable SnO_2 as an electron transport material in a p-i-n PSC with 14.1% PCE, which was unprecedented for solution-phase SnO_2.[84] Our newest work recently published achieved a PCE of 16.55%, where the addition of Yttrium doping improved both the V_{oc} and FF. During this reporting period we investigate 1) the IPL process as implemented for both the mixed cation perovskite and Y:SnO_2-A layers and 2) the stability of the Y:SnO_2-A materials in sub-task 6-2.

Subtask 6.1: Full stack production

The statistical data for a (a) hotplate processed multi-cation PVSK (MC) as well as (b) an IPL processed MC and (c) IPL processed MC/ Y:SnO_2-A layer is shown in figure 6.1.1 and were obtained from 14 and 20 devices, respectively. Hotplate-annealed PSCs had slightly higher V_{oc} and J_{sc} but observed lower fill factors than IPL-annealed PSCs. Champion device of 16.68% PCE for IPL-annealed samples are shown in figure 6.1a. IPL-annealed PSCs had a tighter distribution across the sample set, suggesting that the technique is more reproducible.

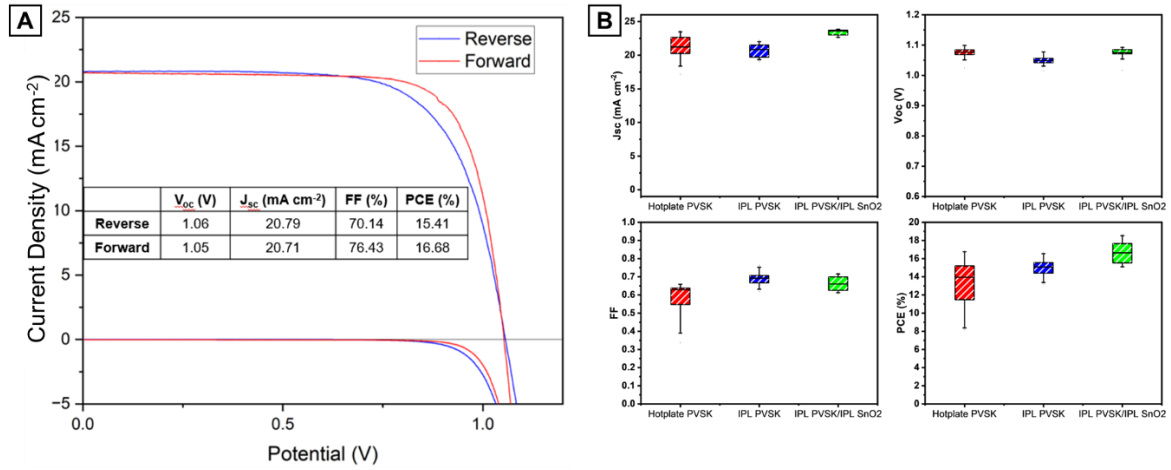

	V_{oc} (V)	J_{sc} (mA cm^{-2})	FF (%)	PCE (%)
Reverse	1.06	20.79	70.14	15.41
Forward	1.05	20.71	76.43	16.68

Figure 6.1.1 (a) JV performance data of the champion IPL-annealed PSC using the optimized ink formulation, light and dark currents. Optimized ink formulation: $FA_{0.4}MA_{0.6}PbI_{0.95}Br_{0.05}$ in 0.6 ACN:0.4 2-ME (v:v) with 6% NMP (mol%), 3 mg/mL PEAI, 38 µL/mL CH_2I_2. (b) Comparison of the performance data of PSCs with Hotplate-annealed PVSK layer, IPL-annealed PVSK layer, and IPL-annealed PVSK and SnO_2 layers. IPL-annealed samples match hotplate-annealed samples and are processed in <30 seconds. The IPL parameters used for IPL-annealed samples were 1700V, 500 µsec duration, 500 msec delay, 3 pulses

To identify whether the hotplate annealing of SnO_2 was affecting the PVSK layer, PSCs in which the SnO_2 was processed using IPL were fabricated. The IPL parameters were identical for PVSK and SnO_2 layers and no optimization of IPL parameters for the SnO_2 layer was done. The champion device PCE was higher for the IPL-annealed SnO_2 sample; however, hysteresis was observed which would indicate a non-optimized process.

A combination of optimized IPL annealing conditions and the CH_2I_2 additive resulted in IPL-annealed devices that were as/more efficient than hotplate-annealed devices, previously unachievable as shown in figure 6.1.1. The drastic increase in processing speed causes a significant reduction in unit manufacturing costs, making this solvent system enticing for high-throughput, low-cost roll-to-roll manufacturing. The technoeconomic analysis by Martin et. al. showed that the capital expenditures for IPL would be 30% less, for the same throughput, and operating expenses would be 80% less that traditional ovens.[10]

In a final demonstration of the full project the following films of NiO, PVSK and SnO_2 were deposited and post-processed using the IPL. This is the first ever reported flexible PSC that utilized metal oxides as both the ETL and HTL. The average performance of these devices is ~12%. Future work should be able to improve the device perofomance.

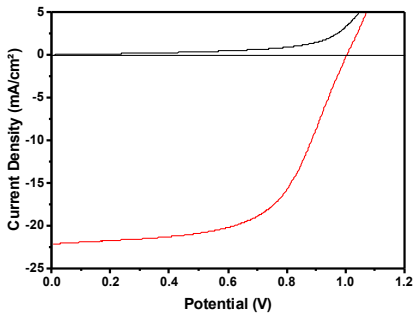

0.1 cm^2	V_{OC} (V)	J_{SC} (mA/cm^2)	FF (%)	η (%)
Champion	1.0	22.09	59.0	13.25
Average	0.99	21.18	57.0	12.05
Std dev	0.040	0.48	3.16	0.91

Material	Process	Anneal
SnO_2	Blade	IPL
$FAMAPbI_3$	Blade	IPL
NiO_x	Blade	IPL
ITO PET (50 ohm/sq)		

Steps to Date

- Optimized IPL annealing for all layers
- MA has higher IPL tolerance to $MAPbI_3$

Next steps.

- Demonstration of stability
- Introduction of Interfacials

Figure 6.1.2: Flexible PSC using NiO, PVSK, SnO2 deposited and IPL post-processed.

Subtask 6.2: End of project cell durability

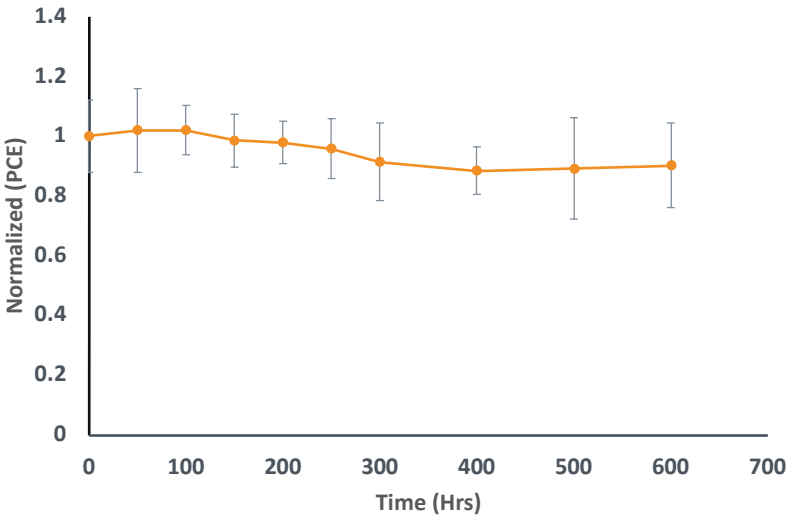

Figure 6.2.1: Durability of PSC.

A stability setup was designed inside a nitrogen-filled box to evaluate the operational stability of the fabricated triple cation f-PSCs under continuous illumination. An array of

LED lamps was selected as the light source, and the light intensity was set to one0.8 to 1 sun using aan NREL-certified calibrated reference photodiode. The temperature of the stability measurement system was measured to be 35±5˚ C. A total of 20 pixels were a part of this test. For this study, we used triple cation perovskite with a device configuration of PET-ITO/PTAA/TC/SnO2/BCP/Ag. The power conversion efficiency of the devices was initially measured every 48 hours for up to 300 hours and then every 100 hours for up to 600 hours. The device performance statistics of the stability test are shown in the following figure. After 600 hours, 90% of the average initial efficiency was retained for the f-PSCs on the ITO-PET substrate.

While working with $MAPbI_3$ devices it was found that iodide migration through the SnO_2 layer was driven by UV light. The addition of an interfacial barrier such as polymethyl methacrylate between the SnO_2 layer and Ag was able to successfully prevent the formation of AgI during a 30 hour stress tests while devices without the coating degraded during initial JV testing. The stress test was conducted in an N_2 glove box, under constent illumination, at short circuit, with temperature varying between 35-40 °C. Other materials that were successful at preventing AgI formation were found to have planer packing orientation with the best preforming materials also having coordinated functional groups to assist in anchoring to the SnO_2 layer.

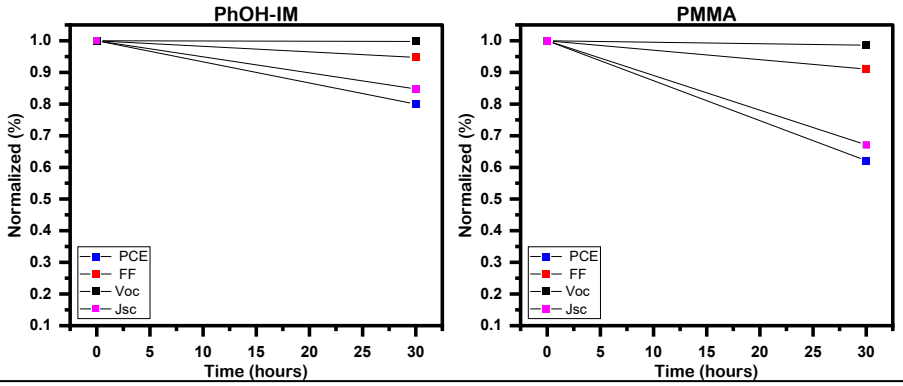

Figure 6.2.2: Stability of $MAPbI_3$ devices with passivator between SnO_2 and Ag

Task 7: Stakeholder commitments

The work during this reporting period has included transfer of materials developed at the University to two industry partners and two academic partners for evaluation. 100 mL of the SnO_2 chemistry was sent for evaluation. The initial results of that work were encouraging with device functionality similar to the results established at the University.

Based on the results from the field testing of the metal oxides and the lessons learned on the PSCs, the students on the team are applied to the Perovskite Startup Challenge. The team, SoFab Inks, were awarded $200k for their startup idea and are actively scaling up the SnO_2 materials. Dr. Druffel is an advisor to SoFab Inks. The team has also been invited to submit an iCorps proposal to the NSF for the summer cohort.

End of Project Milestones

EOP-T3.1 Cell Efficiency

2 m/min (ETL/PVSK/HTL/Metal) 1 cm^2 cell 18% +/- 2%	Average, standard deviation. I-V measurement of at least 15 cells samples randomly selected from a 1 m length web across and along the length of the web. Additionally, 3 cells will be selected from a second web run after a start/stop	Measured by NREL's Device Performance Group. Data and report sent to DOE for verification	Success value was chosen as this target represents a high average efficiency with a small deviation that will be important for commercialization.

Status: The team has demonstrated over 18% efficiency where the SnO2 and PVSK layers are processed by IPL.

Issues: The main issue encountered is the swing in humidity that occurs in Louisville, KY. During low humidity season, very high efficiency devices are prepared.

Strategy: The University of Louisville is building a new facility to be operational in 2025. This should have better control of humidity and temperature. In addition, all facilities for the solar manufacturing will be co-located.

EOP-T3.2 Cell Stability

1000 hrs < 10% loss (relative)	Efficiency ratio. Test 5 unencapsulated cells under constant illumination with unregulated humidity. (Humidity to be monitored and recorded.)	Measured at NREL and/or UofL. Data and report sent to DOE for verification	Generally accepted as a first pass durability test for PSC

Status: After 600 hours, 90% of the average initial efficiency was retained for the f-PSCs on the ITO-PET substrate. This is short of the proposed metric as explained below. To achieve 600 hours it was necessary to utilize a TC PVSK thin film as this formulation has been shown to have the highest durability.

Issues: The main two issues faced with the durability test were intrinsic to the materials we were using and extrinsic to the test platform. The SnO_2 layer is a nanoparticle layer that unavoidably will include voids. These voids allow the halide (I) to migrate across into the Ag contact, causing degradation. The extrinsic issues are related to the test setup, where in the end we were forced to keep the samples in humidity controlled glove box in order to avoid the massive humidity swings that occur in Louisville, KY.

Strategy: The interface between the SnO_2 and perovskite is very good as evidenced by the high V_{oc}, so we have chosen to add an interface layer between the SnO_2 and Ag. The obvious choice, which has been as a capping layer, is a polymer such as polymethyl methacrylate. This has been promising in some initial runs. We plan to put this into an extended test soon.

EOP-CV 3.1 Letter of Intent

Count. A minimum of 2 letters of intent from relevant stakeholders committing to supply materials and/or equipment at the costs outlined in the technoeconomic model.	Letters delivered to DOE	Success of the award will be measured by private entities willing to sell materials/equipment at competitive costs.

Status: Verbal acknowledgement of the costing models have been obtained; however, these have not been sent to the DOE.

Issues: Lack of commitment from suppliers to publish data.

Strategy: Continue to work with potential suppliers.

EOP-SH3.1 Memorandum of Understanding

Count. At least one memorandum of understanding to pursue funding to commercialize the technology.	Agreement sent to DOE	Success of the award will be measured by successful technology transfer to private entities.

Status: SoFab Inks was established in 2022 to commercialize the inks described in this proposal. To date they have secured $250k in funding to move forward with the technology development and commercialization. SoFab inks was founded by 3 graduate students working on this project.

Issues: None

Strategy: Continue to work with SoFab inks.

EOP-SH3.2 Dissemination

Manuscript	Count. At least 2 manuscripts submitted for publication and one provisional patent application.	Accepted manuscript uploaded into OSTI (SEE FARC for more info about reporting requirements)	Dissemination of results through publications offers opportunities to alert the further community of the success of the project. Pate

Status: Total 9 published manuscripts.

Issues: None

Strategy: 3 more manuscripts are being prepared.

EOP-SH3.3 Process Transferability

Industry Engagement with at least 2 partners	Count. Demonstrate the IPL process using materials and/or architecture supplied by third party industry partner. The minimum cell efficiency tested provided by the industry partner >20% and the IPL/IR process will not decrease the efficiency by more than 10%.	Letter attesting to the improvement in operation sent to the DOE.	Success of the award is to establish that the process can be ported to other materials and architectures.

Status: The project team is actively engage with one industry partner. Material and process has been demonstrated.

Issues: The IPL process is a relatively new process and is not being used as anticipated since most manufacturers are more familiar with oven drying.

Strategy: Will continue to work with industry partners as well as the startup that was created during this work. Another proposal has been submitted related to the accomplishments reported here with another industry partner.

9. Significant Accomplishments and Conclusions:

As described in the sections above, the team is working with several materials and deposition techniques, and these are summarized in figure 9.1. Based on the work from the team has down selected a device architecture that is a PET/ITO/NiO/mulit-cation PVSK /SnO_2/Metal. Parameters for the ink formulation, deposition and IPL processing have been established for each of the layers. Efficiencies of greater than 18% have been achieved.

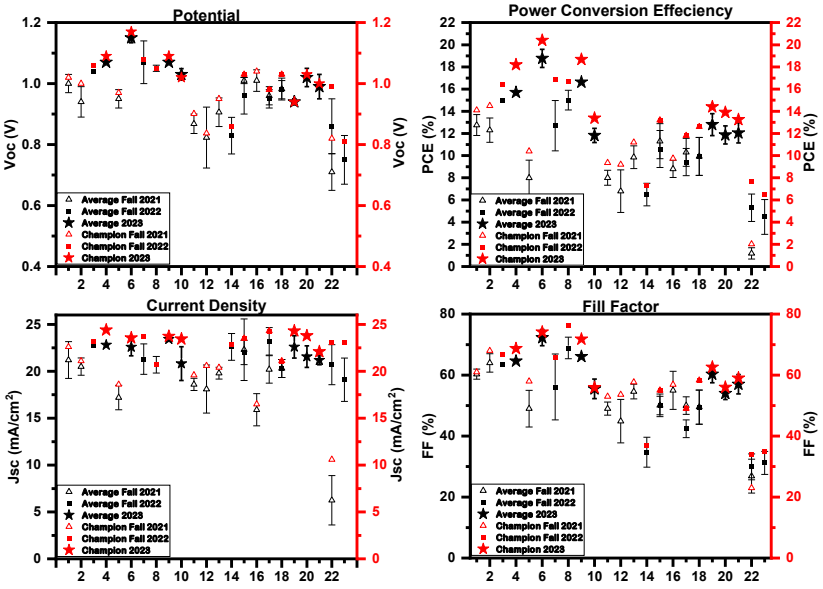

Sample	Architecture	Area
1	SnO2 Blade (Glass)	0.25
2	SnO2 Blade	0.25
3	SnO2 Blade	0.1
4	Y:SnO2 Blade	0.1
5	TC/ SnO2 by Blade	0.25
6	TC/Y:SnO2 Blade	0.1
7	MC/SnO2 Blade	0.25
8	MC-IPL/Y:SnO2	0.1
9	MC/Y:SnO2-IPL	0.1
10	TC/Y:SnO2	1.0
11	R2R NiOx- Plasma	0.25
12	R2R NiO/ R2R MAPbI	0.25
13	R2R Cu:NiO/ MAPbI	0.25
14	R2R Cu:NiO/ R2R MAPbI	1
15	R2R SnO2/Blade MAPbI	1
16	R2R SnO2/Blade MAPbI NMP	1
17	R2R SnO2/R2R MAPbI	1
18	Full MO_x by Blade	0.25
19	NiO_x/IL/MAPbI/SnO_2 by Blade	0.1
20	Full MO_x IL in NiO_x	0.1
21	Full MO_x IPL annealed	0.1
22	R2R Full MO_x	0.25
23	R2R Full MO_x – Mixed Cation	0.25

Figure 9.1: Summary of device results to date.

The three most significant accomplishments are:

1. Successfully demonstrating a device utilizing a PVSK sandwiched between two inorganic CTLs that was deposited by ink chemistries and processed by IPL.
2. Successfully demonstrating that a metal oxide ink can be deposited directly onto a PVSK thin film and demonstrating this with multiple PVSK formulations. Champion device is shown in figure 9.2.
3. Spin out of University technology by students who were involved in the research.

Challenges

The three most significant challenges were:

1. COVID, the pandemic severely impacted the opportunity to collaborate with NREL and industry partners and amongst our own university group. The pandemic also limited the number of undergraduate students we could include in the research. Roll-to-roll coating trials proved to be difficult to sustain due to

limitations in chemistry and personnel, since we were not able to include undergraduate students in the work. As a work around we relied heavily on blade coating techniques.

2. Demonstrating durability was a rather large challenge, both from testing for durability and engineering a fix. In the end we were able to develop a testing chamber that yielded consistent results and engineering fixes to improve the durability of the devices.
3. Swings in ambient conditions that made working with the materials in the summer rather challenging. Towards the end of the project, we had developed a multi-cation PVSK chemistry that had a more robust processing window.

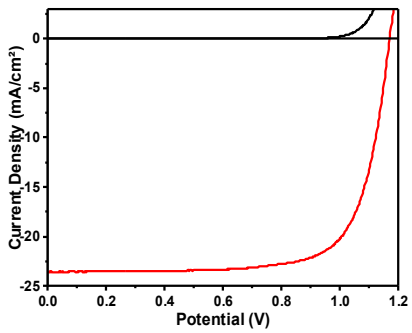

0.1 cm²	V_{oc} (V)	J_{sc} (mA/cm²)	FF (%)	η (%)
Champion	1.17	23.6	74.1	20.4
Average	1.15	22.6	72.3	18.8
Std dev	0.019	0.59	4.42	1.32

Material	Process	Anneal
Y:SnO_2	Blade	Plate
TC	Blade	Plate
PTAA	Blade	Plate
ITO PET (15 ohm/sq)		

Steps to date

- Perovskite ink stability increased
- Fast evaporation

Next Steps

- Large area cells
- Slot die coating
- SnO_2/Ag interface

Figure 9.2: Champion device from project.

10. Path Forward:

A company was formed by the graduate students who were working on this project to commercialize the SnO_2 ink chemistries.

The IPL process will take a bit more work to convince manufacturers to adopt, although we have worked with a few of the industry partners to demonstrate. For the roll-to-roll space the experience with ovens is long and these manufacturers may be adverse to taking on the risk of an unproven technology. Although the IPL has been demonstrated for the UV curing industry (DVDs, headlamps and etc) in continuous operation, theer has not been widespread adoption in traditional roll-to-roll.

The University will continue to research the use of the imidazolium as interfacial layers and engineered chemistries to allow for the deposition of NiO on a perovskite. We are also testing polymers as a capping layer for the SnO_2.

11. Products:

Peer reviewed publications

1. Martin, B., M. Yang, R.C. Bramante, E. Amerling, G. Gupta, M.F.A.M. van Hest, and T. Druffel, *Fabrication of flexible perovskite solar cells via rapid thermal annealing.* Materials Letters, 2020. **276** 10.1016/j.matlet.2020.128215
2. Armstrong, P.J., P.S. Chandrasekhar, S. Chapagain, C.M. Cline, M. van Hest, T. Druffel, and C.A. Grapperhaus, *Solvation of NiOxfor hole transport layer deposition in perovskite solar cells.* Nanotechnology, 2021. **33**(6) 10.1088/1361-6528/ac328e
3. Chapagain, S., P.S. Chandrasekhar, D. McGott, R.C. Bramante, M.F.A.M. van Hest, M.O. Reese, T. Druffel, and C.A. Grapperhaus, *Direct Deposition of Nonaqueous SnO2 Dispersion by Blade Coating on Perovskites for the Scalable Fabrication of p-i-n Perovskite Solar Cells.* Acs Applied Energy Materials, 2021. **4**(10): p. 10477-10483 10.1021/acsaem.1c01287
4. Ghahremani, A.H., S. Pishgar, J. Bahadur, and T. Druffel, *Intense Pulse Light Annealing of Perovskite Photovoltaics Using Gradient Flashes.* ACS Applied Energy Materials, 2020. **3**(12): p. 11641-11654 10.1021/acsaem.0c01520
5. Chandrasekhar, P.S., S. Chapagain, B. Martin, P.J. Armstrong, C. Grapperhaus, and T.L. Druffel, *Rapid scalable fabrication of roll-to-roll slot-die coated flexible perovskite solar cells using intense pulse light annealing.* Sustainable Energy & Fuels, 2022. **6**: p. 5316-5323 10.1039/d2se00911k
6. Martin, B., D. Amos, E. Brehob, M.F.A.M. van Hest, and T. Druffel, *Techno-economic analysis of roll-to-roll production of perovskite modules using radiation thermal processes.* Applied Energy, 2022. **307** 10.1016/j.apenergy.2021.118200
7. Chapagain, S., B. Martin, P. Armstrong, C.L. Perkins, M.O. Reese, T. Druffel, and C.A. Grapperhaus, *High Performing Inverted Flexible Perovskite Solar Cells via Solution Phase Deposition of Yttrium-Doped SnO2 Directly on Perovskite.* Acs Applied Energy Materials, 2023. **6**(9): p. 4496-4502 10.1021/acsaem.2c03720
8. Martin, B., S. Chapagain, P. Armstrong, C.A. Grapperhaus, M.O. Reese, and T. Druffel, *IPL-Annealed Mixed-Cation Perovskites with Robust Coating Window toward Scalable Manufacturing of Commercial Perovskite Solar Cells.* Acs Applied Energy Materials, 2023, 2023. **6**(10): p. 5207-5216 10.1021/acsaem.3c00134
9. Armstrong, P.J., S. Chapagain, R. Panta, C. Grapperhaus, and T. Druffel, *Synthesizing and formulating metal oxide nanoparticle inks for perovskite solar cells.* Chem Commun (Camb), 2023 10.1039/d3cc02830e

Conference Presentations

1. Druffel T. (2022). Progress Towards the Scalable Production of Perovskite Solar Cells Using a High Throughput Roll-to-Roll Platform, at ECS 242nd Meeting, Atlanta, GA
2. Armstrong, P. (2022). Roll-to-roll manufacture of perovskite devices, at ISCST, Minneapolis, MN, 14 Sep 2022.

3. Druffel T. (2022). High Volume Production of Nanoscale Elements, at NNCI Summit, Louisville, KY 9 Aug 2022.
4. Druffel, T. (2022). Scaling Perovskite Manufacturing, presentation to NREL perovskite working group, (virtually) 1 July 2022
5. Druffel, T. (2021). Roll-to-roll production of perovskite solar cells AIMCAL, Orlando, FL. (virtually).
6. Chandrasekhar, P. S., & Druffel, T. (2021). Integration of Intense Pulse Light annealing for Rapid Scale fabrication of Roll-to-Roll Slot-die coated Perovskite Solar Cells, at ECS 240th Meeting, (virtually).
7. Druffel, T. (2020) “Rapid Annealing of Perovskite Solar Cells”, at ECS 238th Meeting, Honolulu, HI (virtually)
8. Martin, B., M. Yang, R. C. Bramante, E. Amerling, G. Gupta, M. F. A. M. van Hest and T. Druffel (2020). “Fabrication of flexible perovskite solar cells via rapid thermal annealing” presented at IEEE PVSC (virtually)
9. Armstrong, P., A. Ghahremani, T. Druffel, R. Buchanan, and C. Grapperhaus (2019) “Hole Transporting Layers in Solar Cells: Stabilizing NiO Perovskite Inks with Organic Capping Agents” at ECS 236th Meeting, Atlanta, GA
10. Martin, B., A. H. Ghahremani, and T. Druffel “Scalable Hole Transport Materials for Roll-to-Roll Perovskite Photovoltaic Modules” at ECS 236th Meeting, Atlanta, GA

Students

Blake Martin, PhD (2023) – Chemical Engineering

Peter Armstrong – PhD Candidate - Chemistry

Sashil Chapagain – PhD Condidate - Chemistry

Rojita Panta – PhD Candidate - Chemistry

Patent Applications

Druffel, T., C. Grapperhaus, S. Chapagain, P. Armstrong, B. Martin, and M.F.A.M.v. Hest. (2022) Methods for preparing perovskite solar cells (PSCS) and the resulting PSCS, PCT/US2022/076697

12. Project Team and Roles:

Thad Druffel, PhD, PE – PI served as PhD mentor of Dr. Blake Martin. He managed the overall project and had contributions to materials synthesis, ink formulation, device production and device characterization. Contributions included design of experiments, data interpretation, external partnerships and budget. Dr. Druffel was also involved in the preparation, submission and revision of all manuscripts as well as the preparation and prosecution of the patent application.

Craig Grapperhaus, PhD – coPI served as the Ph.D. mentor of Armstrong, Chapagain, and Panta. He oversaw activity on Task 1, Subtask 2.1, and Task 4 related to the synthesis and functionalization of metal oxide nanoparticles for deposition of the CTL on the perovskite. Contributions included the design of experiments, data interpretation, and troubleshooting. Prof. Grapperhaus also contributed to the preparation and revision of manuscripts and serves as corresponding authors on three publications.

Delaina Amos, PhD – coPI Assisted with the ink formulation for the roll-to-roll deposition of materials. Prof. Amos also contributed to the preparation and revision of the technoeconomic analysis manuscript.

Mikail van Hest, PhD – coPI Assisted with the coordination of work at NREL preformed by the students. Dr. van Hest also contributed to the preparation and revision of 4 manuscripts and is a named inventor on the patent application.

Matthew Reese, PhD – coPI Assisted with the coordination of work at NREL performed by the students. Dr. Reese also contribute to the preparation and revision of 2 manuscripts.

Siva Chandrasekar, PhD - post doctoral researcher Was primarily responsible for translation of ink development to the roll-to-roll coating apparatus (task 2).

Blake Martin, PhD – Graduate student working on the development of the MC PVSK inks related to tasks 2.2, 3, 5, 6 and 7.

Peter Armstrong – Graduate student working on the development of NiO_x CTL material related to Task 1 and Subtask 2.1

Sashil Chapagain – Graduate student working on the development of SnO_2 ETL material related to task 1 and 2, 4, and 6.

Rojita Panta – Graduate student working on the durability of NiO/perovskite interface related to task 6.

13. References:

1. Kojima, A., K. Teshima, Y. Shirai, and T. Miyasaka, *Organometal halide perovskites as visible-light sensitizers for photovoltaic cells.* J Am Chem Soc, 2009. **131**(17): p. 6050-1 10.1021/ja809598r
2. Laboratory, N.R.E. *Best Research-Cell Efficiency Chart*. 2023 [cited 2023 8-8-23]; Available from: https://www.nrel.gov/pv/cell-efficiency.html.
3. Christians, J.A., P. Schulz, J.S. Tinkham, T.H. Schloemer, S.P. Harvey, B.J. Tremolet de Villers, A. Sellinger, J.J. Berry, and J.M. Luther, *Tailored interfaces of unencapsulated perovskite solar cells for >1,000 hour operational stability.* Nature Energy, 2018. **3**(1): p. 68-74 10.1038/s41560-017-0067-y
4. Berry, J.J., J. van de Lagemaat, M.M. Al-Jassim, S. Kurtz, Y. Yan, and K. Zhu, *Perovskite Photovoltaics: The Path to a Printable Terawatt-Scale Technology.* ACS Energy Letters, 2017. **2**(11): p. 2540-2544 10.1021/acsenergylett.7b00964
5. Lightfoot, E.J. and E.D. Cohen, *Coating and Solidification*, in *Roll-to-roll Manufacturing*, J. Greener, G. Pearson, and M. Calkmak, Editors. 2018, John Wiley & Sons, Inc.: Hoboken, NJ. p. 19-64.
6. Drozd, E. and J.M. Drozd. (2008) Waveguide exposure chamber for heating and drying material, U.S.P. Office, 7.470,876
7. Lavery, B.W., S. Kumari, H. Konermann, G.L. Draper, J. Spurgeon, and T. Druffel, *Intense Pulsed Light Sintering of CH3NH3PbI3 Solar Cells.* ACS Applied Materials & Interfaces, 2016. **8**(13): p. 8419-8426 10.1021/acsami.5b10166
8. Ankireddy, K., A.H. Ghahremani, B. Martin, G. Gupta, and T. Druffel, *Rapid thermal annealing of CH3NH3PbI3 perovskite thin films by intense pulsed light with aid of diiodomethane additive.* Journal of Materials Chemistry A, 2018. **6**(20): p. 9378-9383 10.1039/c8ta01237g
9. Green, M.A., E.D. Dunlop, G. Siefer, M. Yoshita, N. Kopidakis, K. Bothe, and X. Hao, *Solar cell efficiency tables (Version 61).* Progress in Photovoltaics: Research and Applications, 2022. **31**(1): p. 3-16 10.1002/pip.3646
10. Martin, B., D. Amos, E. Brehob, M.F.A.M. van Hest, and T. Druffel, *Techno-economic analysis of roll-to-roll production of perovskite modules using radiation thermal processes.* Applied Energy, 2022. **307** 10.1016/j.apenergy.2021.118200
11. Xu, Z., Q. Zhuang, Y. Zhou, S. Lu, X. Wang, W. Cai, and Z. Zang, *Functional Layers of Inverted Flexible Perovskite Solar Cells and Effective Technologies for Device Commercialization.* Small Structures, 2023. **n/a**(n/a): p. 2200338 https://doi.org/10.1002/sstr.202200338
12. Wu, Z., W. Li, Y. Ye, X. Li, and H. Lin, *Recent progress in meniscus coating for large-area perovskite solar cells and solar modules.* Sustainable Energy & Fuels, 2021. **5**(7): p. 1926-1951 10.1039/D0SE01774D
13. Li, Z., T.R. Klein, D.H. Kim, M. Yang, J.J. Berry, M.F.A.M. van Hest, and K. Zhu, *Scalable fabrication of perovskite solar cells.* Nature Reviews Materials, 2018. **3**(4): p. 18017 10.1038/natrevmats.2018.17

14. Yang, J., E.L. Lim, L. Tan, and Z. Wei, *Ink Engineering in Blade-Coating Large-Area Perovskite Solar Cells.* Advanced Energy Materials, 2022. **12**(28): p. 2200975 https://doi.org/10.1002/aenm.202200975
15. Chapagain, S., B. Martin, P. Armstrong, C.L. Perkins, M.O. Reese, T. Druffel, and C.A. Grapperhaus, *High Performing Inverted Flexible Perovskite Solar Cells via Solution Phase Deposition of Yttrium-Doped SnO2 Directly on Perovskite.* ACS Applied Energy Materials, 2023. **6**(9): p. 4496-4502 10.1021/acsaem.2c03720
16. Zuo, C., D. Vak, D. Angmo, L. Ding, and M.J.N.E. Gao, *One-step roll-to-roll air processed high efficiency perovskite solar cells.* 2018. **46**: p. 185-192
17. Dou, B., J.B. Whitaker, K. Bruening, D.T. Moore, L.M. Wheeler, J. Ryter, N.J. Breslin, J.J. Berry, S.M. Garner, F.S. Barnes, S.E. Shaheen, C.J. Tassone, K. Zhu, and M.F.A.M. van Hest, *Roll-to-Roll Printing of Perovskite Solar Cells.* ACS Energy Letters, 2018. **3**(10): p. 2558-2565 10.1021/acsenergylett.8b01556
18. Abbas, M., L. Zeng, F. Guo, M. Rauf, X.-C. Yuan, and B. Cai, *A Critical Review on Crystal Growth Techniques for Scalable Deposition of Photovoltaic Perovskite Thin Films.* Materials, 2020. **13**: p. 1-42 10.3390/ma13214851
19. Deng, Y., C.H. Van Brackle, X. Dai, J. Zhao, B. Chen, and J. Huang, *Tailoring solvent coordination for high-speed, room-temperature blading of perovskite photovoltaic films.* Sci Adv, 2019. **5**(12): p. eaax7537 10.1126/sciadv.aax7537
20. Niu, G., X. Guo, and L. Wang, *Review of recent progress in chemical stability of perovskite solar cells.* Journal of Materials Chemistry A, 2015. **3**(17): p. 8970-8980 10.1039/C4TA04994B
21. Docampo, P., J.M. Ball, M. Darwich, G.E. Eperon, and H.J.J.N.c. Snaith, *Efficient organometal trihalide perovskite planar-heterojunction solar cells on flexible polymer substrates.* 2013. **4**(1): p. 1-6
22. Dualeh, A., N. Tétreault, T. Moehl, P. Gao, M.K. Nazeeruddin, and M. Grätzel, *Effect of Annealing Temperature on Film Morphology of Organic–Inorganic Hybrid Pervoskite Solid-State Solar Cells.* Advanced Functional Materials, 2014. **24**(21): p. 3250-3258 10.1002/adfm.201304022
23. Cho, A.-N. and N.-G. Park, *Impact of Interfacial Layers in Perovskite Solar Cells.* 2017. **10**(19): p. 3687-3704 https://doi.org/10.1002/cssc.201701095
24. Cao, X., L. Zhi, Y. Jia, Y. Li, K. Zhao, X. Cui, L. Ci, D. Zhuang, and J. Wei, *A Review of the Role of Solvents in Formation of High-Quality Solution-Processed Perovskite Films.* ACS Applied Materials & Interfaces, 2019. **11**(8): p. 7639-7654 10.1021/acsami.8b16315
25. Siegler, T.D., A. Dawson, P. Lobaccaro, D. Ung, M.E. Beck, G. Nilsen, and L.L. Tinker, *The Path to Perovskite Commercialization: A Perspective from the United States Solar Energy Technologies Office.* ACS Energy Letters, 2022. **7**(5): p. 1728-1734 10.1021/acsenergylett.2c00698
26. Pellet, N., P. Gao, G. Gregori, T.Y. Yang, M.K. Nazeeruddin, J. Maier, and M.J.A.c. Grätzel, *Mixed-organic-cation Perovskite photovoltaics for enhanced solar-light harvesting.* 2014. **126**(12): p. 3215-3221
27. Saliba, M., T. Matsui, J.-Y. Seo, K. Domanski, J.-P. Correa-Baena, M.K. Nazeeruddin, S.M. Zakeeruddin, W. Tress, A. Abate, A. Hagfeldt, and M. Grätzel, *Cesium-containing triple*

cation perovskite solar cells: improved stability, reproducibility and high efficiency. Energy & Environmental Science, 2016. **9**(6): p. 1989-1997 10.1039/C5EE03874J

28. Byranvand, M.M., C. Otero-Martínez, J. Ye, W. Zuo, L. Manna, M. Saliba, R.L.Z. Hoye, and L. Polavarapu, *Recent Progress in Mixed A-Site Cation Halide Perovskite Thin-Films and Nanocrystals for Solar Cells and Light-Emitting Diodes.* 2022. **10**(14): p. 2200423 https://doi.org/10.1002/adom.202200423
29. Binek, A., F.C. Hanusch, P. Docampo, and T. Bein, *Stabilization of the Trigonal High-Temperature Phase of Formamidinium Lead Iodide.* The Journal of Physical Chemistry Letters, 2015. **6**(7): p. 1249-1253 10.1021/acs.jpclett.5b00380
30. Conings, B., J. Drijkoningen, N. Gauquelin, A. Babayigit, J. D'Haen, L. D'Olieslaeger, A. Ethirajan, J. Verbeeck, J. Manca, and E.J.A.E.M. Mosconi, *Intrinsic thermal instability of methylammonium lead trihalide perovskite.* 2015. **5**(15): p. 1500477
31. Ghosh, D., A.R. Smith, A.B. Walker, and M.S. Islam, *Mixed A-Cation Perovskites for Solar Cells: Atomic-Scale Insights Into Structural Distortion, Hydrogen Bonding, and Electronic Properties.* Chemistry of Materials, 2018. **30**(15): p. 5194-5204 10.1021/acs.chemmater.8b01851
32. Doherty, T.A.S., S. Nagane, D.J. Kubicki, Y.-K. Jung, D.N. Johnstone, A.N. Iqbal, D. Guo, K. Frohna, M. Danaie, E.M. Tennyson, S. Macpherson, A. Abfalterer, M. Anaya, Y.-H. Chiang, P. Crout, F.S. Ruggeri, S. Collins, C.P. Grey, A. Walsh, P.A. Midgley, and S.D. Stranks, *Stabilized tilted-octahedra halide perovskites inhibit local formation of performance-limiting phases.* 2021. **374**(6575): p. 1598-1605 doi:10.1126/science.abl4890
33. Mozur, E.M. and J.R. Neilson, *Cation Dynamics in Hybrid Halide Perovskites.* 2021. **51**(1): p. 269-291 10.1146/annurev-matsci-080819-012808
34. Chen, C., Z. Song, C. Xiao, R.A. Awni, C. Yao, N. Shrestha, C. Li, S.S. Bista, Y. Zhang, L. Chen, R.J. Ellingson, C.-S. Jiang, M. Al-Jassim, G. Fang, and Y. Yan, *Arylammonium-Assisted Reduction of the Open-Circuit Voltage Deficit in Wide-Bandgap Perovskite Solar Cells: The Role of Suppressed Ion Migration.* ACS Energy Letters, 2020. **5**(8): p. 2560-2568 10.1021/acsenergylett.0c01350
35. Pavlovetc, I.M., M.C. Brennan, S. Draguta, A. Ruth, T. Moot, J.A. Christians, K. Aleshire, S.P. Harvey, S. Toso, S.U. Nanayakkara, J. Messinger, J.M. Luther, and M. Kuno, *Suppressing Cation Migration in Triple-Cation Lead Halide Perovskites.* ACS Energy Letters, 2020. **5**(9): p. 2802-2810 10.1021/acsenergylett.0c01207
36. Cao, J., S.X. Tao, P.A. Bobbert, C.P. Wong, and N.J.A.M. Zhao, *Interstitial occupancy by extrinsic alkali cations in perovskites and its impact on ion migration.* 2018. **30**(26): p. 1707350
37. Abdi-Jalebi, M., Z. Andaji-Garmaroudi, S. Cacovich, C. Stavrakas, B. Philippe, J.M. Richter, M. Alsari, E.P. Booker, E.M. Hutter, and A.J.J.N. Pearson, *Maximizing and stabilizing luminescence from halide perovskites with potassium passivation.* 2018. **555**(7697): p. 497-501
38. Schelhas, L.T., Z. Li, J.A. Christians, A. Goyal, P. Kairys, S.P. Harvey, D.H. Kim, K.H. Stone, J.M. Luther, K.J.E. Zhu, and E. Science, *Insights into operational stability and processing of halide perovskite active layers.* 2019. **12**(4): p. 1341-1348

39. Li, N., Y. Luo, Z. Chen, X. Niu, X. Zhang, J. Lu, R. Kumar, J. Jiang, H. Liu, and X.J.J. Guo, *Microscopic degradation in formamidinium-cesium lead iodide perovskite solar cells under operational stressors.* 2020. **4**(8): p. 1743-1758
40. Saidaminov, M.I., K. Williams, M. Wei, A. Johnston, R. Quintero-Bermudez, M. Vafaie, J.M. Pina, A.H. Proppe, Y. Hou, and G.J.N.m. Walters, *Multi-cation perovskites prevent carrier reflection from grain surfaces.* 2020. **19**(4): p. 412-418
41. Liu, L., J. Lu, H. Wang, Z. Cui, G. Giorgi, Y. Bai, and Q. Chen, *A-site phase segregation in mixed cation perovskite.* Materials Reports: Energy, 2021. **1**(4): p. 100064 https://doi.org/10.1016/j.matre.2021.100064
42. Liu, S., Y. Guan, Y. Sheng, Y. Hu, Y. Rong, A. Mei, and H. Han, *A Review on Additives for Halide Perovskite Solar Cells.* Advanced Energy Materials, 2020. **10**(13) 10.1002/aenm.201902492
43. Ghahremani, A.H., B. Martin, A. Gupta, J. Bahadur, K. Ankireddy, and T. Druffel, *Rapid fabrication of perovskite solar cells through intense pulse light annealing of SnO2 and triple cation perovskite thin films.* Materials & Design, 2020. **185**: p. 108237 https://doi.org/10.1016/j.matdes.2019.108237
44. Xu, W., R.T. Piper, Y. Zheng, A.V. Malko, and J.W.P. Hsu, *Elucidating Diiodomethane-Induced Improvement in Photonically Cured MAPbI3 Solar Cells.* ACS Applied Energy Materials, 2022. **5**(6): p. 7328-7334 10.1021/acsaem.2c00848
45. Japan's, N.J.B.-F.P., *Panasonic Achieve the World's Highest Conversion Efficiency of 16.09% for Largest-area Perovskite Solar Cell Module.* 2020
46. Heo, J.H., F. Zhang, C. Xiao, S.J. Heo, J.K. Park, J.J. Berry, K. Zhu, and S.H.J.J. Im, *Efficient and stable graded CsPbI3− xBrx perovskite solar cells and submodules by orthogonal processable spray coating.* 2021. **5**(2): p. 481-494
47. Bu, T., J. Li, H. Li, C. Tian, J. Su, G. Tong, L.K. Ono, C. Wang, Z. Lin, and N.J.S. Chai, *Lead halide–templated crystallization of methylamine-free perovskite for efficient photovoltaic modules.* 2021. **372**(6548): p. 1327-1332
48. Deng, Y., X. Zheng, Y. Bai, Q. Wang, J. Zhao, and J.J.N.E. Huang, *Surfactant-controlled ink drying enables high-speed deposition of perovskite films for efficient photovoltaic modules.* 2018. **3**(7): p. 560-566
49. Chen, S., X. Dai, S. Xu, H. Jiao, L. Zhao, and J.J.S. Huang, *Stabilizing perovskite-substrate interfaces for high-performance perovskite modules.* 2021. **373**(6557): p. 902-907
50. Yaghoobi Nia, N., F. Giordano, M. Zendehdel, L. Cinà, A.L. Palma, P.G. Medaglia, S.M. Zakeeruddin, M. Grätzel, and A. Di Carlo, *Solution-based heteroepitaxial growth of stable mixed cation/anion hybrid perovskite thin film under ambient condition via a scalable crystal engineering approach.* Nano Energy, 2020. **69**: p. 104441 https://doi.org/10.1016/j.nanoen.2019.104441
51. Heo, J.H., M.H. Lee, M.H. Jang, and S.H.J.J.o.M.C.A. Im, *Highly efficient CH 3 NH 3 PbI 3− x Cl x mixed halide perovskite solar cells prepared by re-dissolution and crystal grain growth via spray coating.* 2016. **4**(45): p. 17636-17642
52. Bi, E., W. Tang, H. Chen, Y. Wang, J. Barbaud, T. Wu, W. Kong, P. Tu, H. Zhu, X. Zeng, J. He, S.-i. Kan, X. Yang, M. Grätzel, and L. Han, *Efficient Perovskite Solar Cell Modules with High Stability Enabled by Iodide Diffusion Barriers.* Joule, 2019. **3**(11): p. 2748-2760 https://doi.org/10.1016/j.joule.2019.07.030

53. Yang, M., Z. Li, M.O. Reese, O.G. Reid, D.H. Kim, S. Siol, T.R. Klein, Y. Yan, J.J. Berry, M.F.A.M. van Hest, and K. Zhu, *Perovskite ink with wide processing window for scalable high-efficiency solar cells.* Nature Energy, 2017. **2**(5): p. 17038 10.1038/nenergy.2017.38
54. Mahmood, K., S. Sarwar, and M.T. Mehran, *Current status of electron transport layers in perovskite solar cells: materials and properties.* RSC Advances, 2017. **7**(28): p. 17044-17062 10.1039/C7RA00002B
55. Zhou, Y., X. Li, and H. Lin, *To be higher and stronger—metal oxide electron transport materials for perovskite solar cells.* Small, 2020. **16**(15): p. 1902579
56. Lin, L., T.W. Jones, T.C.J. Yang, N.W. Duffy, J. Li, L. Zhao, B. Chi, X. Wang, and G.J. Wilson, *Inorganic electron transport materials in perovskite solar cells.* Advanced Functional Materials, 2021. **31**(5): p. 2008300
57. Ball, J.M., M.M. Lee, A. Hey, and H.J. Snaith, *Low-temperature processed meso-superstructured to thin-film perovskite solar cells.* Energy & Environmental Science, 2013. **6**(6): p. 1739-1743
58. Liu, M., M.B. Johnston, and H.J. Snaith, *Efficient planar heterojunction perovskite solar cells by vapour deposition.* Nature, 2013. **501**(7467): p. 395-398
59. Min, H., D.Y. Lee, J. Kim, G. Kim, K.S. Lee, J. Kim, M.J. Paik, Y.K. Kim, K.S. Kim, and M.G. Kim, *Perovskite solar cells with atomically coherent interlayers on SnO2 electrodes.* Nature, 2021. **598**(7881): p. 444-450
60. Xiong, L., Y. Guo, J. Wen, H. Liu, G. Yang, P. Qin, and G. Fang, *Review on the application of SnO2 in perovskite solar cells.* Advanced Functional Materials, 2018. **28**(35): p. 1802757
61. Park, S.Y., M.Y. Baek, Y. Ju, D.H. Kim, C.S. Moon, J.H. Noh, and H.S. Jung, *Simultaneous ligand exchange fabrication of flexible perovskite solar cells using newly synthesized uniform tin oxide quantum dots.* The Journal of Physical Chemistry Letters, 2018. **9**(18): p. 5460-5467
62. Xie, H., X. Yin, P. Chen, J. Liu, C. Yang, W. Que, and G. Wang, *Solvothermal synthesis of highly crystalline SnO2 nanoparticles for flexible perovskite solar cells application.* Materials Letters, 2019. **234**: p. 311-314
63. Song, J., E. Zheng, J. Bian, X.-F. Wang, W. Tian, Y. Sanehira, and T. Miyasaka, *Low-temperature SnO 2-based electron selective contact for efficient and stable perovskite solar cells.* Journal of Materials Chemistry A, 2015. **3**(20): p. 10837-10844
64. Jiang, Q., L. Zhang, H. Wang, X. Yang, J. Meng, H. Liu, Z. Yin, J. Wu, X. Zhang, and J. You, *Enhanced electron extraction using SnO2 for high-efficiency planar-structure HC (NH2) 2PbI3-based perovskite solar cells.* Nature Energy, 2016. **2**(1): p. 1-7
65. Jiang, Q., Z. Chu, P. Wang, X. Yang, H. Liu, Y. Wang, Z. Yin, J. Wu, X. Zhang, and J. You, *Planar-structure perovskite solar cells with efficiency beyond 21%.* Advanced materials, 2017. **29**(46): p. 1703852
66. Yang, G., C. Chen, F. Yao, Z. Chen, Q. Zhang, X. Zheng, J. Ma, H. Lei, P. Qin, and L. Xiong, *Effective carrier-concentration tuning of SnO2 quantum dot electron-selective layers for high-performance planar perovskite solar cells.* Advanced Materials, 2018. **30**(14): p. 1706023

67. Bose, A.C., D. Kalpana, P. Thangadurai, and S. Ramasamy, *Synthesis and characterization of nanocrystalline SnO2 and fabrication of lithium cell using nano-SnO2.* Journal of Power Sources, 2002. **107**(1): p. 138-141
68. Noh, Y.W., J.H. Lee, I.S. Jin, S.H. Park, and J.W. Jung, *Tailored electronic properties of Zr-doped SnO2 nanoparticles for efficient planar perovskite solar cells with marginal hysteresis.* Nano Energy, 2019. **65**: p. 104014
69. Park, M., J.-Y. Kim, H.J. Son, C.-H. Lee, S.S. Jang, and M.J. Ko, *Low-temperature solution-processed Li-doped SnO2 as an effective electron transporting layer for high-performance flexible and wearable perovskite solar cells.* Nano Energy, 2016. **26**: p. 208-215
70. Ye, H., Z. Liu, X. Liu, B. Sun, X. Tan, Y. Tu, T. Shi, Z. Tang, and G. Liao, *17.78% efficient low-temperature carbon-based planar perovskite solar cells using Zn-doped SnO2 electron transport layer.* Applied Surface Science, 2019. **478**: p. 417-425
71. Ren, X., D. Yang, Z. Yang, J. Feng, X. Zhu, J. Niu, Y. Liu, W. Zhao, and S.F. Liu, *Solution-processed Nb: SnO2 electron transport layer for efficient planar perovskite solar cells.* ACS applied materials & interfaces, 2017. **9**(3): p. 2421-2429
72. Chen, B.-X., H.-S. Rao, W.-G. Li, Y.-F. Xu, H.-Y. Chen, D.-B. Kuang, and C.-Y. Su, *Achieving high-performance planar perovskite solar cell with Nb-doped TiO 2 compact layer by enhanced electron injection and efficient charge extraction.* Journal of Materials Chemistry A, 2016. **4**(15): p. 5647-5653
73. Lv, Y., B. Cai, Q. Ma, Z. Wang, J.J. Liu, and W.-H. Zhang, *Highly crystalline Nb-doped TiO 2 nanospindles as superior electron transporting materials for high-performance planar structured perovskite solar cells.* RSC advances, 2018. **8**(37): p. 20982-20989
74. Bai, Y., Y. Fang, Y. Deng, Q. Wang, J. Zhao, X. Zheng, Y. Zhang, and J. Huang, *Low temperature solution-processed Sb: SnO2 nanocrystals for efficient planar perovskite solar cells.* ChemSusChem, 2016. **9**(18): p. 2686-2691
75. Yang, G., H. Lei, H. Tao, X. Zheng, J. Ma, Q. Liu, W. Ke, Z. Chen, L. Xiong, and P. Qin, *Reducing hysteresis and enhancing performance of perovskite solar cells using low-temperature processed Y-doped SnO2 nanosheets as electron selective layers.* Small, 2017. **13**(2): p. 1601769
76. Degani, M., Q. An, M. Albaladejo-Siguan, Y.J. Hofstetter, C. Cho, F. Paulus, G. Grancini, and Y. Vaynzof, *23.7% Efficient inverted perovskite solar cells by dual interfacial modification.* Science advances, 2021. **7**(49): p. eabj7930
77. Yoo, J.J., G. Seo, M.R. Chua, T.G. Park, Y. Lu, F. Rotermund, Y.-K. Kim, C.S. Moon, N.J. Jeon, and J.-P. Correa-Baena, *Efficient perovskite solar cells via improved carrier management.* Nature, 2021. **590**(7847): p. 587-593
78. Kim, M., J. Jeong, H. Lu, T.K. Lee, F.T. Eickemeyer, Y. Liu, I.W. Choi, S.J. Choi, Y. Jo, and H.-B. Kim, *Conformal quantum dot–SnO2 layers as electron transporters for efficient perovskite solar cells.* Science, 2022. **375**(6578): p. 302-306
79. Siegrist, S., P. Nandi, R.K. Kothandaraman, A. Abdessalem, A.N. Tiwari, and F. Fu, *Understanding Coating Thickness and Uniformity of Blade-Coated SnO*

2

Electron Transport Layer for Scalable Perovskite Solar Cells. Solar RRL, 2023 10.1002/solr.202300273

80. Jiang, Q., Y. Zhao, X. Zhang, X. Yang, Y. Chen, Z. Chu, Q. Ye, X. Li, Z. Yin, and J. You, *Surface passivation of perovskite film for efficient solar cells.* Nature Photonics, 2019. **13**(7): p. 460-466 10.1038/s41566-019-0398-2
81. Chandrasekhar, P.S., S. Chapagain, M. Blake, P.J. Armstrong, C. Grapperhaus, and T.L. Druffel, *Rapid scalable fabrication of roll-to-roll slot-die coated flexible perovskite solar cells using intense pulse light annealing.* Sustainable Energy & Fuels, 2022. **6**(23): p. 5316-5323 10.1039/D2SE00911K
82. Wang, Y., L. Yang, C. Dall'Agnese, G. Chen, A.-J. Li, and X.-F. Wang, *Spray-coated SnO 2 electron transport layer with high uniformity for planar perovskite solar cells.* Frontiers of Chemical Science and Engineering, 2021. **15**: p. 180-186
83. You, J., L. Meng, T.-B. Song, T.-F. Guo, Y. Yang, W.-H. Chang, Z. Hong, H. Chen, H. Zhou, and Q. Chen, *Improved air stability of perovskite solar cells via solution-processed metal oxide transport layers.* Nature nanotechnology, 2016. **11**(1): p. 75-81
84. Chapagain, S., P.S. Chandrasekhar, D. McGott, R.C. Bramante, M.F. van Hest, M.O. Reese, T. Druffel, and C.A. Grapperhaus, *Direct deposition of nonaqueous SnO2 dispersion by blade coating on perovskites for the scalable fabrication of p–i–n perovskite solar cells.* ACS Applied Energy Materials, 2021. **4**(10): p. 10477-10483
85. Martin, B., S. Chapagain, P. Armstrong, C.A. Grapperhaus, M.O. Reese, and T. Druffel, *IPL-Annealed Mixed-Cation Perovskites with Robust Coating Window toward Scalable Manufacturing of Commercial Perovskite Solar Cells.* ACS Applied Energy Materials, 2023. **6**(10): p. 5207-5216 10.1021/acsaem.3c00134
86. Tsiba Matondo, J., D. Malouangou Maurice, Q. Chen, L. Bai, and M. Guli, *Inorganic copper-based hole transport materials for perovskite photovoltaics: Challenges in normally structured cells, advances in photovoltaic performance and device stability.* Solar Energy Materials and Solar Cells, 2021. **224**: p. 111011 https://doi.org/10.1016/j.solmat.2021.111011
87. Bouich, A., J.C. Torres, H. Chfii, J. Marí-Guaita, Y.H. Khattak, F. Baig, B.M. Soucase, and P. Palacios, *Delafossite as hole transport layer a new pathway for efficient perovskite-based solar sells: Insight from experimental, DFT and numerical analysis.* Solar Energy, 2023. **250**: p. 18-32 https://doi.org/10.1016/j.solener.2022.12.022
88. Li, M., X. Xu, Y. Xie, H.-W. Li, Y. Ma, Y. Cheng, and S.-W. Tsang, *Improving the conductivity of sol–gel derived NiOx with a mixed oxide composite to realize over 80% fill factor in inverted planar perovskite solar cells.* Journal of Materials Chemistry A, 2019. **7**(16): p. 9578-9586 10.1039/C8TA10821H
89. Zhao, L., X. Sun, Q. Yao, S. Huang, L. Zhu, J. Song, Y. Zhao, and Y. Qiang, *Field-Effect Control in Hole Transport Layer Composed of Li:NiO/NiO for Highly Efficient Inverted Planar Perovskite Solar Cells.* Advanced Materials Interfaces, 2022. **9**(2): p. 2101562 https://doi.org/10.1002/admi.202101562
90. Zhang, X., L. Shen, P. Baral, S.N. Vijayaraghavan, F. Yan, X. Gong, and H. Wang, *Blade-coated inverted perovskite solar cells in an ambient environment.* Solar Energy Materials and Solar Cells, 2022. **246**: p. 111894 https://doi.org/10.1016/j.solmat.2022.111894

91. Li, C., Y. Zhang, X. Zhang, P. Zhang, X. Yang, and H. Chen, *Efficient Inverted Perovskite Solar Cells with a Fill Factor Over 86% via Surface Modification of the Nickel Oxide Hole Contact.* Advanced Functional Materials, 2023. **33**(13): p. 2214774 https://doi.org/10.1002/adfm.202214774
92. Piper, R.T., T.B. Daunis, W. Xu, K.A. Schroder, and J.W.P. Hsu, *Photonic Curing of Nickel Oxide Transport Layer and Perovskite Active Layer for Flexible Perovskite Solar Cells: A Path Towards High-Throughput Manufacturing.* Frontiers in Energy Research, 2021. **9**(76) 10.3389/fenrg.2021.640960
93. Jiang, F., W.C.H. Choy, X. Li, D. Zhang, and J. Cheng, *Post-treatment-Free Solution-Processed Non-stoichiometric NiOx Nanoparticles for Efficient Hole-Transport Layers of Organic Optoelectronic Devices.* Advanced Materials, 2015. **27**(18): p. 2930-2937 https://doi.org/10.1002/adma.201405391
94. Bai, S., P. Da, C. Li, Z. Wang, Z. Yuan, F. Fu, M. Kawecki, X. Liu, N. Sakai, J.T.-W. Wang, S. Huettner, S. Buecheler, M. Fahlman, F. Gao, and H.J. Snaith, *Planar perovskite solar cells with long-term stability using ionic liquid additives.* Nature, 2019. **571**(7764): p. 245-250 10.1038/s41586-019-1357-2
95. Cui, X., J. Jin, J. Zou, Q. Tang, Y. Ai, X. Zhang, Z. Wang, Y. Zhou, Z. Zhu, G. Tang, Q. Cao, S. Liu, X. Liu, and Q. Tai, *NiOx Nanocrystals with Tunable Size and Energy Levels for Efficient and UV Stable Perovskite Solar Cells.* Advanced Functional Materials, 2022. **32**(31): p. 2203049 https://doi.org/10.1002/adfm.202203049
96. Ouyang, D., J. Zheng, Z. Huang, L. Zhu, and W.C.H. Choy, *An efficacious multifunction codoping strategy on a room-temperature solution-processed hole transport layer for realizing high-performance perovskite solar cells.* Journal of Materials Chemistry A, 2021. **9**(1): p. 371-379 10.1039/D0TA05873D
97. Guo, T., Z. Zhang, L. Yu, H. Yuan, J. Zhang, X. Liu, Z. Hu, and Y. Zhu, *Synthesis of well dispersed NiO ink for efficient perovskite solar cells.* Journal of Alloys and Compounds, 2021. **860** 10.1016/j.jallcom.2020.157889
98. Pirzad Ghias Abadi, S., M. Borhani Zarandi, and N. Jahanbakhshi Zadeh, *Synthesis methods of NiOx nanoparticles and its effect on hole conductivity and stability of n-i-p perovskite solar cells.* Synthetic Metals, 2022. **289** 10.1016/j.synthmet.2022.117115
99. Zhang, H., C. Zhao, J. Yao, and W.C.H. Choy, *Dopant-free NiOx Nanocrystals: A Low-cost and Stable Hole Transport Material for Commercializing Perovskite Optoelectronics.* Angewandte Chemie International Edition, 2023. **n/a**(n/a): p. e202219307 https://doi.org/10.1002/anie.202219307
100. Ciro, J., D. Ramírez, M.A. Mejía Escobar, J.F. Montoya, S. Mesa, R. Betancur, and F. Jaramillo, *Self-Functionalization Behind a Solution-Processed NiOx Film Used As Hole Transporting Layer for Efficient Perovskite Solar Cells.* ACS Applied Materials & Interfaces, 2017. **9**(14): p. 12348-12354 10.1021/acsami.6b15975
101. Bahari Molla Mahaleh, Y., S.K. Sadrnezhaad, and D. Hosseini, *NiO Nanoparticles Synthesis by Chemical Precipitation and Effect of Applied Surfactant on Distribution of Particle Size.* Journal of Nanomaterials, 2008. **2008**: p. 470595 10.1155/2008/470595
102. Shin, S.S., S.J. Lee, and S.I. Seok, *Metal Oxide Charge Transport Layers for Efficient and Stable Perovskite Solar Cells.* Advanced Functional Materials, 2019. **29**(47): p. 1900455 https://doi.org/10.1002/adfm.201900455

103. Wang, Q., Z. Lin, J. Su, Z. Hu, J. Chang, and Y. Hao, *Recent progress of inorganic hole transport materials for efficient and stable perovskite solar cells.* Nano Select, 2021. **2**(6): p. 1055-1080 https://doi.org/10.1002/nano.202000238
104. Chen, W., Y. Wu, J. Fan, A.B. Djurišić, F. Liu, H.W. Tam, A. Ng, C. Surya, W.K. Chan, D. Wang, and Z.-B. He, *Understanding the Doping Effect on NiO: Toward High-Performance Inverted Perovskite Solar Cells.* Advanced Energy Materials, 2018. **8**(19): p. 1703519 https://doi.org/10.1002/aenm.201703519
105. Di Girolamo, D., F. Di Giacomo, F. Matteocci, A.G. Marrani, D. Dini, and A. Abate, *Progress, highlights and perspectives on NiO in perovskite photovoltaics.* Chemical Science, 2020. **11**(30): p. 7746-7759 10.1039/D0SC02859B
106. Marand, Z.R., A. Kermanpur, F. Karimzadeh, E.M. Barea, E. Hassanabadi, E.H. Anaraki, B. Julián-López, S. Masi, and I. Mora-Seró, *Structural and Electrical Investigation of Cobalt-Doped NiO(x)/Perovskite Interface for Efficient Inverted Solar Cells.* Nanomaterials, 2020. **10**(5): p. 872 10.3390/nano10050872
107. Kotta, A., I. Seo, H.-S. Shin, and H.-K. Seo, *Room-temperature processed hole-transport layer in flexible inverted perovskite solar cell module.* Chemical Engineering Journal, 2022. **435**: p. 134805 https://doi.org/10.1016/j.cej.2022.134805
108. Xu, X., H. Zhang, Y. Tong, Y. Sun, X. Fang, J. Xu, and X. Wang, *Tuning Ni3+ quantity of NiO via doping of cations with varied valence states: The key role of Ni3+ on the reactivity.* Applied Surface Science, 2021. **550**: p. 149316 https://doi.org/10.1016/j.apsusc.2021.149316
109. Mann, D.S., S.-N. Kwon, P. Patil, and S.-I. Na, *Revivification of nickel oxide-perovskite interfaces via nickel nitrate to boost performance in perovskite solar cells.* Nano Energy, 2023. **106**: p. 108062 https://doi.org/10.1016/j.nanoen.2022.108062
110. Yang, J., T. Wang, Y. Li, X. Pu, H. Chen, Y. Li, B. Yang, Y. Zhang, J. Zhao, Q. Cao, X. Chen, S. Ghasemi, A. Hagfeldt, and X. Li, *Overcome Low Intrinsic Conductivity of NiOx Through Triazinyl Modification for Highly Efficient and Stable Inverted Perovskite Solar Cells.* Solar RRL, 2022. **6**(9): p. 2200422 https://doi.org/10.1002/solr.202200422
111. Lian, Q., P.-l. Wang, G. Wang, X. Zhang, Y. Huang, D. Li, G. Mi, R. Shi, A. Amini, L. Zhang, and C. Cheng, *Doping Free and Amorphous NiOx Film via UV Irradiation for Efficient Inverted Perovskite Solar Cells.* Advanced Science, 2022. **9**(18): p. 2201543 https://doi.org/10.1002/advs.202201543
112. Zhang, J., J. Yang, R. Dai, W. Sheng, Y. Su, Y. Zhong, X. Li, L. Tan, and Y. Chen, *Elimination of Interfacial Lattice Mismatch and Detrimental Reaction by Self-Assembled Layer Dual-Passivation for Efficient and Stable Inverted Perovskite Solar Cells.* Advanced Energy Materials, 2022. **12**(18): p. 2103674 https://doi.org/10.1002/aenm.202103674
113. Hu, Y., Z. Yang, X. Cui, P. Zeng, F. Li, X. Liu, G. Feng, and M. Liu, *Construction of Charge Transport Channels at the NiOx/Perovskite Interface through Moderate Dipoles toward Highly Efficient Inverted Solar Cells.* ACS Applied Materials & Interfaces, 2022. **14**(11): p. 13431-13439 10.1021/acsami.2c01625
114. Yang, X., H. Yang, M. Su, J. Zhao, X. Meng, X. Hu, T. Xue, Z. Huang, Y. Lu, Y. Li, and Z. Yang, *Scalable Flexible Perovskite Solar Cells Based on a Crystalline and Printable Template with Intelligent Temperature Sensitivity.* Solar RRL, 2022. **6**(4): p. 2100991 https://doi.org/10.1002/solr.202100991

115. Boyd, C.C., R.C. Shallcross, T. Moot, R. Kerner, L. Bertoluzzi, A. Onno, S. Kavadiya, C. Chosy, E.J. Wolf, J. Werner, J.A. Raiford, C. de Paula, A.F. Palmstrom, Z.J. Yu, J.J. Berry, S.F. Bent, Z.C. Holman, J.M. Luther, E.L. Ratcliff, N.R. Armstrong, and M.D. McGehee, *Overcoming Redox Reactions at Perovskite-Nickel Oxide Interfaces to Boost Voltages in Perovskite Solar Cells.* Joule, 2020. **4**(8): p. 1759-1775 https://doi.org/10.1016/j.joule.2020.06.004
116. Greener, J., G. Pearson, and M. Cakmak, *Roll-to-Roll Manufacturing: Process Elements and Recent Advances*. 2018: Wiley.
117. Dharmadasa, R., M. Jha, D.A. Amos, and T. Druffel, *Room Temperature Synthesis of a Copper Ink for the Intense Pulsed Light Sintering of Conductive Copper Films.* ACS Applied Materials & Interfaces, 2013. **5**(24): p. 13227-13234 10.1021/am404226e
118. Su, J., H. Cai, X. Ye, X. Zhou, J. Yang, D. Wang, J. Ni, J. Li, and J. Zhang, *Efficient Perovskite Solar Cells Prepared by Hot Air Blowing to Ultrasonic Spraying in Ambient Air.* ACS Applied Materials & Interfaces, 2019. **11**(11): p. 10689-10696 10.1021/acsami.9b01843
119. Sánchez, S., M. Vallés-Pelarda, J.-A. Alberola-Borràs, R. Vidal, J.J. Jerónimo-Rendón, M. Saliba, P.P. Boix, and I. Mora-Seró, *Flash infrared annealing as a cost-effective and low environmental impact processing method for planar perovskite solar cells.* Materials Today, 2019. **31**: p. 39-46 https://doi.org/10.1016/j.mattod.2019.04.021
120. Ouyang, Z., M. Yang, J.B. Whitaker, D. Li, and M.F.A.M. van Hest, *Toward Scalable Perovskite Solar Modules Using Blade Coating and Rapid Thermal Processing.* ACS Applied Energy Materials, 2020. **3**(4): p. 3714-3720 10.1021/acsaem.0c00180
121. Chen, Q., T. Ma, F. Wang, Y. Liu, S. Liu, J. Wang, Z. Cheng, Q. Chang, R. Yang, and W.J.A.S. Huang, *Rapid Microwave-Annealing Process of Hybrid Perovskites to Eliminate Miscellaneous Phase for High Performance Photovoltaics.* 2020. **7**(12): p. 2000480
122. Sandha Gupta, K.S., *Structural and Thermo-Mechanical Study of Aluminum Coated Polyethylene Terphthalate (PET) Film.* International Journal of Innovative Research in Electronics and Communications, 2016. **3**(2): p. 7-14
123. Pandey, M., Z. Wang, G. Kapil, A.K. Baranwal, D. Hirotani, K. Hamada, and S. Hayase, *Dependence of ITO-Coated Flexible Substrates in the Performance and Bending Durability of Perovskite Solar Cells.* Advanced Engineering Materials, 2019. **21**(8): p. 1900288 10.1002/adem.201900288
124. Ragay, P.G., R.W. Parks, L.A.R. Garcia, and R.G. Kruzek. (2009) Rapid thermal firing IR conveyor furnace having high intensity heating section, U.S.P. Office, 7,805,064
125. Sowade, E., H. Kang, K.Y. Mitra, O.J. Weiß, J. Weber, and R.R. Baumann, *Roll-to-roll infrared (IR) drying and sintering of an inkjet-printed silver nanoparticle ink within 1 second.* Journal of Materials Chemistry C, 2015. **3**(45): p. 11815-11826 10.1039/C5TC02291F
126. Perelaer, J., B.J. de Gans, and U.S. Schubert, *Ink-jet Printing and Microwave Sintering of Conductive Silver Tracks.* Advanced Materials, 2006. **18**(16): p. 2101-2104 10.1002/adma.200502422
127. Fouassier, J.P., *Photoinitialization Photopolymerization and Photocuring*. 1995, Cincinnati, OH: Hanser/Gardner Publications, Inc.

128. Druffel, T., R. Dharmadasa, B.W. Lavery, and K. Ankireddy, *Intense pulsed light processing for photovoltaic manufacturing.* Solar Energy Materials and Solar Cells, 2018. **174**: p. 359-369 10.1016/j.solmat.2017.09.010
129. Xu, W., T.B. Daunis, R.T. Piper, and J.W.P. Hsu, *Effects of Photonic Curing Processing Conditions on MAPbI3 Film Properties and Solar Cell Performance.* ACS Applied Energy Materials, 2020 10.1021/acsaem.0c01243
130. Troughton, J., M.J. Carnie, M.L. Davies, C. Charbonneau, E.H. Jewell, D.A. Worsley, and T.M. Watson, *Photonic flash-annealing of lead halide perovskite solar cells in 1 ms.* Journal of Materials Chemistry A, 2016. **4**(9): p. 3471-3476 10.1039/C5TA09431C
131. Feleki, B., G. Bex, R. Andriessen, Y. Galagan, and F. Di Giacomo, *Rapid and low temperature processing of mesoporous TiO2 for perovskite solar cells on flexible and rigid substrates.* Materials Today Communications, 2017. **13**: p. 232-240 https://doi.org/10.1016/j.mtcomm.2017.09.007
132. Das, S., B. Yang, G. Gu, P.C. Joshi, I.N. Ivanov, C.M. Rouleau, T. Aytug, D.B. Geohegan, and K. Xiao, *High-Performance Flexible Perovskite Solar Cells by Using a Combination of Ultrasonic Spray-Coating and Low Thermal Budget Photonic Curing.* ACS Photonics, 2015. **2**(6): p. 680-686 10.1021/acsphotonics.5b00119
133. Zhu, M., W. Liu, W. Ke, S. Clark, E.B. Secor, T.-B. Song, M.G. Kanatzidis, X. Li, and M.C. Hersam, *Millisecond-pulsed photonically-annealed tin oxide electron transport layers for efficient perovskite solar cells.* Journal of Materials Chemistry A, 2017. **5**(46): p. 24110-24115
134. Ghahremani, A.H., S. Pishgar, J. Bahadur, and T. Druffel, *Intense Pulse Light Annealing of Perovskite Photovoltaics Using Gradient Flashes.* ACS Applied Energy Materials, 2020. **3**(12): p. 11641-11654 10.1021/acsaem.0c01520
135. Muydinov, R., S. Seeger, S.H.B. Vinoth Kumar, C. Klimm, R. Kraehnert, M.R. Wagner, and B. Szyszka, *Crystallisation behaviour of CH3NH3PbI3 films: The benefits of sub-second flash lamp annealing.* Thin Solid Films, 2018. **653**: p. 204-214 https://doi.org/10.1016/j.tsf.2018.03.050
136. Xu, W., Z. Liu, R.T. Piper, and J.W.P. Hsu, *Bayesian Optimization of photonic curing process for flexible perovskite photovoltaic devices.* Solar Energy Materials and Solar Cells, 2023. **249**: p. 112055 https://doi.org/10.1016/j.solmat.2022.112055
137. Woodhouse, M., B. Smith, A. Ramdas, and R. Margolis, *Crystalline Silicon Photovoltaic Module Manufacturing Costs and Sustainable Pricing: 1H 2018 Benchmark and Cost Reduction Roadmap*. 2019, National Renewable Energy Laboratory: Golden, CO.
138. Fuller, M. and M. Warwick, *The catalytic oxidation of carbon monoxide on tin (IV) oxide.* Journal of Catalysis, 1973. **29**(3): p. 441-450
139. McManus, J.S., P.D. Cunningham, L.B. Regan, A. Smith, D.W. McGrath, and P.W. Dunne, *Highly soluble ligand stabilized tin oxide nanocrystals: gel formation and thin film production.* Crystal Growth & Design, 2014. **14**(9): p. 4819-4826
140. Deacon, G. and R. Phillips, *Relationships between the carbon-oxygen stretching frequencies of carboxylato complexes and the type of carboxylate coordination.* Coordination Chemistry Reviews, 1980. **33**(3): p. 227-250

141. Beach, E.R., K. Shqau, S.E. Brown, S.J. Rozeveld, and P.A. Morris, *Solvothermal synthesis of crystalline nickel oxide nanoparticles.* Materials Chemistry and Physics, 2009. **115**(1): p. 371-377 https://doi.org/10.1016/j.matchemphys.2008.12.018
142. Carta, F., A. Akdemir, A. Scozzafava, E. Masini, and C.T. Supuran, *Xanthates and Trithiocarbonates Strongly Inhibit Carbonic Anhydrases and Show Antiglaucoma Effects in Vivo.* Journal of Medicinal Chemistry, 2013. **56**(11): p. 4691-4700 10.1021/jm400414j
143. Sawant, P., E. Kovalev, J.T. Klug, and S. Efrima, *Alkyl xanthates: New capping agents for metal colloids. Capping of platinum nanoparticles.* Langmuir, 2001. **17**(10): p. 2913-2917 10.1021/la0014961
144. Ichiro, H., K. Taketoshi, F. Takatomo, M. Taketoshi, and U. Katsuyuki, *Carboxylation of Phenol Derivatives. XXII. Formation of Alkali Alkyl Carbonate by the O-Carboxylation of Alcohol in the Presence of an Alkali Salt of a Weak Acid.* Bulletin of the Chemical Society of Japan, 1976. **49**(10): p. 2775-2779 10.1246/bcsj.49.2775
145. Bai, Y., S. Xiao, C. Hu, T. Zhang, X. Meng, Q. Li, Y. Yang, K.S. Wong, H. Chen, and S. Yang, *A pure and stable intermediate phase is key to growing aligned and vertically monolithic perovskite crystals for efficient PIN planar perovskite solar cells with high processibility and stability.* Nano Energy, 2017. **34**: p. 58-68 https://doi.org/10.1016/j.nanoen.2017.02.019
146. Cao, Q., Y. Li, H. Zhang, J. Yang, J. Han, T. Xu, S. Wang, Z. Wang, B. Gao, J. Zhao, X. Li, X. Ma, S.M. Zakeeruddin, W.E.I. Sha, X. Li, and M. Gratzel, *Efficient and stable inverted perovskite solar cells with very high fill factors via incorporation of star-shaped polymer.* Sci Adv, 2021. **7**(28) 10.1126/sciadv.abg0633
147. Moghadamzadeh, S., I.M. Hossain, M. Jakoby, B.A. Nejand, D. Rueda-Delgado, J.A. Schwenzer, S. Gharibzadeh, T. Abzieher, M.R. Khan, and A.A. Haghighirad, *Spontaneous enhancement of the stable power conversion efficiency in perovskite solar cells.* Journal of Materials Chemistry A, 2020. **8**(2): p. 670-682
148. Fei, C. and H. Wang, *Age-induced recrystallization in perovskite solar cells.* Organic Electronics, 2019. **68**: p. 143-150
149. Chang, N.L., A.W.Y. Ho-Baillie, D. Vak, M. Gao, M.A. Green, and R.J. Egan, *Manufacturing cost and market potential analysis of demonstrated roll-to-roll perovskite photovoltaic cell processes.* Solar Energy Materials and Solar Cells, 2018. **174**: p. 314-324 10.1016/j.solmat.2017.08.038
150. Mathews, I., S. Sofia, E. Ma, J. Jean, H.S. Laine, S.C. Siah, T. Buonassisi, and I.M. Peters, *Economically Sustainable Growth of Perovskite Photovoltaics Manufacturing.* Joule, 2020. **4**(4): p. 822-839 10.1016/j.joule.2020.01.006
151. USGS, *Indium. Mineral Commodity Summaries.* . 2020, United States Geological Survey: Washington DC.
152. Song, Z., C.L. McElvany, A.B. Phillips, I. Celik, P.W. Krantz, S.C. Watthage, G.K. Liyanage, D. Apul, and M.J. Heben, *A technoeconomic analysis of perovskite solar module manufacturing with low-cost materials and techniques.* Energy & Environmental Science, 2017. **10**(6): p. 1297-1305 10.1039/c7ee00757d
153. Woodhouse, M., A. Goodrich, R. Margolis, T.L. James, M. Lokanc, and R. Eggert, *Supply-Chain Dynamics of Tellurium, Indium, and Gallium Within the Context of PV*

Manufacturing Costs. IEEE Journal of Photovoltaics, 2013. **3**(2): p. 833-837 10.1109/jphotov.2013.2242960

154. Martin, B., M. Yang, R.C. Bramante, E. Amerling, G. Gupta, M.F.A.M. van Hest, and T. Druffel, *Fabrication of flexible perovskite solar cells via rapid thermal annealing.* Materials Letters, 2020. **276** 10.1016/j.matlet.2020.128215
155. Kumar, A., M. Bieri, T. Reindl, and A.G. Aberle, *Economic Viability Analysis of Silicon Solar Cell Manufacturing: Al-BSF versus PERC.* Energy Procedia, 2017. **130**: p. 43-49 10.1016/j.egypro.2017.09.412
156. Yun, J.S., W.J. Choi, S.H. Kim, E. Cho, S.J. Lee, J.H. Lee, J.H. Park, and D.S. Ham, *Inhibition of iodide ion migration in flexible perovskite solar cells using oxide–metal–oxide transparent electrode.* Surfaces and Interfaces, 2021. **27**: p. 101546 https://doi.org/10.1016/j.surfin.2021.101546
157. Shahbazi, S., C.-M. Tsai, S. Narra, C.-Y. Wang, H.-S. Shiu, S. Afshar, N. Taghavinia, and E.W.-G. Diau, *Ag Doping of Organometal Lead Halide Perovskites: Morphology Modification and p-Type Character.* The Journal of Physical Chemistry C, 2017. **121**(7): p. 3673-3679 10.1021/acs.jpcc.6b09722
158. Kato, Y., L.K. Ono, M.V. Lee, S. Wang, S.R. Raga, and Y. Qi, *Silver Iodide Formation in Methyl Ammonium Lead Iodide Perovskite Solar Cells with Silver Top Electrodes.* Advanced Materials Interfaces, 2015. **2**(13): p. 1500195 https://doi.org/10.1002/admi.201500195
159. A. Shaker, S., H. Khaledi, and H. Mohd Ali, *2-Methylbenzimidazolium thiocyanate-2-methylbenzimidazole (1/1).* Acta Crystallographica Section E, 2010. **66**(9): p. o2291 doi:10.1107/S1600536810031181
160. Fischer, A., H. Pettersson, A. Hagfeldt, G. Boschloo, L. Kloo, and M. Gorlov, *Crystal formation involving 1-methylbenzimidazole in iodide/triiodide electrolytes for dye-sensitized solar cells.* Solar Energy Materials and Solar Cells, 2007. **91**(12): p. 1062-1065 10.1016/j.solmat.2007.02.020
161. Kooijman, H., A.H. Velders, and A.L. Spek, *N-Methylbenzimidazole N-methylbenzimidazolium hexafluorophosphate.* Acta Crystallographica Section E, 2006. **62**(1): p. o21-o23 doi:10.1107/S1600536805039383
162. Jian, F., F. Bei, X. Wang, and L. Lu, *Synthesis and crystal structure of 2-chloromethyl-1H-benzimidazole nitrate,[ClCH2 (C7H6N2)] NO3.* CHINESE JOURNAL OF STRUCTURAL CHEMISTRY, 2003. **22**(4): p. 382-386
163. Wang, X., Q. Zhao, Z. Li, D. Liu, C. Chen, B. Zhang, X. Sun, X. Du, L. Hao, C. Gao, Y. Li, S. Mao, Z. Shao, X. Wang, G. Cui, and S. Pang, *Improved performance and stability of perovskite solar cells by iodine-immobilizing with small and flexible bis(amide) molecule.* Chemical Engineering Journal, 2023. **451**: p. 138559 https://doi.org/10.1016/j.cej.2022.138559
164. Halvani Anaraki, E., A. Kermanpur, M.T. Mayer, L. Steier, T. Ahmed, S.-H. Turren-Cruz, J. Seo, J. Luo, S.M. Zakeeruddin, and W.R. Tress, *Low-temperature Nb-doped SnO2 electron-selective contact yields over 20% efficiency in planar perovskite solar cells.* ACS Energy Letters, 2018. **3**(4): p. 773-778

165. Song, J., W. Zhang, D. Wang, K. Deng, J. Wu, and Z. Lan, *Colloidal synthesis of Y-doped SnO_2 nanocrystals for efficient and slight hysteresis planar perovskite solar cells.* Solar Energy, 2019. **185**: p. 508-515
166. Xiong, L., M. Qin, G. Yang, Y. Guo, H. Lei, Q. Liu, W. Ke, H. Tao, P. Qin, and S. Li, *Performance enhancement of high temperature SnO_2-based planar perovskite solar cells: electrical characterization and understanding of the mechanism.* Journal of Materials Chemistry A, 2016. **4**(21): p. 8374-8383

List of Abbreviations

Abbreviation	text
ACN	Acetonitrile
BCP	Bathocuproine
C60	carbon 60
CAPEX	Capital equipment expenses
CB	Chlorobenzene
CDT	Corona Discharge Treater
CH_2I_2	Diiodomethan
CIGS	Copper Indium Gallium Disellinide
COGS	Cost of goods sold
CTL	Conductive transport layer
DFT	density functional theory
DI	de-ionized
DMF,	Dimethylformamide
DMSO	Dimethyl sulfoxide
EIS	electro impedence spectroscopy
EOP	End of project
ETL	electron transport layer
FA	formadinium
FF	Fill factor
FTO	Flourinate tin oxide
GBL	Gamma-Butyrolactone
GNG	Go/no-go
GW	gigawatt
HTL	hole transport layer
i	intrinsic
I	Current
IPL	Intense pulsed light
IR	infrared
ISOS	International Summit on Organic PV Stability
ITO	indium tin oxide
IV	current voltage
J_{SC},	short circuit current
MA	Methyl ammonium
MAPI	methyl ammonium lead iodide
MC	multi cation
n	n-type material

NiO	Nickel oxide
NMP	N-Methylpyrrolidone
NP	nanoparticle
NREL	National Renewable Energy Laboratory
NSF	National Science Foundation
NVCS	Non-volatile coordinating solavent
OPEX	operational expenses
p	p-type material
PCBM	[6,6] phenyl-C61-butyric acid methyl ester
PCE	photo conversion efficiency
PEAI	Phenethylammonium iodide
PEDOT	poly polystyrene sulfonate
PEN	poly ethylene napthalate
PET	poly ethylene terapthalate
PFN	
PL	photo luminescence
PSC	perovskite solar cell
PTAA	poly(triaryl amine)
PV	photovoltaic
PVSK	perovskite (as pertaining to a film or ink)
SEM	scanning electron microscope
SnO2	Tim oxide
TC	triple cation
TCO	transparent conductive oxide
TW	terrawatt
UV	Ultraviolet
VNCS	volatile non-coordinating solvent
V_{oc},	Opern circuit voltage
W,	Watt
XPS,	X-ray photoelectron spectroscopy
XRD	X-ray diffraction spectroscopy
Y	Yttrium